DISS. ETH NO. 19825

Backscatter and Humidity Measurements in Cirrus and Dust Clouds using Balloon Sondes

A dissertation submitted to

ETH ZURICH

for the degree of

Doctor of Sciences

presented by

MARTIN BRABEC

Dipl. Geogr., University of Zurich

born 16 March 1978

citizen of Switzerland

accepted on the recommendation of

Prof. Dr. T. Peter, examiner
Dr. F. G. Wienhold, co-examiner
Dr. H. Vömel, co-examiner

2011

Contents

Abstract

Cirrus clouds cover approximately 30 % of the Earth's atmosphere and influence climate in various aspects, such as radiation, stratospheric ozone and atmospheric water budget. Currently, the knowledge regarding mechanisms of cirrus cloud formation and their properties are far from comprehensive. Previous studies of in-cloud and clear sky water vapour measurements in the upper troposphere reveal high supersaturations with respect to ice occasionally exceeding even water saturation. This led Peter et al. (2006) to state that "recent field observations call into question the basic principles underpinning the current understanding of ice cloud formation and alter the assessment of water distribution in the upper troposphere". Furthermore, Spichtinger et al. (2005a) noticed that one of the shortcomings of radiosonde data is the lack of knowledge whether the measurements occurred in clear sky conditions or inside a cirrus cloud. Therefore, the balloon-borne backscatter sonde COBALD (Compact Optical Backscatter and AerosoL Detector) was developed recently to provide this additional information. It is shown that COBALD is able to detect cirrus clouds, to and distinctly define their boundaries, and to accurately measure the particle backscatter ratio at two wavelengths (455 nm and 870 nm), from which the ice water content and to some approximation also the ice particle number density and a lower bound of the ice particle radius can be derived. These measurements enhance the RHi measurements and consequently also the cirrus cloud studies. COBALD was successfully launched 111 times during numerous capaigns, together with various high quality hygrometers sondes such as CFH, SnowWhite and FPH measuring humidity in the upper troposphere with the low water mixing ratios demanding for the best available instruments.

A case study focussing on a sounding in Lindenberg, Germany (52.21°N, 14.12°E) in November 2008, which was part of the "Lindenberg Upper-Air Methods Intercomparison" (LUAMI) campaign, shows that the COBALD-CFH tandem is an excellent payload to determine the partitioning of atmospheric water between the gas phase and the condensed ice phase in and around cirrus clouds, and thus to detect in-cloud and out-of-cloud supersaturations with respect to ice. The case discussed in detail is characterised by very little horizontal wind shear, making it ideal for detailed testing of cirrus modelling. We show that operational analysis data of ECMWF (1°x1° spatial resolution, 6-hourly stored fields) fail to represent important cloud properties, such as ice water contents or relative humidities, whereas COSMO-7 fields (6.6 x 6.6 km, hourly) provide a much better agreement with the humidity measurements, though the profile of the ice water content is not captured accurately. The main differences between the ECMWF and the COSMO data are the resolution of small-scale vertical winds, which allows the mesoscale model to better represent cirrus nucleation and growth processes, and better mesoscale representation of mixing processes resulting in a more accurate representation of relative humidity. Comprehensive microphysical cloud model calculations along LAGRANTO trajectories based on COSMO-7 wind and temperature fields allow to determine the humidity, ice particle size, number density and backscatter ratios, which are in good agreement with

the measured cirrus clouds. Experimental runs with higher time-resolved output fields (every 5 minutes) from COSMO-7 are presently underway. These are expected to lead to improved vertical trajectory movements and cooling rates, and hence to further improve the modeled cloud properties.

Moreover, this thesis investigates balloon-borne measurements of S_{ice} comprising all sky, in-cloud and clear sky conditions analysing data from 43 cirrus clouds detected on 27 balloon soundings in northern high latitudes, mid-latitude, the tropics, monsoon region and in the southern hemisphere in the temperature range 190 - 250 K. Frequent super- and subsaturations are observed inside cirrus clouds. Yet no measurements reveal supersaturations above water saturation, which contrasts with previous studies but agrees with common thermodynamic knowledge. In-cloud measurements show a saturation with the median at $S_{ice} = 1.02$, i.e. a median-symmetric distribution around equilibrated saturation. The absolute minimum and maximum values of $S_{ice} = 0.3$ and 1.49. The extremely low value for S_{ice} of 0.3 can be explained as fall-streaks, i.e. particles falling into dry regions below the cloud. The study shows that cirrus clouds reveal significant differences concerning S_{ice} among the geographical regions. The observed increase of the median from high-latitudes to low latitudes could result from different formation processes encountered in the corresponding geographical regions, e.g. in situ cloud formation versus outflow. This asks for further investigation, also raising the question if future cirrus studies need to be analysed by differentiating geographical regions. Clear sky observations follow an exponential frequency distribution regarding S_{ice} which means that the probability of measuring a certain amount of ice supersaturation in the analysed troposphere decreases exponentially with the degree of ice supersaturation. This characteristic has been described by other cirrus studies (Gierens et al., 1999; Spichtinger et al., 2002; Ovarlez et al., 2002).

Finally, COBALD was launched in Lauder, New Zealand to measure dust events transported from Australia across the Tasman Sea. With the support of the Lagrangian trajectory calculation tool LAGRANTO based on ECMWF wind fields, it is shown that the dust measured in Lauder originated from the Australian south east coast due to a dust storm also observed by the MODIS satellite. The dust arriving in Lauder was characterised in terms of particle size and number density based on Mie calculus. This revealed three possible estimated dust particle sizes, which are 0.5 μm, 1.3 μm and 2.9 μm. The corresponding number densities are 1 cm^{-3}, 0.2 cm^{-3} and 0.06 cm^{-3}, respectively. The estimated particle sizes (1.3 μm and 2.9 μm) agree with previous studies analysing dust travelling from Asia to a measuring site at San Nicolas Island, California revealing sizes of 1-2 μm (Tratt et al., 2001) and Asian dust that reached other parts of western North America during the April 1998 event indicating, finding particle sizes of 2-3 μm (Husar et al., 2001). This supports validity of the assumptions made by Mie calculations based on COBALD's measurements.

In summary, the studies presented in this thesis prove COBALD to be an essential and extremely reliable tool for application in further atmospheric studies focusing on cirrus clouds and dust measurements.

Zusammenfassung

Zirruswolken bedecken ungefähr 30% der Erdatmosphäre und beeinflussen das Klima in diversen Bereichen, so beispielsweise bezüglich der Strahlung, des Stratosphärenozons und des atmosphärischen Wassergehalts. Die heutigen Kenntnisse über die Bestandteile der Zirren und die Mechanismen ihrer Formation sind relativ beschränkt. Bisherige Studien, bei denen "in-cloud" und wolkenfreie Wasserdampfmessungen in der oberen Troposphäre vorgenommen wurden, ergaben eine hohe Eisübersättigung, die gegebenenfalls sogar die Wasserübersättigung übersteigt. Dies veranlasste Peter et al. (2006) zur folgenden Annahme: "[...] recent field observations call into question the basic principles underpinning the current understanding of ice cloud formation and alter the assessment of water distribution in the upper troposphere". Im Rahmen ihrer Studie erkannten Spichtinger et al. (2005a) zudem das Problem, dass es bei Radiosondendaten nicht möglich ist, zwischen "in-cloud"- und wolkenlosen Bedingungen zu unterscheiden. Um zu dieser zusätzlichen Information zu gelangen, wurde die Rückstreuballonsonde COBALD (Compact Optical Backscatter and AerosoL Detector) entwickelt. Es steht fest, dass COBALD Zirruswolken sowohl erkennen als auch deren Grenzen klar definieren und den Partikelrückstreuungsanteil bei zwei verschiedenen Wellenlängen (455 nm und 870 nm) genau messen kann. Anhand dieser Messung kann der Wassergehalt und annähernd auch die Teilchendichte der Eispartikel, wie auch eine untere Grenze des Eispartikelradius' abgeschätzt werden. Diese Untersuchungen bereichern die Feuchte-Messungen und in Folge dessen auch die Studien von Zirruswolken. COBALD wurde in verschiedenen Kampagnen 111 Mal erfolgreich gestartet, zusammen mit diversen hochqualitativen Hygrometersonden wie CFH, SnowWhite und FPH. Dabei wurde die Feuchtigkeit in der oberen Troposphäre gemessen. Die da vorherrschenden niedrigen Wassermischungsverhältnisse verlangen nach den besten verfügbaren Instrumenten.

Eine Fallstudie mit Fokus auf eine Sondierung - ausgeführt in Lindenberg, Deutschland, 52.21°N, 14.12°E, innerhalb der "Lindenberg Upper-Air Methods Intercomparison" (LUAMI)-Kampagne zeigt, dass das COBALD-CFH-Tandem eine exzellente Sondenkombination ist, um die Menge von atmosphärischem Wasser in gasförmigem Zustand und kondensierter Eisphase in und um Zirruswolken zu bestimmen. Dies ermöglicht die Eisübersättigung innerhalb und ausserhalb der Wolke festzustellen. Die geringe horizontale Windscherung hilft die Zirrusmodellierung zu testen. Es zeigt sich, dass die Daten der operationalen Analyse von ECMWF (1°x1° räumliche Auflösung, 6-stündlich gespeicherte Felder) unzureichend sind, um wichtige Wolkeneigenschaften wie Eiswassergehalt oder relative Feuchtigkeit zu bestimmen. COSMO-7-Felder (6.6 x 6.6 km, stündlich) hingegen ergeben eine bessere Übereinstimmung mit Feuchtigkeitsmessungen, auch wenn das Profil des Eiswassergehalts nicht genau erfasst wurde. Ein Unterschied zwischen den ECMWF- und COSMO ist die Auflösung von kleinformatigen vertikalen Winden. Dies ermöglicht eine bessere Repräsentation der Prozesse der Zirrusnukleation und des -wachstums mit dem mesoskaligen Modell wie auch jene von vermischten Prozessen, die eine angemessenere Repräsentation von relativer Feuchtigkeit zur Folge haben. Um-

fassende, den LAGRANTO-Trajektorien entsprechende, mikrophysikalische Berechnungen von Wolkenmodellen basierend auf COSMO-7-Wind- und Temperaturfeldern erlauben es, die Feuchtigkeit, die Grösse der Eispartikel, die Teilchendichte und den Rückstreuungsanteil abzuschätzen. Sie sind in guter Übereinstimmung mit den gemessenen Zirruswolken. Berechnungen mit höheren zeitaufgelösten Output-Feldern (alle fünf Minuten) sind noch nicht abgeschlossen. Es wird erwartet, dass diese die vertikalen Trajektorienbewegungen und die Kühlraten verbessern, und damit die bestehenden Modelle über Wolkeneigenschaften bereichern können.

In dieser Arbeit wurden zudem Messungen von Eisübersättigung in Ballonsondierungen, sowohl "in-cloud"- als auch unter wolkenlosen Bedingungen durchgeführt. Daten von 43 Zirruswolken aus 27 Ballonsondierungen in unterschiedlichen geographischen Regionen (nördliche hohe und mittlere Breitengrade, Tropen, Monsunregion und südliche Hemisphäre) und Temperaturen zwischen 190-250 K wurden analysiert. Es konnten häufige Über- und Untersättigung im Innern der Zirruswolken beobachtet werden. Allerdings zeigen die bisherigen Messungen keine Übersättigung oberhalb der Wassersättigung, was im Gegensatz zu früheren Studien in Übereinstimmung mit dem gängigen Wissen über Thermodynamik steht. "In-cloud"-Messungen zeigen eine Sättigung mit einem Median von S_{ice} = 1.02, d.h. eine mediansymmetrische Verteilung um eine ausgewogene Sättigung. Die Werte des absoluten Minimums und Maximums betragen S_{ice} = 0.3 und 1.49. Der extrem niedrige Wert von S_{ice} = 0.3 kann durch Sedimentation erklärt werden, d.h. die Partikel fallen in nicht gesättigte Bereiche unter der Wolke. Die Studie zeigt, dass Zirruswolken in den unterschiedlichen geographischen Regionen signifikante Unterschiede bezüglich des Sice aufweisen. Der beobachtete Anstieg des Medians von höheren zu niedrigen Breitengraden könnte darin begründet sein, dass in den entsprechenden geographischen Regionen unterschiedliche Formationsprozesse begegnen, z.B. in-situ-Wolkenformation vs. Ausströmung. Dies erfordert weitere Untersuchungen und wirft die Frage auf, ob in zukünftigen Studien zu Zirren unterschiedliche geographische Regionen differenziert werden müssen. Beobachtungen bei wolkenlosen Bedingungen ergeben eine exponentielle Häufigkeitsverteilung bezüglich S_{ice}, d.h. dass die Wahrscheinlichkeit der Eisübersättigung mit dem Grad der Eisübersättigung exponentiell abnimmt. Diese Eigenschaft wurde bereits in anderen Studien zu Zirren beschrieben (Gierens et al., 1999; Spichtinger et al., 2002; Ovarlez et al., 2002).

Schliesslich wurde COBALD in Lauder, Neuseeland, gestartet, um die Staubvorkommen zu messen, die von Australien über das Tasmanische Meer transportiert wurden. Das Trajektorienmodell LAGRANTO, das auf ECMWF-Windfeldern basiert, zeigt, dass der Staub in Lauder von der australischen Südküste stammt und wegen eines Staubsturms auch vom Terra-MODIS beobachtet wurde. Die Partikelgrösse und Teilchendichte des Staubs in Lauder wurden durch Mie-Berechnungen abgeschätzt. Dies ergab die drei folgenden möglichen Schätzungen für die Partikelgrössen: 0.5 μm, 1.3 μm und 2.9 μm, mit entsprechenden Massen für die Teilchendichte von 1 cm^{-3}, 0.2 cm^{-3} und 0.06 cm^{-3}. Die geschätzten Partikelgrössen 1.3 μm und 2.9 μm stimmen mit Resultaten aus früheren Studien überein. Staubpartikel aus Asien, die in San Nicolas Island, Kalifornien gemessen wurden, zeigen eine Grösse von 1-2 μm (Tratt et al., 2001) und asiatischer Staub, der andere Teile im westlichen Nordamerika in Folge eines Sturms im April 1998 erreichte, weist eine Partikelgrösse von 2-3 μm auf (Husar et al., 2001). Diese Resultate auf der Basis der COBALD-Messungen unterstützen die Annahmen der Mie-Berechnungen.

Zusammenfassend kann gesagt werden, dass die Studien dieser Arbeit aufzeigen, dass

COBALD ein wichtiges Messinstrument für zukünftige atmosphärische Studien von Zirruswolken und Staub darstellt.

Chapter 1

Introduction

The focus of this thesis is the investigation of cirrus cloud properties based on balloon sounding data. The soundings which were carried out are unique due to the use of a newly developed backscatter sonde, the Compact Optical Backscatter AerosoL Detector (COBALD). Supported by optical scattering models, the backscatter sondes provide aerosol and cloud particle information of the sampled ambient air parcel. Particle sizes and densities can be estimated from the measured backscatter signal. In most of the measurements discussed here, we flew COBALD in tandem with a high quality hygrometer. Measuring low water mixing ratios in the upper troposphere requires the best available instruments.

This thesis consists of two introductory chapters. After a general introduction into the problem in Chapter 1, Chapter 2 introduces the scientific basics. Chapter 3 provides a description of the design and operational principles of the instruments used. The following two chapters (Chapter 4 and 5) analyse cirrus cloud observations. Chapter 6 discusses dust aerosols transported from Australia to New Zealand. One purpose of that chapter is to point out a further application of the newly developed backscatter sonde. The last two chapters summarise the results and give an outlook.

1.1 Climate change

The main contribution to the natural greenhouse effect is due to atmospheric water vapour but the detailed processes are still uncertain (IPCC, 2007).

Moreover, the Intergovernmental Panel on Climate Change (IPCC), finds that the Earth's climate change is largely due to anthropogenic influences since the beginning of the industrial era ($\sim$1860). The increase of the temperature is clearly correlated with anthropogenic activities such as fuel consumption, energy production and refrigeration. Therefore the reduction of greenhouse gases was the primary goal of the United Nations Framework Convention on Climate Change (UNFCCC) protocol launched in Kyoto (Japan) on December 11, 1997.

Many of the key processes that control climate sensitivity or abrupt climate changes, such as the formation of cirrus clouds depend on very small spatial scales (IPCC, 2007). Due to the small spatial scales it is so far impossible to represent them in full detail within global models. Moreover the detailed scientific understanding of these processes is still a major uncertainty in the current understanding of the climate system. Therefore the IPCC report of 2007 states that "there is a continuing need to assist in the use and interpretation of complex models through models that are either conceptually simpler, or limited to a number of processes or to a specific region and therefore enabling a deeper understanding of the processes at work or a more relevant comparison with observations".

1.2 Cirrus clouds

Clouds contain either liquid droplets, ice crystals or a mixture of both, suspended in the atmosphere. Cirrus clouds are composed of ice crystals that form in the upper troposphere and temperatures typically below -38°C (Pruppacher and Klett, 1997). They cover approximately 30 % of the Earth's atmosphere and play an important role in the climate system (Wylie and Menzel, 1999).

1.2.1 Influence of cirrus clouds on the climate

Cirrus clouds play an important role in atmospheric radiative transfer, stratospheric ozone and atmospheric water budget. Fu et al. (1998) show further that climate model predictions critically depend on the cirrus radiative properties assumed. Cirrus clouds therefore play a significant role in regulating the radiation balance of the atmospheric system. Radiative analyses of mid latitude cirrus clouds indicate that the transition between warming (i.e. for dominating absorption of thermal radiation emitted by Earth towards space) and cooling (i.e., dominating albedo effect) strongly depends on macrophysical properties such as temperature and the optical thickness of the cloud, which in turn depend on the microphysical properties like crystal size, crystal shape, ice water content and number density (Wendisch et al. (2007) and Fusina et al. (2007)). For optically thin cirrus for instance, the absorption of infrared radiation and lack of re-emission at low temperatures dominates the scattering of incoming solar radiation, which leads to a net warming. For optically thicker clouds, the scattering of incoming solar radiation may dominate, leading to a net cooling (Wendisch et al., 2007). Generally it is believed that cirrus clouds on average lead to a global warming (Chen et al., 2000). However, Zhang et al. (2005) showed that different climate models react differently to radiative influences, which implies that it is difficult to estimate the overall effect of cirrus clouds on the radiative budget.

Cirrus clouds may also influence stratospheric ozone and the stratospheric circulation by their ability to change heating rates (Dessler et al., 1996). Moreover, cirrus clouds host heterogeneous chemical reactions in particular in middle and high latitudes, thereby contributing to the observed decline of ozone in the mid latitude of the lower stratosphere (Borrmann et al., 1996).

Another aspect of cirrus clouds is their role in dehydration. In the tropics, high-altitude cirrus clouds are thought to form through freeze-drying the air and therefore dehydrate air by precipitating ice before the air enters the tropical lower stratosphere, hence influencing the stratospheric water vapour budget (Jensen et al. (1996) and Braham and Spyers-Duran (1967)).

The role and properties of cirrus clouds mentioned above remains poorly quantified, demonstrating the importance of studying cirrus clouds.

1.2.2 Supersaturation inside and outside of cirrus clouds

Figure 1.1 shows different water vapour measurements (personal communications by Thomas Peter) embedded in a coordinate frame of ice saturation versus temperature in order to compare with lab-based theory of homogeneous freezing illustrated in panel (a) (Koop et al., 2000). The cyan line represents the liquid water saturation threshold described by Murphy and Koop (2005). The black slanted lines represent the maximum saturation ratio with respect to ice that can be reached before homogeneous ice nucleation is expected to start for 50 nm solution droplets for the upper line and 5 μm for the lower, respectively. Panel (b) shows results from AIDA chamber experiments during a simulation of cloud forming conditions in the upper troposphere. The RHi evolution in the presence of ammonium sulfate ($(NH_4)_2SO_4$, Abbatt et al. (2006)) and organic carbon on soot particles (Möhler et al., 2005). The results show that the ammonium sulfate experiment agrees with our microphysical understanding, whereas soot does not serve as an ice nucleus. Panel (c), (d) and (e) represent aircraft measurements. Panel (c) shows observation at 17 km above Costa Rica in 2004. RHi measurements reach 230 % (Jensen et al., 2005), which contradicts our most fundamental understanding of instantaneous droplet growth (and immediate subsequent freezing due to homogeneous nucleation). Panel (d) assembles in-cloud data from either cirrus (black) or contrails (green) collected at 10-15 km over Florida in July 2002 (Gao et al., 2004). It shows supersaturations of 30% for at least 1 hour. Krämer et al. (2007) present data from inside cirrus clouds in the tropics (reddish), mid-latitudes (greenish) and Arctic (bluish) in panel (e). "All sky" balloon observations by Vömel et al. (2007a) from Costa Rica and Indonesia are shown in panel (f). Here it is not possible to distinguish between in cloud and clear sky observations, because no in-situ cloud information has been available (such as COBALD data) on these soundings.

High supersaturations were thought to be removed quickly by condensation of the vapour on cloud particles. For typical conditions (particle size, number density) Peter et al. (2006) estimated the relaxation time due to gas phase diffusion limited ice growth to be of the order of minutes. This relaxation is shown in Figure 1.2 panel (a). Particles nucleate (yellow star in panel (a)) at a certain threshold ($S_{ice} \approx 1.6$) and S_{ice} in panel (d) decreases (green curve). Murray (2008) note that organic coatings may suppress freezing , an effect that has been made responsible for the observations shown in Figure 1.2 (b,c) and that is also illustrated in Figure 1.2 (b). Panel (d) shows therefore a perpetuation of the supersaturation (purple curve). Slow water vapour transfer to the ice phase is another hypothesis modelled by Gao et al. (2004), which leads to long supersaturation relaxation times (Krämer et al., 2009). This phenomenon is shown in panel (c). Ice forms, but as displayed in panel (d) the supersaturation decreases very slowly as compared to the above estimate.

Another explanation for low temperature ($T < 190$ K) is formation of cubic ice particles (Murray et al., 2005) that compared to the stable hexagonal configuration, has an approximately 10 % higher equilibrium vapour pressure (Shilling et al., 2006). Krämer et al. (2009) suggest that the supersaturation "puzzle" could be explained by unexpectedly low ice crystal number densities causing the observed supersaturation. A further possible explanation is the formation of glassy aerosols (Zobrist et al., 2008), which may drastically reduce the water uptake. Nonetheless, all these mechanisms act only under specific conditions and cannot explain the observed high supersaturation temperatures (Peter et al., 2006). As Barahona and Nenes (2011) state: "Lacking the predictive understanding of

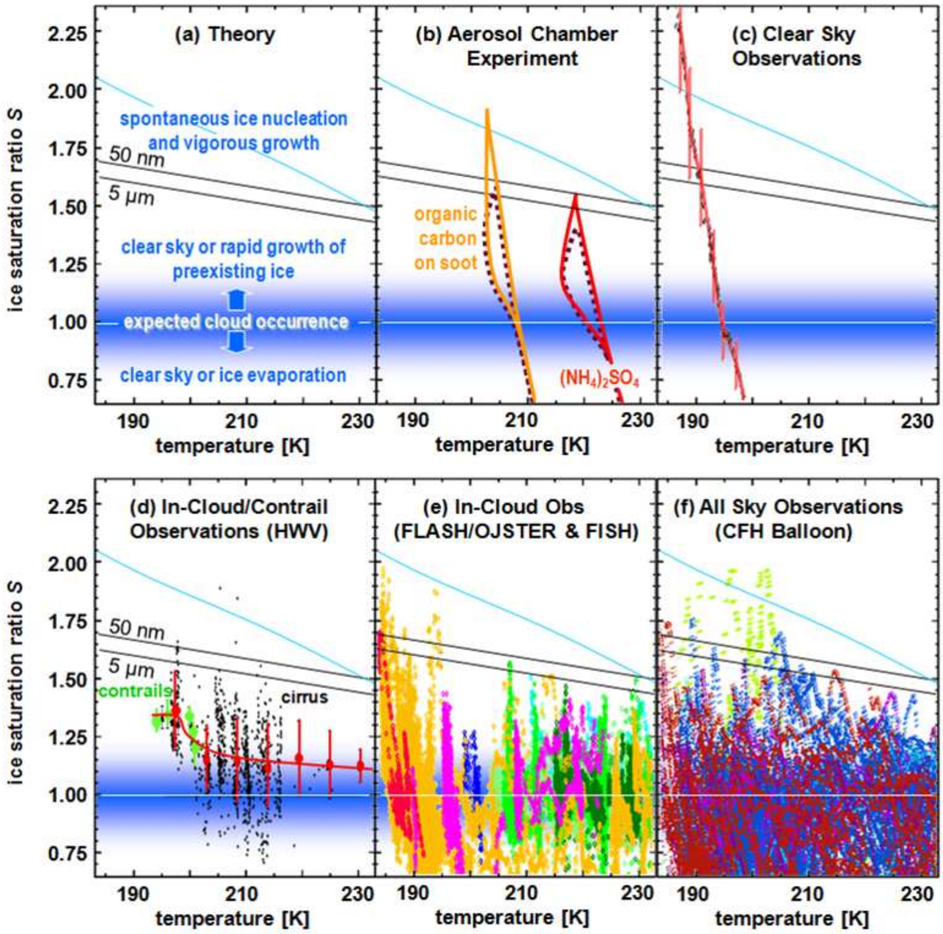

Figure 1.1: *S_{ice} as function of temperature. Cyan line stands for the liquid water saturation threshold described by Murphy and Koop (2005). Upper black slanted lines stand for 50 nm solution droplets nucleation threshold and 5 µm for the lower (Koop et al., 2000). (a) Best present knowledge: lab-based theory of homogeneous freezing. Supersaturated ($S_{ice} < 1$) conditions are characterised by either clear sky or ice particles evaporation. Around the $S_{ice} = 1$ cloud occurrence is expected whereas above this threshold clear sky or rapid growth of preexisting ice occurs. (b) AIDA experiments, Möhler et al. (2005), Abbatt et al. (2006). (c) WB-57 aircraft measurements, Costa Rica, Jensen et al. (2005). (d) WB-57 measurement inside cirrus clouds or contrails, Gao et al. (2004). (e) Learjet and Geophysica aircraft measurements, Krämer et al. (2009). (f) All sky balloon-borne measurements, Costa Rica and Indonesia, Vömel et al. (2007a). The highest observed supersaturations are difficult to reconcile with the present understanding (Pruppacher and Klett (1997) and Koop et al. (2000)).*

such phenomena hinders the ability of climate models to capture the climate effects of cirrus clouds and their response to anthropogenic perturbations."

1.2.3 Upper Tropospheric Water Vapour Measurements and their Difficulties

To analyse water saturation in cirrus clouds it is essential to have high quality water vapour measurements.

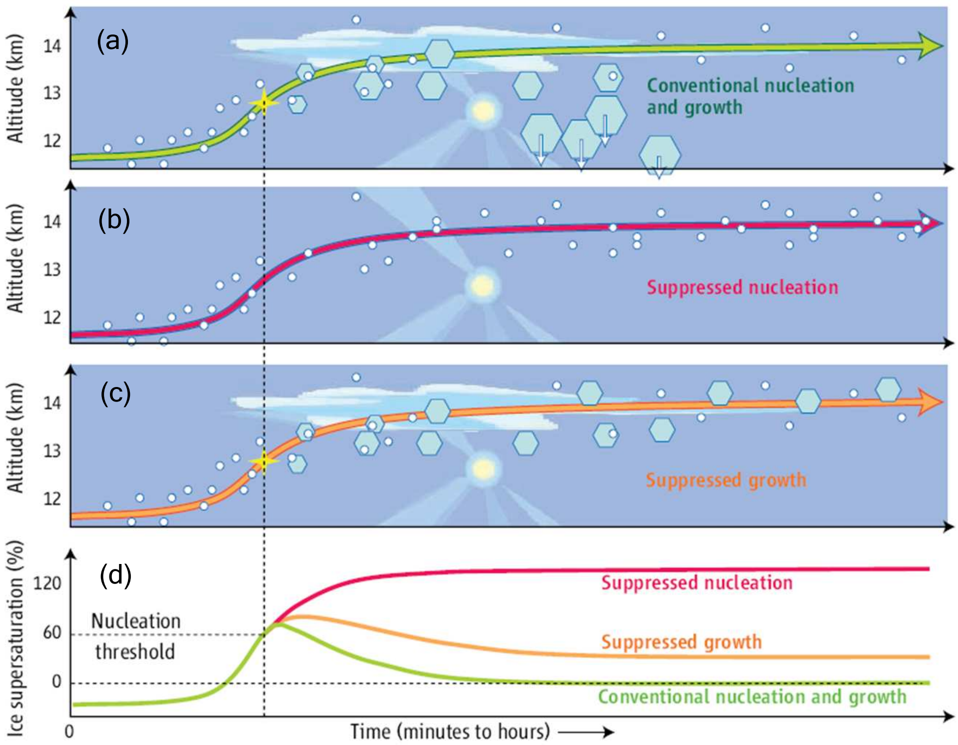

Figure 1.2: *Humidity increase through rising air parcels and eventual ice cloud formation. The top three panels show three air parcel trajectories while the bottom panel shows the effect of these scenarios in terms of supersaturation. According to conventional understanding of cirrus cloud formation, ice particles nucleate by reaching the freezing threshold (stars), grow, and return to equilibrium (green curves). Observations as mentioned in the text suggest suppressed nucleation (red curves) or suppressed growth (orange curves) in the atmosphere. (Peter et al., 2006)*

Remote sensing and in-situ measurements are the two techniques available to measure water vapour in the atmosphere. Remote sensing techniques can be employed by using either ground-based, space-borne systems or carried on in-situ platforms, while in-situ instruments are carried by aircraft or balloon-borne platforms. Remote sensing systems may allow for continuous observations and can have the advantage of global cover (i.e. Meteosat by EUMETSAT). But measurement uncertainties can be large and the spatial resolution is often coarse (Albertz, 2001). In-situ measurement techniques provide overall a better spatial resolution than remote sensing systems. But still, also for these measurements "conditions within clouds might fluctuate faster than aircraft-borne instruments can resolve" (Peter et al., 2006). Since balloon-borne instruments ascend with a much lower speed of typically 5 m/s their vertical resolution is better. However, balloon measurements are point measurements and therefore do not represent a large horizontal area. Using trajectory calculations, additional insight can be achieved to extend the analysed area.

Measuring water vapour in the upper troposphere is difficult because of the low H_2O partial pressures and because the H_2O molecule sticks to most surfaces, which may lead to artefacts. Therefore campaigns are organised such as AquaVIT, an intercomparison of atmospheric water measurement inside the AIDA (Aerosols, Interactions and Dynamics in the Atmosphere) chamber in Karlsruhe, 8-26 October 2007, or LUAMI (Lindenberg campaign regarding an Upper-Air Methods Intercomparison) in Lindenberg, 10 November - 1 December 2008 in order to compare various in-situ instruments. The aim of such campaigns is to verify the instrumental data quality and if applicable improve the instruments. Campaigns like AquaVIT reveal that the measurement of water vapour in the upper troposphere is still a challenging issue. Möhler et al. (2009) state that depending on the water content, instruments showed inconsistencies in a range of $1 \leq H_2O \leq 10$ ppm of about 20 % to +1000% with most instruments reading significantly higher than the reference value.

A brief overview of the instruments used is given in Chapter 3.

1.3 Aerosols

The case study described in Chapter 6 focuses on dust aerosols which were measured by a COBALD sounding in Lauder, New Zealand. The dust aerosols are originated from an Australian dust storm. Therefore a brief introduction into aerosols follows.

Aerosols are defined as a dispersion of solid and/or liquid particles suspended in gas. Aerosols are produced by various processes occurring on land and water surfaces and in the atmosphere itself. There are notable differences in the size, chemical nature and sources of aerosols (Jacob, 1999).

In the early 1990s researchers started to focus increasingly on aerosols as climate forcing agents. Thereafter, the range of climate relevant aerosols was extended beyond sulfates to include nitrates, organics, soot, mineral dust and sea salt altough aerosols are one of the least understood components of the climate system (IPCC, 2007). Figure 1.3 compares the radiative forcing for greenhouse gases and other climate forcing factors, along with an assessment of the level of scientific understanding (LOSU). Aerosols contribute the largest negative radiative forcing (cooling), but at the same time the level of scientific understanding of their climate influence is ”low” to ”medium-low”.

1.3.1 Influence of Aerosols on the Climate

Aerosols exert climate forcing in two ways, the direct and the indirect aerosol effect. The direct aerosol effect is due to the scattering and the absorption of sunlight by aerosols, both of which are determined by the physical state, the size, the absorption cross section and the chemical composition of the particles. Aerosols also cause an indirect effect by acting as cloud condensation nuclei (CCN) for liquid clouds or as ice nuclei (IN) for ice clouds and therefore modify cloud optical properties and persistence. In the complete absence of aerosols, cloud droplets could not form without supersaturations of several hundred percent. Consequently aerosols largely affect the initial cloud droplet number concentration, cloud lifetime and albedo (Giannakaki et al., 2009).

As described by IPCC (2007), uncertainties about the aerosol effects for mineral dust are particularly high.

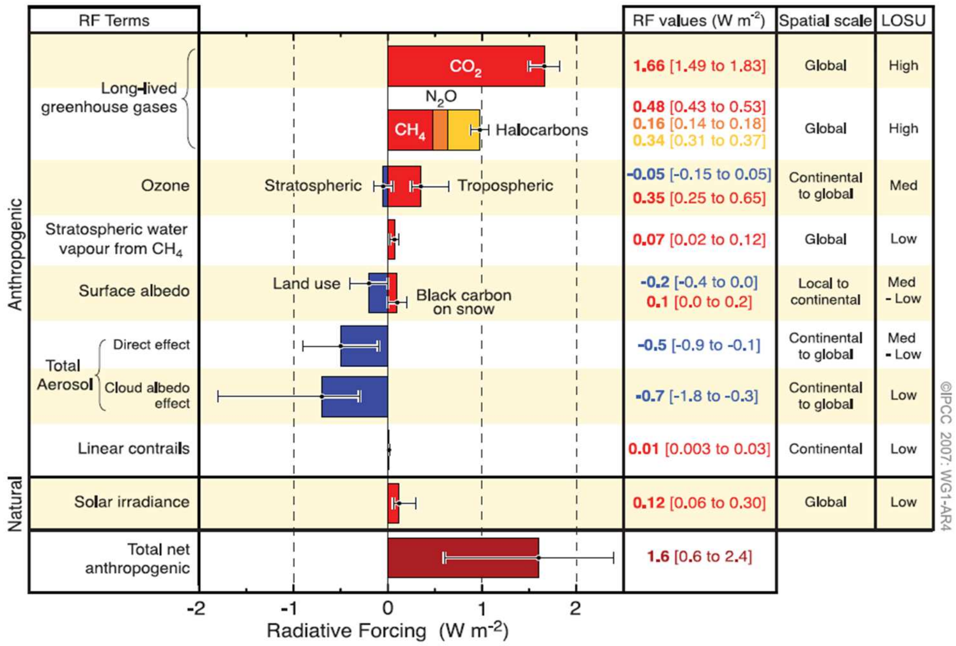

Figure 1.3: *Global average radiative forcing (RF) in 2005 for anthropogenic and natural components and mechanisms with its typical geographical extent (spatial scale) and the assessed level of scientific understanding (LOSU). Additional forcing factors not included here are considered to have a very low LOSU or have an episodic nature (volcanic aerosols) and are therefore hard to capture. (IPCC, 2007)*

1.3.2 The Role of Australian Dust Aerosols and the Connection to this Thesis

Australia is the dominant dust source in the Southern Hemisphere (Tanaka and Chiba, 2006), with a range of environmental impacts including iron fertilization of surrounding oceans and possible climate feedbacks (Cassar et al., 2007). Unfortunately, "a systematic characterisation of the composition and optical properties of Australian dust aerosol is currently lacking", as Qin and Mitchell (2008) state. Also Rotstayn et al. (2009) mention a need for a better understanding of the Australian dust source.

The atmosphere over Australia is influenced by a number of aerosol sources, including soil-dust, sea-salt, biomass burning and secondary organic aerosols (SOA) as products of gas-to-particle conversion. The major extended anthropogenic sources are the capital cities in each state, although there are several significant, isolated point sources, such as power stations (Rotstayn et al., 2009).

Chapter 6 in this thesis hopes to contribute to a better understanding of dust aerosols in the southern hemisphere focussing on Australia and New Zealand.

1.4 Objectives of the thesis

Measuring and interpreting the properties of cirrus clouds in the upper troposphere and tropopause region are necessary prerequisites for developing the ability to understand and predict the radiative effects of cirrus clouds, their role in precipitation processes and in the hydrological cycle, and subsequently their impact on climate.

This chapter outlined the major difficulties encountered when measuring water vapour in the upper troposphere, regarding data quality and ambiguity of clear sky or in-cloud classification. Furthermore, this chapter described recent in situ observations that reveal unexpectedly high supersaturation with respect to ice. It is still poorly understood how such supersaturations can be maintained. However, instrumental artifacts can not be excluded.

This thesis addresses in particular the following five objectives.

- Collect accurate and reliable water vapour data by using balloon-borne sondes. These measurements are supplemented by a newly developed backscatter sonde called Compact Optical Backscatter AerosoL Detector (COBALD) with which it is possible to distinguish between clear sky and in-cloud measurements.
- COBALD needs to be characterised and calibrated. This thesis presents a robust calibration procedure and characterises COBALD in Chapter 3.
- Mie and T-Matrix calculations are performed to estimate particle size and number concentration (Chapter 4, 5 and 6).
- Chapters 5 and 6 present trajectory calculations to assist the data interpretation. Chapter 4 additionally involves a microphysical model, which is used as box model in a column model mode. The model is run along COSMO-2 regional model output, and the results are compared with the COBALD and hygrometer measurements in addition to the ECMWF and COSMO microphysical output.
- COBALD can be used for a variety of atmospheric applications such as volcanic ash and polar stratospheric cloud studies. This thesis presents a dust study in Chapter 6 and contributes to overcome the described lack of systematic characterisation of Australian dust aerosols.

Chapter 2

Scientific background

As mentioned in the introduction, this thesis analyses balloon-borne measurement data aiming to investigate cirrus clouds and aerosols. With each payload we gain information on ambient temperature, pressure, S_{ice} through hygrometer measurements, and backscatter information by the newly developed backscatter sonde COBALD (for instrumental details see Chapter 3).

Cirrus clouds are characterised in more detail in the first part of this chapter. Important processes concerning cirrus cloud formation are homogeneous and heterogeneous nucleation. Currently their relative importance for the ice nucleation is not clear, yet homogeneous and heterogeneous nucleation lead to different types and number densities of ice crystals substantially affecting cloud optical properties and their lifetime (Cantrell and Heymsfield, 2005). In view of the case study in Chapter 6, dust aerosol properties are described subsequently. Finally, light scattering is depicted in order to provide the basis to interpret the COBALD backscatter data.

2.1 Cirrus clouds

2.1.1 Cirrus cloud classification

The World Meteorological Organization (WMO) is responsible for the official classification of clouds and distinguishes between Cirrus (Ci), Cirrocumulus (Cc), and Cirrostratus (Cs). Ci appear as detached clouds in the form of white filaments. Cc are white or mostly white patches, while Cs exist as narrow white bands (WMO, 1956). Subvisible cirrus' have also been described in several articles, Jensen et al. (1996) and Kärcher (2002).

The WMO classification does not explicitly require physical properties such as particle size distribution, particle number density or optical depth, although they are considered to be sensible criteria for the characterisation of cirrus clouds.

Alternatively, cirrus clouds are classified by their optical depth in order to address their radiative properties. Table 2.1 lists the subdivision of cirrus clouds according to Sassen (2002). Five mechanisms responsible for cirrus cloud formation are described according to Sassen (2002): (1) synoptic, (2) injection, (3) mountain-wave updraft, (4) cold trap and (5) contrail cirrus clouds.

(1) Synoptic cirrus clouds are formed by lifting of air masses. This occurs in connection with jet streams and frontal and low-pressure systems and are common over land and oceans at midlatitudes. They tend to form through homogeneous nucleation of haze

Category	τ range	Description
Subvisual	0.03	Invisible against the blue sky
Thin	0.03-0.3	Translucent, retains a bluish colour
Opaque	0.3-3.0	Usually appears white or greyish

Table 2.1: *Cirrus clouds subdivided by their optical depths after Sassen (2002).*

particles in regions where ice supersaturation is high (DeMott, 2002).

(2) Mostly in the tropics deep convection transports massive amounts of water vapour and ice particles into the upper troposphere and thereby forms optical thick anvils. These clouds are called 'anvil cirrus' (Jensen et al., 2009). Their optical depth often exceeds a value of 3.0, whereas in the classical meteorology they are considered as a part of the whole Cumulonimbus. Ice particle number concentration in fresh anvil cirrus often ranges between 1 cm^{-3} and 10 cm^{-3}. In aged anvil cirrus ice number densities reduce to typically $\simeq$ 0.1 cm^{-3} but rarely exceed 1 cm^{-3} (Jensen et al., 2009).

(3) Orographically formed cirrus clouds (mountain-wave updraft) can persist for long distances downwind of the wave generating terrain (Wylie, 2002).

(4) Cold trap cirrus clouds occur primarily at very high altitude in the tropics and are optically thin or subvisible. Thunderstorm activities are recognised as their humidity supply.

(5) Finally, contrail cirrus, develop by trails of condensed water vapour made by the exhaust of aircraft engines. With their unique formation mechanism and geographical distribution they are a rather new phenomenon (Schumann, 2002).

2.1.2 Homogeneous Ice Nucleation

Nucleation processes involve the transition of a parent phase (i.e. liquid water or a solution) to a new phase (i.e. ice). The new phase begins with a cluster of several molecules and can grow to a macroscopic accumulation under the right conditions. If the new phase is thermodynamically more stable than the parent phase ascertained by the environment, the transition to the new phase is energetically favourable (Pruppacher and Klett, 1997). The formation of a new phase involves the formation of a new surface between the phases, which requires energy. This energy barrier ΔG has to be overcome in each nucleation process (Pruppacher and Klett, 1997). The rate J at which ice particles are nucleated depends on the height of the energy barrier, since

$$J \propto exp\left(-\frac{\Delta G}{kT}\right), \tag{2.1}$$

where T is the temperature and k the Boltzmann constant (Pruppacher and Klett, 1997). The height of the energy barrier depends firstly on the new phase related quantities such as the surface tension between the new and the parent phase and secondly on the condition in the parent phase, such as temperature and water activity (Koop et al., 2000). The higher the supersaturation the lower the energy barrier and thereafter the occurrence of formation of a critical cluster is more likely.

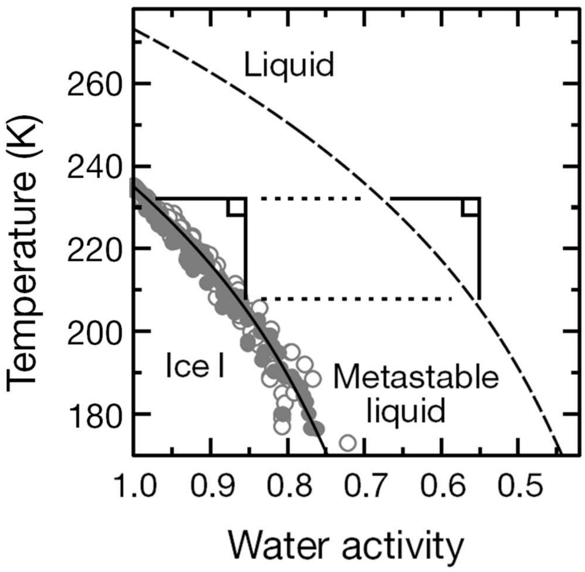

Figure 2.1: *Freezing temperatures (T_f) of approximately 1-10 μm droplets of 18 different aqueous solutions as a function of the water activity (a_w. For species shown as dots a_w was calculated at T_f using an ion interaction model. For all circles a_w was estimated by determining a_w at the melting temperature (dashed line), and assuming that for a fixed composition a_w is independent of temperature between T_f and T_m. The solid line is the melting point curve. (Koop et al., 2000)*

The classical nucleation theory suggests that the nucleation process is driven by the water activity, but also by the solute effects on the liquid to solid interface energy and the activation energy for a water molecule to freeze from a solution phase (Pruppacher and Klett, 1997). In contradiction, Koop et al. (2000) showed that homogeneous freezing is only a function of a temperature dependent water activity in solutions and not of the solute.

The water activity of a solution is the ratio of its water vapour pressure to the vapour pressure over pure water at the same conditions. Thus, by expressing freezing temperature as a function of water activity Koop et al. (2000) obtained Figure 2.1 in which circles and dots represent solutions with different solutes and concentration. Despite that variability, all data group around a single curve (solid) representing the freezing temperature threshold. The solid curve where all solutions freeze is the freezing temperature threshold. For example, at temperatures lower than 233 K (-40°C) this process requires airmasses in a state of substantial supersaturation which is generally larger than 40% (Spichtinger et al., 2003)).

2.1.3 Heterogeneous Ice Nucleation

While homogeneous freezing of supercooled aqueous phase aerosol particles is reasonably well understood, understanding heterogeneous ice nucleation raises uncertainties (IPCC, 2007).

Heterogeneous ice nucleation on insoluble particles may take place at a much lower supersaturation than homogeneous nucleation. This is the consequence of the nucleation rate J increasing due to the presence of an ice nucleus (IN) which reduces the energy barrier ΔG (Pruppacher and Klett, 1997). Hence, heterogeneous nucleation may play an

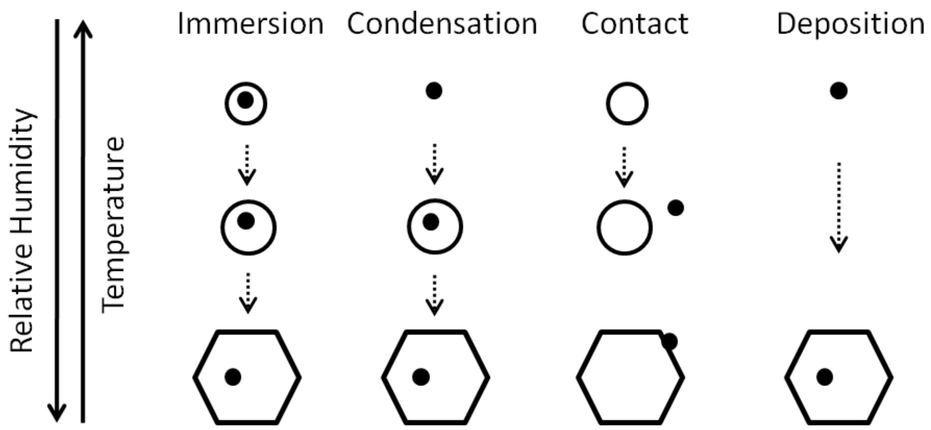

Figure 2.2: *Heterogeneous Nucleation pathways. This figure shows four schemes of heterogeneous nucleation. Heterogeneous nucleation is commonly grouped into immersion, condensation, contact and deposition mode. The dots represent IN's, the circles supercooled aqueous solution droplets and the hexagons nucleated ice particles.*

important role in our atmosphere if the impacts of heterogeneous nucleation differ from the homogeneous case.

Heterogeneous nucleation is commonly classified in four different types. These are immersion, condensation, contact and deposition as schematically illustrated in Figure 2.2. The dots represent IN's, the circles represent supercooled aqueous solution droplets and the hexagons illustrate nucleated ice particles.

Immersion freezing occurs when a droplet with an immersed IN is cooled to a supercooled threshold value at which the IN initiates freezing of the droplet. The condensation freezing pathway refers to where a cloud droplet nucleates on the IN and immediately freezes. When a dry aerosol particle collides with a supercooled cloud droplet and the droplet freezes it is called contact nucleation. The last heterogeneous ice nucleation pathway is called deposition nucleation and refers to ice nucleation by deposition of water molecules directly from the vapour phase which means the vapour phase has to be supersaturated with respect to ice.

Heterogeneous nucleation lowers the required activation energy for the nucleation process (DeMott, 2002) and therefore occurs at lower S_{ice}. With limited IN available, this process leads to a smaller concentration of larger particles compared to homogeneous nucleation (Borrmann et al. (1996) and Kärcher and Lohmann (2003)).

The different crystal sizes interact differently with radiation. Heterogeneous clouds provide a lower net radiative forcing than those which form homogeneously.

Cantrell and Heymsfield (2005) indicate in their review article that mineral dust and soot may be the most important IN in the UT. Supporting this theory are aircraft measurements indicating that the major IN in a cirrus cloud at around 12 km may be of these types (Cziczo et al., 2004).

2.1.4 Cirrus cloud formation and microphysical aspects

If an air parcel is lifted quickly its temperature decreases adiabatically and S_{ice} will increase. Based on Figure 2.3 three different trajectories and their evolution are explained which are termed "wet", "average" and "dry". These terms reflect their absolute water content (Wiacek and Peter, 2009). The Roman numerals stand for cloud types and the Arabic numerals for formation processes applicable in the corresponding trajectory area. The formation processes and therefore the cloud types are strongly temperature dependent.

The "wet" trajectory on the far right in Figure 2.3 reaches the water saturation threshold after being lifted adiabatically. A liquid cloud (i) is formed (1). This refers to temperature >273 K saturation wrt liquid water. If the air parcel is further cooled to a temperature below 273 K the liquid cloud might be transformed into a mixed-phase (ii) cloud due to droplets that nucleate heterogeneously on suitable IN (immersion freezing) or collide with IN (contact freezing). The most common "average" trajectory passes through (v) where ice can form through heterogeneous (3) nucleation (likely deposition freezing on dry nuclei) and form a warm thin cirrus with low crystal number densities. If ice is formed RH_{ice} will relax to 100. If there are not any suitable IN in this region the air parcel will become supersaturated with respect to ice, by further cooling. Eventually it reaches the water saturation threshold where homogeneously nucleated ice crystals and heterogeneously nucleated water droplets can exist simultaneously (4) and form a mixed-phase cloud (ii). Upon further lifting the air parcel follows the water saturation curve and at a temperature of approximately 233 K (Wiacek and Peter, 2009) homogeneous nucleation occurs where all remaining water droplets nucleate to ice (5). Finally, the "dry" trajectory passes region (iv), where heterogeneous nucleation (likely deposition freezing on dry nuclei) can occur in case sufficiently potent IN are available and form a cold thin cirrus (6). If the cloud has not been formed due to a lack of potent IN the trajectory reaches the homogeneous ice nucleation limit and forms a cold dense cirrus (7) homogeneously (iii).

In mixed-phase clouds (ii), ice particles grow at the expense of neighbouring water droplets driven by the lower partial pressure above ice (Bergeron-Findeisen process, Seinfeld and Pandis (1998)) or due to depletion of water vapour (diffusional growth, Pruppacher and Klett (1997)). Ice crystal growth behaviour is primarily determined by temperature and relative humidity inside the cloud (Cantrell and Heymsfield, 2005).

If particles have not nucleated heterogeneously in regions (iv) and (v) the water vapour is in a metastable phase. Areas like that are termed ice-supersaturated regions (ISSR) (Spichtinger et al., 2005a). The following processes, that are described more detailed in Spichtinger (2004) are potential candidates for the formation processes of ISSRs:

- Temperature drop: The adiabatic ascent due to warm/cold fronts or the crossing over mountains can form ISSRs through the accompanied temperature drop.
- If nucleation takes place and hydrometeors are formed and fall out, ISSR's may remain.
- Convective ascent of air can cause ISSRs.
- Turbulent mixing: Through (small) convective events the change of specific humidity is the driving force for high RHi.

In addition, the cooling rates significantly affects size and number density of the ice

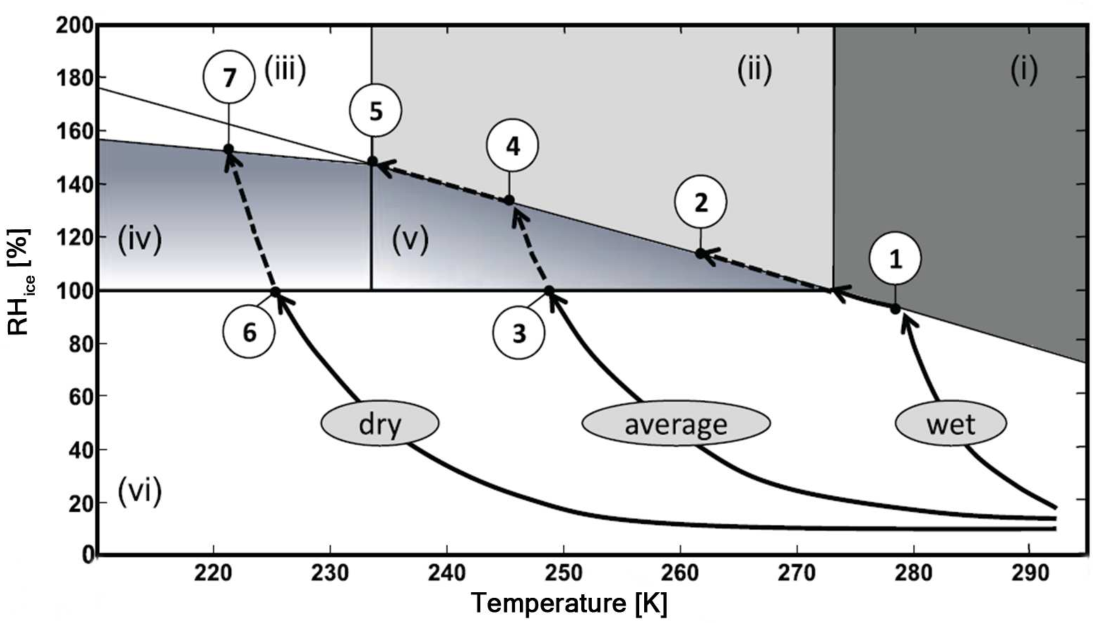

Figure 2.3: *Cloud types shown in Roman numerals from 1-7 and cloud formation processes (i-vi) illustrated by means of three trajectories. Adapted from (Wiacek and Peter, 2009).*

crystals produced by homogeneous nucleation. Liquid droplet concentrations measured in strong updrafts (fast cooling) typically exceed 100 cm^{-3} and may produce mainly small ice particles (Heymsfield et al., 2005).

As soon as ice particles exist they start depleting the gas phase water vapour to aspire equilibrium S$_{ice}$. This is due to molecular diffusion driven by the water vapour partial pressure gradient (Pruppacher and Klett, 1997). Korolev and Mazin (2003) show that the product of the mean number and size of the ice crystals n$_{ice}$ x r$_{ice}$ is one important parameter controlling the water vapour relaxation time τ. Analysis of the diffusion equation for cirrus altitude conditions lead to relation:

$$\tau_{RHi} \approx \frac{1000s}{n_{ice} \times r_{ice}}. \tag{2.2}$$

Equation 2.2 reveals that the time scale for diffusion growth is inversely proportional to the product of ice crystal number density n$_{ice}$ in cm^{-3} and size r$_{ice}$ in μm.

The growth of the ice crystals lead to an eventual sedimentation. This speed of sedimentation is size dependent and named terminal velocity.

The terminal velocity v is described by the following equation and describes the balance of gravitational and viscous forces (Finlayson-Pitts and Pitts, 2000a):

$$v = \frac{2(\rho_p - \rho_{air})gr^2}{\eta}, \tag{2.3}$$

where ρ_p and ρ_{air} is the particle density and ambient air density, respectively, g is the acceleration due to gravity, r is the radius and η is the viscosity of air.

Equation 2.3 can be approximated, by assuming the viscosity to be hight independent, (for temperature and pressure regimes equals to lower stratosphere and upper troposphere) to:

$$v \cong 1\frac{m}{h}\left(\frac{r}{\mu m}\right)^2, \tag{2.4}$$

whereas m is meter, h is hour and r the radius of the crystal in μm. For example, this yields a terminal velocity of 4 m/h for a particle of 2 μm radius. In this thesis only the approximation equation 2.4 is used since it is valid for lower stratosphere and upper troposphere.

2.2 Aerosols

2.2.1 Dust Aerosols

In September 2009 a huge dust storm event occurred in the center of Australia. The dust was carried over the Tasman Sea towards New Zealand where it was measured by COBALD and the NOAA Frost Point Hygrometer (NOA-FPH, described in chapter 3). The analysis of this event is presented within a case study in chapter 6. This section provides the related information on dust aerosols.

Aerosols are commonly defined as fine solid or liquid particles suspended in a gas (Seinfeld and Pandis, 1998). Aerosols appear in the atmosphere either by direct emission (primary aerosols) or are formed in situ by gas to particle conversion (secondary aerosols). The size distribution and composition of aerosol particles can differ strongly because they are altered by coagulation, chemical reaction, condensation, evaporation, or by activation as cloud condensation nuclei (CCN) or ice nuclei (IN). Further, the concentration varies greatly with time and location. (Pruppacher and Klett, 1997)

The aerosol size distribution contains typically four modes, known as the coarse-particle (2.5-100 μm in diameter), accumulation (0.1-2.5 μm), Aitken (0.01-0.1 μm) and nucleation modes (less than 10 nm) (Finlayson-Pitts and Pitts, 2000b). The accumulation mode has the greatest impact on climate because size and composition of these particles (typically sulfates and organic carbon compounds) determine longer lifetimes in the atmosphere compared (Hobbs, 1993).

Aerosols play an important role in the climate system by affecting the radiation budget (Tegen and Lacis, 1996) and atmospheric chemistry (Ziemann, 2010). Additionally, aerosols adversely affect air quality and human health (Griffin et al., 2001). Dust particles from different regions have also been found to have strikingly different optical properties (Giannakaki et al., 2009). Hence, evaluating the contribution of each dust source region reduces uncertainties in a study of dust cycles.

The residence time of accumulation mode particles is typically 3-10 days and they have a significant effect on visibility, cloud formation and atmospheric chemistry. In the

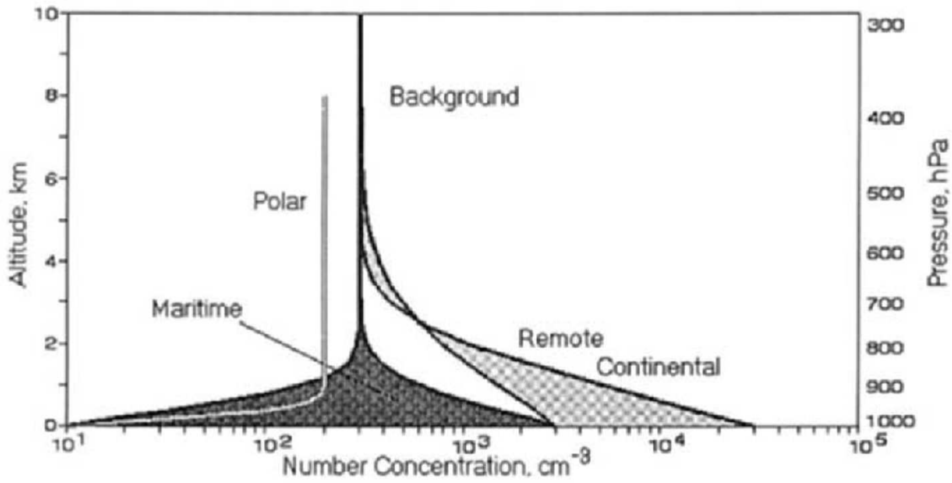

Figure 2.4: *Vertical distribution of background aerosol number concentrations (Jaenicke, 1993).*

presence of large concentrations of dust, the coarse particle mode can also be optically active and hence be climatically important (Giannakaki et al., 2009).

2.2.2 Background Aerosols

Microphysical modelling (chapter 6) strongly suggests that the payload deployed in Lauder, New Zealand on 25 September 2009 measured swollen background aerosols at an altitude of 8 km. These aerosol particles grow in size due to increasing saturation and thereby maintain equilibrium with the ambient water vapour that condenses onto the particle. This swelling process is called hygroscopic growth (Jaenicke, 1993).

Charlson et al. (1974) define background aerosols as particles which exists in remote locations, away from local sources but may include the contribution from distant human activities. The tropospheric background aerosol is characterised by direct emissions and gas-to-particle formation from natural sources. Referring to mass, direct emissions from deserts, the oceans, and vegetations contribute the largest fraction in the troposphere. According to Hobbs (1993) the concentration of tropospheric particles varies with altitude (Figure 2.4). It has to be taken into account that the number concentration has a large variability in terms of space and time. In the planetary boundary layer (PBL), which extends from the surface up to a height that ranges from 0.1 to usually around 1 km or more (Strawbridge and Snyder, 2004), number concentrations can reach a value of 3 x 10^4 cm^{-3} in remote continental regions as presented in Figure 2.4. Jaenicke (1993) quote a concentration of 200 to 3000 cm^{-3} above the PBL up to the tropopause. Above an altitude of a few kilometers, particle concentrations are influenced little by direct emissions from the earth's surface (Jaenicke, 1993). More than 2 km above the oceans an almost constant aerosol profile concentration can be found, which supports the idea that the background aerosols reach the ocean surface at an altitude level of ~5 km (Jaenicke, 1993).

2.3 Scattering of Light by Particles

Scattering of light by particles is the source of many phenomena such as the blue colour of the sky, red sunsets or white clouds. The majority of the light does not reach our eyes directly from the source but due to scattering (McCartney, 1976). The backscatter sonde COBALD mentioned above operates with two light emitting diodes (LED) emitting at two different wavelength. The light is scattered by molecules, aerosols or cloud particles and the light scattered in backward direction is detected by COBALD. The detection geometry of COBALD which is $\Theta = 174°..\ 180°$ (See Figure 3.1) reveals angular scattering to be essential. The purpose of this section is to describe the fundamental terms and show the scattering theory by means of COBALD.

2.3.1 Basics

Matter is composed of electrically charged particles such as electrons and protons. If electromagnetic waves propagate through matter, molecules are set into oscillatory motion by the electric field of the incident wave, which in turn modify the light intensity. This is described by Beer's law which states how absorbtion of light depends on the properties of the material through which the light is traveling (McCartney (1976) and Bohren and Huffman (2004)). This modification is called extinction which is divided in scattering and absorption. The scattering coefficient (κ) is the product of number density, geometrical cross section (π x r^2) and scattering efficiency. This can be expressed by the dimensionless Mie parameter x normalising particle radius r by wavenumber λ:

$$x = \frac{2\pi r}{\lambda}. \tag{2.5}$$

The scattering pattern for spheres is symmetric with respect to the light source and therefore it is sufficient to consider only values of Θ between 0 and 180°. It is crucial to be aware of the scattering angle since the intensity for different angles vary enormously as illustrated in Figure 2.5. The forward scattering for $x \approx \lambda$, which is seen in the left part of the panel (0° until <90°), is more intense. Referring to the experimental backscatter angular range, which is illustrated in Figure 2.5 by the means of the red rectangle motivates to average the scattering efficiency over corresponding angles.

The relevant regime for COBALD is $\Theta = 174°$ to 180° and is indicated in Figure 2.5 by a red rectangle. Since COBALD's detected value is referring to a volume, we need to consider the angular coefficient, also known as volume angular scattering coefficient β^{Θ} (Bohren and Huffman, 2004). The angular scattering coefficient is defined as

$$\beta^{\Theta} = \frac{d\kappa_{sc}(\Theta)}{d\Omega}, \tag{2.6}$$

where Ω is the solid angle subtended in direction of Θ (McCartney, 1976).

Solutions to modelling scattering is found in macroscopic electromagnetic theories based on Maxwell's work. The two theories explained here are Rayleigh and Mie. This assumes only elastic scattering which means that the energy of the scattered light is the same as that of the incident beam.

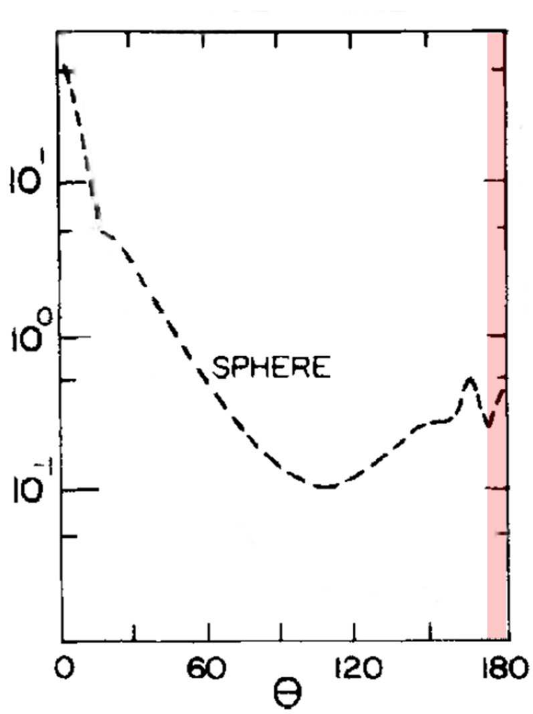

Figure 2.5: *Scattering diagram for a spheroid, adapted from Bohren and Huffman (2004). COBALD's detection regime is illustrated by the red rectangle. When the light wavelength is similar to the particle diameter the forward scattering is much more intense than the backward scattering.*

2.3.2 Mie Theory

The Mie-Theory was 1908 developed by Gustav Adolf Ludwig Mie. McCartney (1976) states that "Mie theory rigorously describes the scattering characteristics of particles for broad ranges of size and refractive index". This is illustrated in Figure 2.6 in terms of the Mie parameter. There are two limiting cases for Mie theory. The limiting case for small Mie parameters i.e. small particles is called Rayleigh theory. In the Rayleigh sector only one solution exist (McCartney, 1976). The limiting factor for high Mie parameters is termed geometrical optics. It is important to note that Mie theory is only valid for sphericals.

Generally, when a light wavelength is similar to the particle diameter, light interacts with the particle over a cross-sectional area. The cross section σ is defined as

$$\sigma = \pi r^2 Q_{sc}, \tag{2.7}$$

where r is the radius of the particle and Q_{sc} the scattering efficiency. The scattering cross section is to a very good approximation inversely proportional to λ^4. A Mie calculation output typically provides σ. Therefore this parameter is commonly divided by the geometric cross-sectional area to provide a dimensionless scattering efficiency Q_{sc}.

However, a more meaningful efficiency parameter is the scattering coefficient β^{α} defined

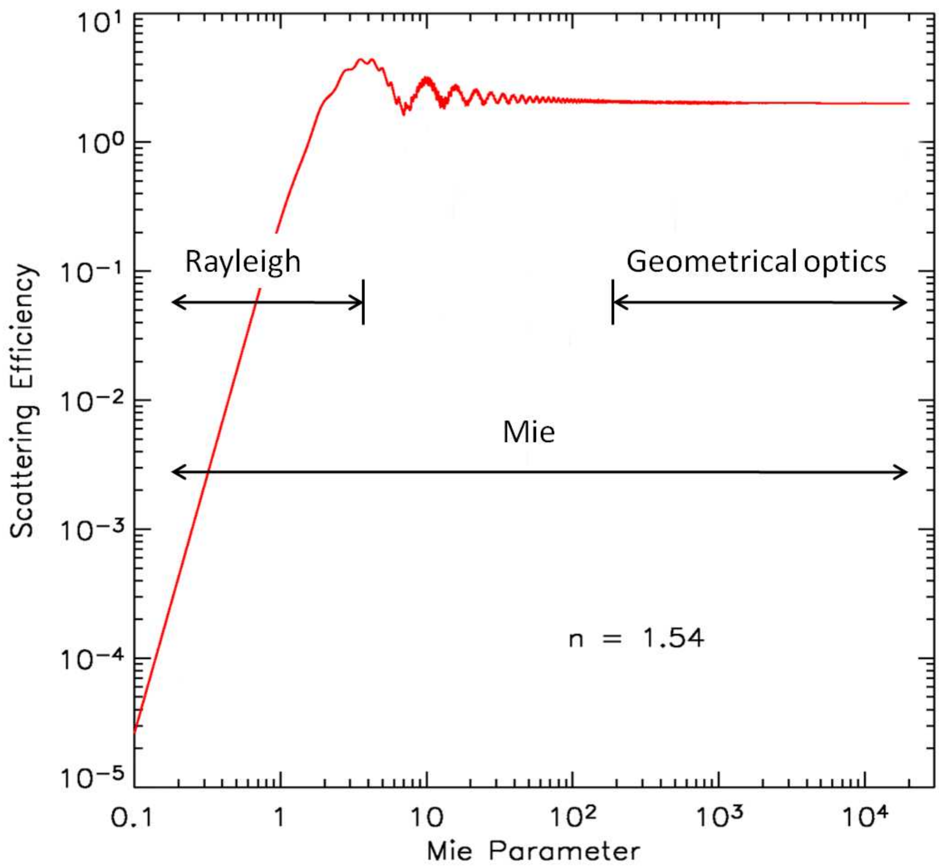

Figure 2.6: *Scattering efficiency (Q_{sc}) vs. Mie parameter with a refractive index of n = 1.54. Mie theory describes the whole Mie parameter band. Whereas Rayleigh and geometrical optics are the limiting cases of the Mie theory. Rayleigh theory is used for small particles or molecules while geometrical optics is applied for large Mie parameters.*

as

$$\beta^{\alpha} = \kappa_{sc}\frac{3}{8\pi}. \tag{2.8}$$

2.3.3 T-Matrix calculus

As mentioned above, Mie theory applies to spheres only. In chapter 4 ice particles are analysed which have different shapes as illustrated in Figure 2.7. Their shapes depend on the temperature and humidity in which they are formed. For example, thin plates and stars grow at approximately -2° while columns and needles appear near just below -5°C. Plates and stars again form near -15°C and a combination of plates and columns are formed around -30°C. In general, the diagram reveals that snow crystals tend to form simpler shapes when the humidity is low and more complex shapes at higher humidities (Libbrecht, 2005).

T-Matrix is a method to compute electromagnetic scattering by nonsperical particles based on a direct solution of Maxwell's equations (Mishchenko et al., 1996). It describes

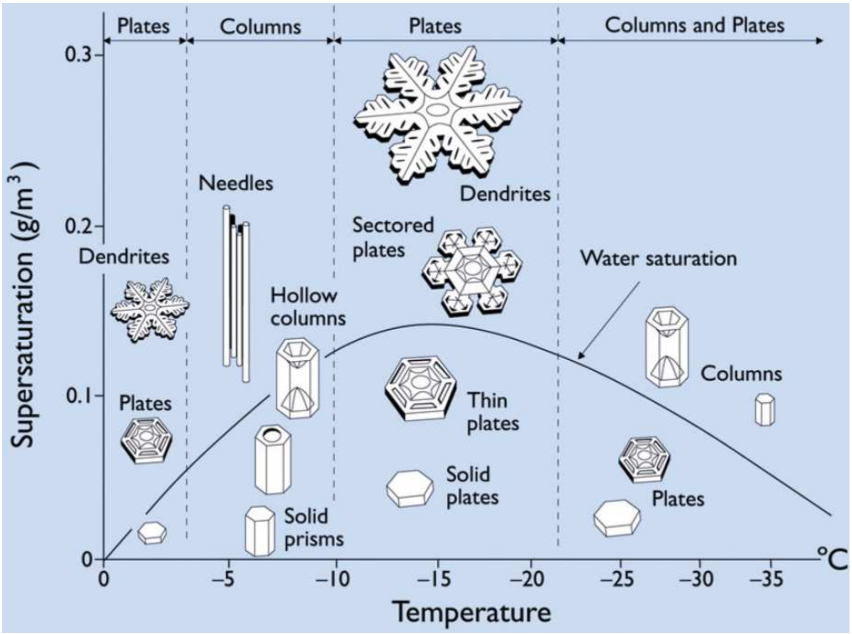

Figure 2.7: *Size and shape of ice crystals as a function of supersaturation and temperature. The graphic is taken from Libbrecht (2005).*

prolate and oblate rotational ellipsoids and cylindrical symmetry. The particles are orientationally averaged which smooths the oscillation assuming finite width in the aspect ratio. The distribution of shapes also adds to smoothing. The T-Matrix calculations have been conducted by Dr. Beiping Luo. An overview on T-Matrix calculations is given in the review paper of Mishchenko et al. (1996).

Chapter 3

Instrumentation

This Chapter provides an insight into the technique of balloon soundings and an overview of the instrumentation used. Furthermore, it describes the calibration procedure applied to the COBALD. Finally, trajectory calculation tools are introduced which are used to analyse cirrus formations in Chapter 4 and aerosol transport in Chapter 6.

3.1 Balloon Sounding

Operational radiosondes typically measure air temperature T, air pressure p and humidity, usually expressed as relative humidity with respect to liquid water (RH). Most modern sondes are equipped with a Global Positioning System (GPS) receiver whereas older sondes used radio tracking techniques to locate the sonde and to determine wind fields. Sonde data are transmitted instantaneously to a ground station through radio telemetry.

The sondes used within this thesis were carried by Totex rubber balloons filled with Helium. A typical ascent speed is 5 m/s intended to achieve good operational conditions for the sondes. The balloons used in this study burst at an altitude of approximately 30 km depending on the balloon's shape and the ratio between balloon size and payload weight.

Spichtinger (2004) points out in his dissertation that it is not possible with conventional radio soundings to distinguish between cloud-free, thin or thick cirrus clouds. Therefore the COBALD backscatter sonde was added to the payload for its cloud detection capability.

3.2 COBALD

Backscatter sondes are a valuable tool to detect cirrus clouds or to characterise in-situ aerosol or cloud particles. COBALD (Compact Optical Backscatter AerosoL Detector) is a lightweight, newly developed balloon-borne backscatter sonde designed by Dr. Frank Wienhold and tested at the Institute for Atmospheric and Climate Science (IACETH). The sonde was designed to be flown on operational weather balloons.

COBALD is based on similar principles as the backscatter sonde built at the University of Wyoming (Rosen and Kjome, 1991) which has been used extensively in field studies (Larson et al. (1994), Rosen et al. (1997), Beyerle et al. (2001) etc.). Their original design does not meet the weight restrictions for operational sounding payloads in many countries including Switzerland. The weight restriction in Switzerland is 2 kg (BAZL, 2007), accounting for potential damage to aircrafts or hazard to drop in inhabited areas.

3.2.1 Properties

The following description of COBALD is based on its data sheet (Wienhold, 2008) and on the MeteoSwiss GAW-CH Plus proposal submitted by Peter and Wienhold (2006).

Specifications

The backscatter sonde COBALD needs to be flown in combination with a radio sonde to use its telemetry. Table 3.1 shows the specifications of COBALD.

Feature	Specification	Remark
optical wavelengths	455 nm and 870 nm	
time resolution	typically 1 s	depends on the sondes default from which the telemetry is used. 0.05 s to 3 s is selectable by COBALD
dimensions	17 x 14 x 12 cm^3	includes 3 cm of thermal insulation on each side
weight with batteries	500 g	
power supply	8 x 1.5 V 2 x 9 V	for 3 h of operation
altitude range	0 to 30 km	

Table 3.1: *Specifications of COBALD based on Wienhold (2008).*

Optics

COBALD is operated with two LEDs rated to 250 mW optical power each as illustrated in Figure 3.1. The emitted light is collimated to cones of less than 4° half angle. The light backscattered from air molecules, aerosols or cloud droplets/ice particles is collected by a lens (25 mm aperture with 18 mm focal length) and focussed onto a silicon photodiode with a field of view of ±6°. The detectors signal is amplified and digitalised by a voltage to frequency converter. The dark blue and red colors in Figure 3.1 show schematically the area where the backscattered signal originates. "A good overlap between the emission and reception fields of view is established at a distance greater than 0.5 m from the sonde." (Peter and Wienhold, 2006)

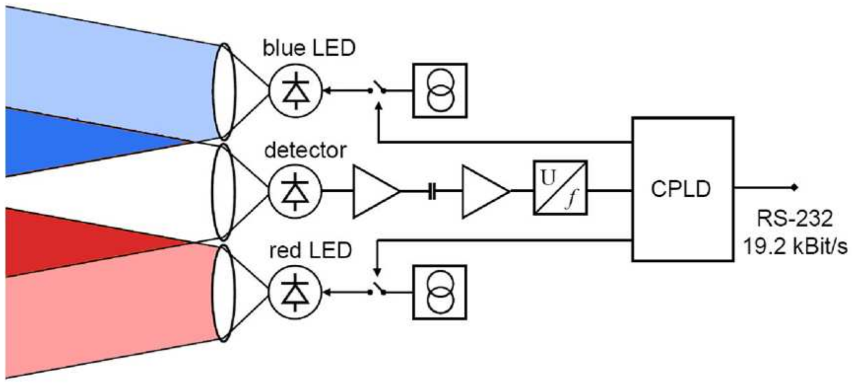

Figure 3.1: *Operation scheme of COBALD (Wienhold, private communication). The blue and red LED emit light whose backscatter is recorded by the detector. The simplified electronics displayed is explained in the text. (personal communication with Dr. Frank Wienhold.*

The blue LED emits with a wavelength of 455 nm and is confined by $\Delta\lambda_{\frac{1}{2}} = 20$ nm, whereas the red LED emits with 870 nm and a $\Delta\lambda_{\frac{1}{2}} = 50$ nm. The detector provides a high dynamic range in order to resolve molecular Rayleigh scattering which is used as a reference and to provide sufficient headroom for additional aerosol scattering. Furthermore, the detection scheme copes with the pressure span of an approximate factor 100 encountered during a balloon sounding and the resulting change in density.

Electronic configuration

A complex programmable logic device (CPLD, see Figure 3.1) modulates the two LEDs with a frequency of 300 Hz and 90° out of phase of each other. Thus, information from both optical channels is carried on the same frequency and retrieved by a phase sensitive detection scheme digitally implemented in the CPLD. The CPLD directly communicates to the monitoring computer or the sonde telemetry through a standard RS-232 interface. Daylight saturates the first amplifier stage and therefore COBALD measurements are only carried out at night, which is common for backscatter sondes.

3.2.2 Signal treatment

Backscatter data are all treated according to the procedure which was developed by Rosen and Kjome (1991). The raw data provided by COBALD sonde are counts proportional to the intensity of the backscattered light. The following subsections introduce the derived quantities which are used in this thesis.

Backscatter ratio

The raw backscatter signal is normalized to the environmental molecular scattering derived from molecular number density using temperature and pressure. This product is termed backscatter ratio (BSR). Its derivation invokes a calibration procedure explained in Chapter 3.2.3. The BSR has two contributions, the molecular Rayleigh backscatter, equaling unity by definition, and the additional aerosol/particle backscatter (ABSR =

BSR - 1).

Color index

The color index (CI) is an indicator of particle size requiring assumptions on the particle size distribution and on the refraction index. CI is defined as the ABSR in the infrared channel (870 nm) divided by the ABSR in the blue channel (455 nm):

$$CI = \frac{ABSR_{870nm}}{ABSR_{455nm}} \tag{3.1}$$

Due to this definition very small particles with respect to the wavelength approach a colour index of 1 and large particles have an index of ∼14 (Rosen and Kjome, 1991). The latter value is determined by the two wavelengths. As explained by Rosen and Kjome (1991) it is possible for the color index to significantly exceed 14 before reaching the large particle geometric value due to scattering functions oscillating around the asymptotic limit.

Figure 3.2 illustrates an example of the dependence of CI on mode radius for a lognormal distribution for the wavelengths used by COBALD. It is based on Mie calculations for spheres. The particles are assumed to have a refraction index of 1.31 (i.e. ice). An angular mean over 174 to 180° scattering angle was applied accounting for COBALDs detection geometry.

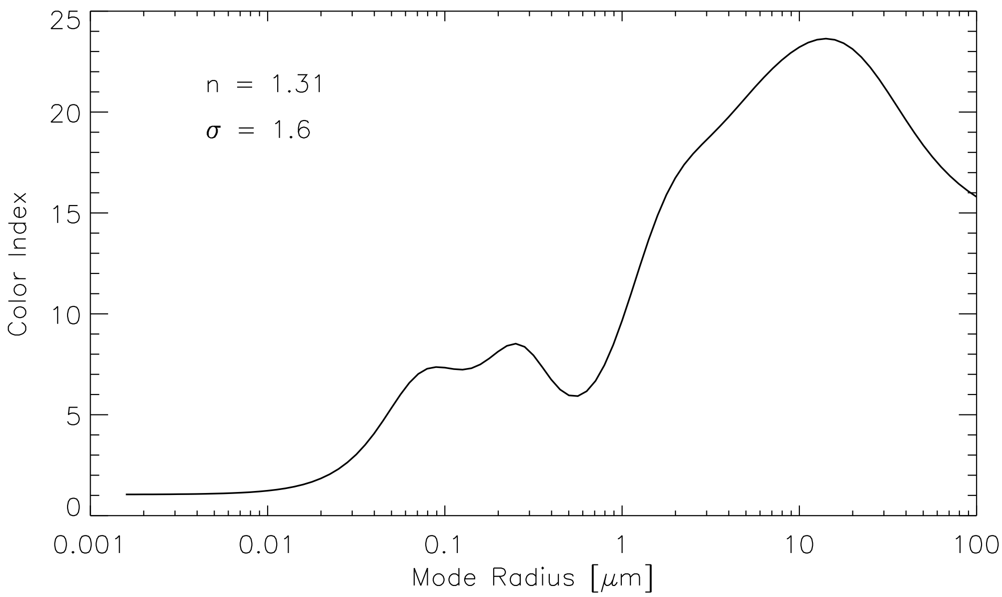

Figure 3.2: *Colour index of a lognormal aerosol distribution calculated for the COBALD wavelengths. Aerosols with an index of refraction of n = 1.31 (ice) are assumed. These calculations were carried out according to Mie theory for a lognormal distribution of spherical particles with the mode radius as indicated on the abscissa and a lognormal width of σ = 1.6.*

3.2.3 Calibration procedure

This section is based on the final Swiss National Science Foundation report (Brabec et al., 2011). Each COBALD sonde is calibrated in multiple steps based on the sounding profile data. Firstly, the blue backscatter ratio (BSR) is adjusted to minimum values of 1.05 in clean regions in the upper troposphere (source: Dr. B.P. Luo, private communication). The reference Rayleigh level of the red channel is chosen such that for all regions with the blue BSR exceeding 1.05 the minimum of the colour index (CI) does not fall below a value of five. This would imply an unrealistically high number of small particles causing the observed backscatter. This approach is justified by the analysis of stratospheric aerosol in Arctic winter measurements. To this end we investigated sounding data obtained in Sodankylä (Finland) during the 2009/2010 Arctic winter.

The left panel in Figure 3.3 shows a profile obtained in Sodankylä, Finland, on 23 January. It shows the temperature in black, the blue and red BSR and the calculated CI. The black dotted line indicates the 1.05 BSR level, which corresponds to the reference Rayleigh level mentioned above. The dashed line shows a BSR of 1. In general, the profile shows a very clean troposphere. Upon entering the lower stratosphere which is marked magenta on the left pressure axis, the blue and red BSRs rise due to stratospheric aerosols. A polar stratospheric cloud (PSC) can be seen between 85 to 15 hPa identified by cyan color.

With a lognormal width for the particle size distribution assumed to be 1.6, the mode radius would be between 0.1 and 0.2 μm shown in the right panel of Figure 3.3. These number densities compare well with our general understanding. Modeling results published in the SPARC Report No. 4 (February 2006) shown in Figure 3.4 provide estimates for particle number densities and effective radii as a function of latitude and altitude (annual mean). For comparison with the sounding in Figure 3.3, the blue vertical lines represent the latitude of Sodankylä (Finland, lat: 67°25'N/ lon: 29°36'E) and the red ovals highlight the lower stratosphere. Typical number densities are about 20 cm^{-3} and typical effective radii about 0.16 μm.

The calibration procedure is confirmed by modelling results and thus, it is applied to all BSR profiles in this thesis.

3.3 Hygrometers

There are different ways of measuring RH. In this thesis only balloon borne frostpoint hygrometers were used. Two of the three sondes applied, the Cryogenic Frostpoint Hygrometer and SnowWhite, were involved in an intercomparison campaign in the AIDA chamber and obtained accurate results (accuracy < 10 % in RHi). A description of the AIDA chamber intercomparison and the instrumental results can be found in Möhler et al. (2009).

3.3.1 Frostpoint hygrometers

Frostpoint Hygrometers are based on the chilled-mirror principle. The temperature of a mirror is controlled with an opto-electronic feedback detection system such that the

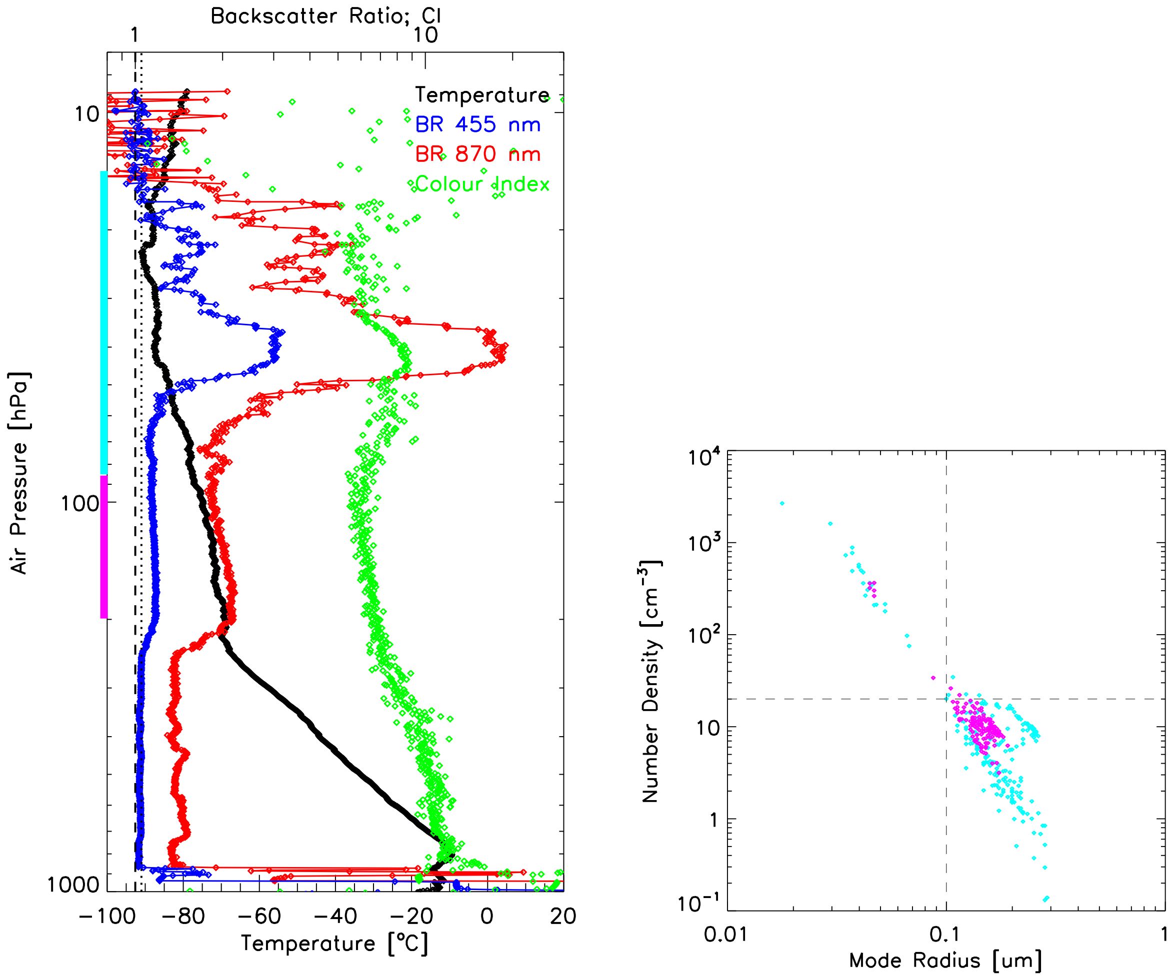

Figure 3.3: *Sounding in Sodankylä, Finland, on 23 January 2010 in the left panel. The profile shows backscatter ratios at 455 nm (blue dots), 870 nm (red dots), colour index (green dots) and temperature (black line). The lower stratosphere (magenta) and the polar stratospheric cloud region (PSC, cyan) is highlighted on the left pressure axis. The corresponding colours (magenta and cyan) to these regions are used in the right panel that shows number density vs. mode radius calculated with Mie theory for altitudes between 15 and 85 hPa (cyan) and between 85 and 200 hPa (purple).*

mirror maintains a thin and constant layer of liquid or solid condensate. The measured temperature then corresponds to the dew or frostpoint temperature depending on the phase of the condensate on the mirror (Wiederhold, 1997).

SnowWhite

The SnowWhite frostpoint hygrometer, which is produced by Meteolabor AG, Switzerland, uses a single-stage thermoelectric Peltier device to cool the mirror (Fujiwara et al. (2003), Vömel et al. (2003), Miloshevich et al. (2006)).

The SnowWhite measurement accuracy is comparable to the state-of-the-art Cryogenic Frostpoint Hygrometer (CFH, described below) as stated by Miloshevich et al. (2006). But 3 limiting factors are descbibed by Vömel et al. (2003) which have to be taken into account by interpreting measurements.

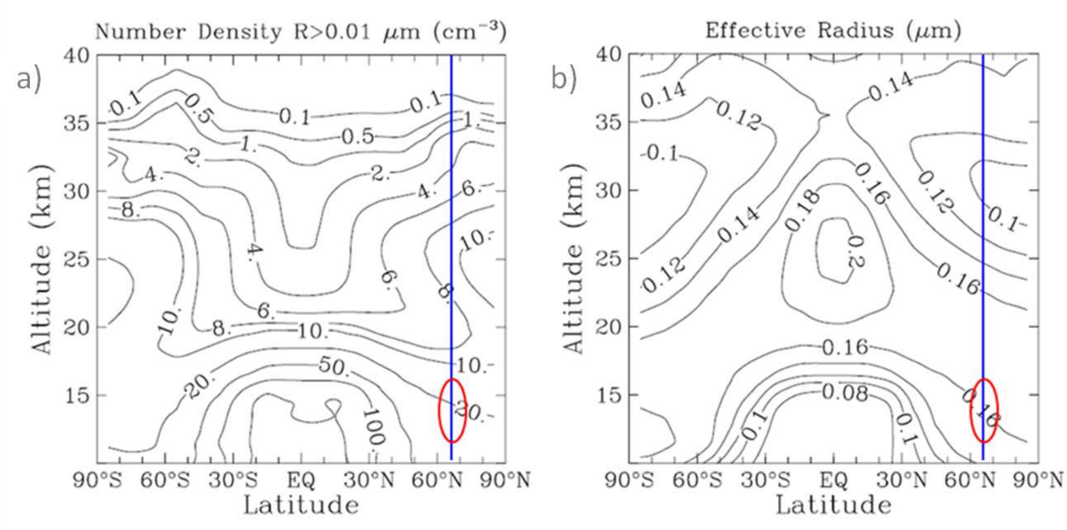

Figure 3.4: *Model-calculated annual average morphology of the stratospheric aerosol layer showing (a) number density (cm^{-3}) for particles greater than 0.01 μm radius, and (b) effective radius (μm) from the AER model (described in Weisenstein et al. (1997)) between 10 and 40 km. Adapted from SPARC report No. 4 (2006).*

(1) The lower RH detection limit is approximately 6% RH.

(2) When the frostpoint hygrometer traverses through vast dry layers below the RH detection limit the frost layer on the mirror disappears.

(3) in the UT, a either dry or wet bias is occasionally observed which is thought to be caused by instability in the controller at low temperatures leading to unreliable measurements below -70°C (personal communication with Dr. Vömel 2011).

Due to limits mentioned we only applied SnowWhite sondes with diagnostic channels which give indications for some malfunctions.

"Meteolabor specifies 0.2°C for both frost point temperature precision and accuracy leading to a total error of about 5 % (depending on temperature) in the water vapor mixing ratio" (Möhler et al., 2009).

Cryogenic Frostpoint Hygrometers

Cryogenic frostpoint hygrometers use cryogenic cooling to cool and a powerful heater is used against this cold sink to control the mirror temperature. Two stainless steel tubes extending beyond the top and bottom of the instrument prevent contamination ((Vömel et al., 2007a) and (Vömel et al., 2007b)).

Two different types of cryogenic frostpoint hygrometers were used within this thesis. Both, the NOAA frostpoint hygrometer (NOAA-FPH) and the Cryogenic Frostpoint Hygrometer (CFH) are based on the former NOAA/CMDL instrument.

Vömel et al. (1995) states that the accuracy of the instrument depends mainly on the thermistor calibration, the stability of the controller, the measurement error and the digitizing error. The overall accuracy of the measured frost point temperature is assumed to be 0.5°C, which is less than 10% in the upper troposphere.

Further details are found in Vömel et al. (1995), Vömel et al. (2003) and Vömel et al.

(2007b).

3.4 Trajectory calculations

To support the analysis of cirrus clouds (Chapter 4) and identify source regions of aerosols (Chapter 6), trajectory calculations were carried out.

To calculate air parcel trajectories, high-resolution wind fields such as those from ECMWF or COSMO-7 are essential. Furthermore, a calculation transport model is needed whereas in this thesis LAGRANTO is used. Besides that, a microphysical box model is applied in Chapter 4 which simulates the nucleation and growth process of ice particles. The results are compared with the LAGRANTO output and sounding measurements. Both the wind fields and the trajectory calculation models are explained in this section.

3.4.1 Wind fields

ECMWF analysis data

The European Centre for Medium-Range Weather Forecasts (ECMWF) operational analysis data are based on 4D variational assimilation (4DVAR) which uses the "Integrated Forecast System" (IFS) model as part of the assimilation system. The analysis can be thought of as being the best estimate state of the model that is most consistent with all observations (personal communication with Richard Forbes from ECMWF). The spatial resolution of the operational analysis data is 1° x 1° horizontally with 91 layers rising up to 0.01 hPa which compare with about 80 km altitude. The operational ECMWF analysis data reflects specific humidity q qualitatively well (Overlaz et al., 2000), but absolute values can not be assumed accurate (Overlaz and van Velthoven, 1997). ECMWF analysis data cover the whole globe.

Operational analysis data from ECMWF was applied to the work described in Chapter 4 and 6.

Microphysical cloud model

The microphysical cloud model, designed by Dr. B. Luo, is designed to simulate nucleation and models exchange of water between gas and condensed phase based on the diffusion equation (with an accommodation coefficient $\alpha = 1$) Hoyle et al. (2005). The model consists of vertically stacked boxes forming a column. Each box simulates conditions experienced by air parcels following temperature and pressure data along trajectories. The initial particle distribution is chosen as lognormal with a mode radius of 0.06 μm, a number density of 200 cm^{-3} and a lognormal width of σ=1.8 (personal communication with Dr. B. Luo). Homogeneous nucleation rates embedded correspond to the theory of Koop et al. (2000). Once ice particles are formed they take up water vapour from the gas phase at the expense of the liquid particles existing so far (Bergeron-Findeisen effect (Seinfeld and Pandis, 1998)) and eventually depleting ice supersaturation. The ice particles sediment and fall with a terminal velocity depending on the particle size as described in Section 2.1.4.

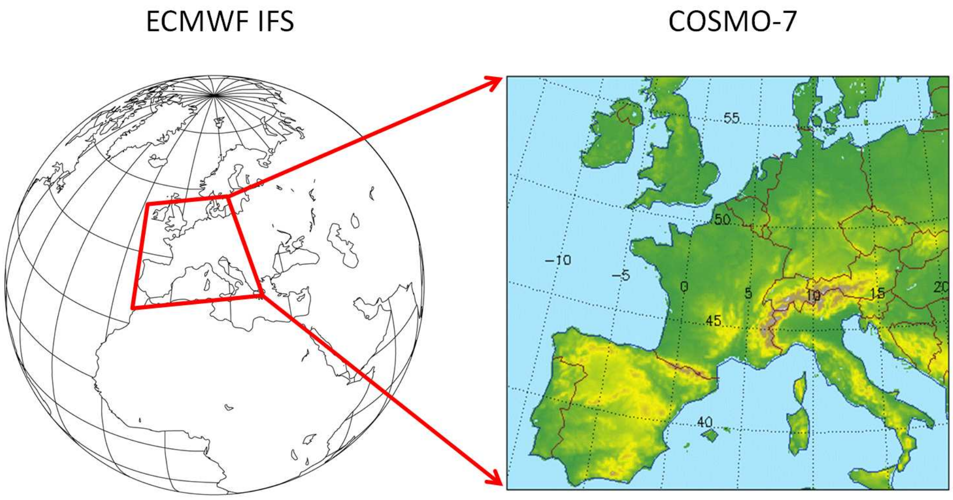

Figure 3.5: *Spatial domains of ECMWF and COSMO-7. ECMWF is a global model while COSMO-7 is regional. Globe: copyright Bruce Jones Design Inc. 2009, Europe map: webpage COSMO (2010)).*

Further details of the model are given in Luo et al. (2003) and Hoyle et al. (2005). The model is used to explore the cloud properties in Chapter 4 and to compare with measurements in chapter 5.

COSMO-7 analysis data

COSMO stands for COnsortium for Small-scale MOdelling. Number 7 reflects the spatial resolution of a 6.6 x 6.6 km grid. In vertical direction the model has 60 levels reaching an altitude of approximately 23 km.

The COSMO model was initially based on the "Local-Model" (LM) of DWD with its corresponding data assimilation system (formerly called "LM" until 2007 (COSMO, 2010)). Its aim is to have a realistic simulation of small-scale physical processes by using up-to-date physical parameterisations and numerics. Moreover, COSMO-7 is organised in an international framework and runs a short-range forecasting model as described in Steppeler et al. (2003). The lateral boundary fields for COSMO-7 are provided by the ECMWF model. Detailed information can be found on their webpage (COSMO, 2010).

COSMO-7 is chosen regional by MeteoSwiss with Switzerland in its centre. Figure 3.5 illustrates its extensions compared to ECMWF.

3.4.2 Trajectory calculation models

LAGRANTO

The LAGRangian ANalysis TOol (LAGRANTO) allows the identification of air mass source regions and is described in detail by Wernli and Davies (1997). To drive the trajectory calculations, analysis input wind fields are needed such as ECMWF or COSMO. The analysis fields are interpolated linearly in space and time using the two nearest analysis fields (Wernli and Davies, 1997).

In this thesis LAGRANTO was applied in Chapter 4 to support the analysis of cirrus cloud formation.

Chapter 4

A case study of particle backscatter and relative humidity measured across cirrus clouds and comparison with state-of-the-art cirrus modelling

This chapter is a paper draft.

M. Brabec*, F. G. Wienhold*, B. Luo*, H. Vömel+, F. Immler+, P. Baumann°, T. Peter*

* Institute for Atmospheric and Climate Science (IAC), ETH Zurich, Switzerland
+ Deutscher Wetterdienst, Germany
° Meteo Swiss, Switzerland

The layout of the article as well as the section and figure numbering have been adapted to match with the thesis structure.

Abstract

The newly developed balloon-borne backscatter sonde COBALD (Compact Optical Backscatter and AerosoL Detector) was flown 14 times together with a CFH (Cryogenic Frostpoint Hygrometer) from Lindenberg, Germany (52.21°N, 14.12°E) in November 2008. The soundings were part of the "Lindenberg Upper-Air Methods Intercomparison" (LUAMI) campaign with the aim to investigate state-of-the-art instrumentation for cirrus cloud measurements in the midlatitude upper troposphere. The COBALD-CFH tandem is shown to be an excellent payload to determine the partitioning of atmospheric water between the gas phase and the condensed ice phase in and around cirrus clouds, and thus to detect in-cloud and out-of-cloud supersaturations with respect to ice. The case discussed here in detail is characterised by very little horizontal wind shear, making it ideal for detailed testing of cirrus modelling. We show that operational analysis data of ECMWF (1°x1° spatial resolution, 6-hourly stored fields) fail to represent important cloud properties, such as ice water contents or relative humidities, whereas COSMO-7 fields (6.6 x 6.6 km, hourly) provide a much better agreement with the humidity measurements, though the profile of the ice water content is not captured accurately. The main difference between the ECMWF and the COSMO data are the resolution of small-scale vertical winds, which allows the mesoscale model to better represent cirrus nucleation and growth processes, and better mesoscale representation of mixing processes resulting in a more accurate representation of relative humidity. Comprehensive microphysical cloud model calculations along LAGRANTO trajectories based on COSMO-7 wind and temperature fields allow an estimation of humidity, ice particle size, number density and backscatter ratio which turned out to be in agreement with the observed cirrus clouds.

4.1 Introduction

Water vapour is a key element in the Earth's climate system, in everyday weather and in atmospheric chemistry. Dehydration mechanisms driven by the formation of visible and subvisible cirrus clouds, determine the atmospheric water vapour budget and thus the chemical and radiative properties of the upper troposphere and stratosphere. Though still uncertain, the role of cirrus clouds is of particular importance in the Earth's climate system due to their poorly characterised radiative properties and microphysics (Christensen et al., 2007). Approximately 30% of the Earth is covered with cirrus clouds, which can influence the radiative budget by altering both the reflectivity for incoming solar radiation and the emission of outgoing infrared radiation (Joos et al., 2008). These characteristics highly motivate cirrus cloud studies.

This work describes a case study based on vertical profiles of water vapour and particle backscatter collected at the meteorological observatory (52.21°N, 14.12°E) at Lindenberg, Germany on 6 November 2008. The data from the newly developed backscatter sonde, COBALD and the Cryogenic Frostpoint Hygrometer are considered for the analysis. Moreover, CFH provides highly accurate measurements at cirrus altitudes (Möhler et al., 2009). Spichtinger et al. (2005a) claim that one of the shortcomings of radiosonde data is the lack of knowledge whether the measurements took place in clear sky or in cirrus clouds. COBALD's application as a cloud detector provides this information which was previously unavailable, proving the backscatter sensor to be an essential tool.

When analysing cirrus clouds, it is useful to conduct detailed case studies. This study aims to explore the ability of models to represent in-situ measurements and explaining micro physical processes. We investigate LAGRANTO trajectories calculated using two different input wind fields, namely ECMWF and COSMO-7. A microphysical box model using the trajectory temperature and pressure data was applied to explore the clouds' properties.

4.2 Instrumentation and models description

The following chapter describes COBALD and CFH and the treatment of their data. COSMO and ECMWF analysis data and the LAGRangian ANalysis TOol (LAGRANTO), a trajectory calculation model, are also described in this chapter (Wernli and Davies, 1997). Finally, a microphysical Lagrangian box model is introduced which is used to describe microphysical processes.

4.2.1 COBALD

COBALD is a lightweight, newly developed backscatter sonde designed to be flown on operational weather balloons. It is based on similar principles as the Wyoming backscatter sonde (Rosen and Kjome, 1991) which has been used extensively in field studies (such as Larson et al. (1994), Larson et al. (1995), Rosen et al. (1997), Beyerle et al. (2001)). COBALD uses two high power (250 mW) LEDs at wavelengths centered at 455 nm (blue) and 870 nm (infrared). A silicon detector detects backscattered light from air molecules, aerosols or cloud droplets/ice particles from both sources. The data treatment is based on the procedure developed by Rosen and Kjome (1991).

Backscatter ratio

The raw backscatter signal is normalised to the environmental molecular scattering, derived from molecular number density, using ambient temperature and pressure. This product is termed backscatter ratio (BSR). Its derivation is based on the calibration procedure described in Chapter 3. The BSR has two contributions, the molecular Rayleigh part, equaling unity by definition, and the additional aerosol/particle backscatter (ABSR = BSR - 1). In this study, the BSR signal is used to quantify cirrus clouds.

IWC estimation with BSR signal

Figure 4.1 shows simulated BSR for different mode radii and 1 ppm water in form of ice. The assumed conditions are a lognormal distribution, a particle width of σ=1.4, a refractive index of 1.31 and an aspherical ratio of A=0.75. Assuming a mode radius of 30 μm for the observed ice particles the BSR_{870} signal would be two. Taking as example a value of 70 for the measured BSR_{870} the resulting ice water mixing ratio would be 35 ppm corresponding to $\sim$20x10^{-3} g/kg. For ice particles with a mode radius of 10μm the same BSR_{870} signal leads to an ice water content (IWC) of $\sim$10x10^{-3} g/kg. These two IWC values are taken for the upper and lower limit for cloud 'A'.

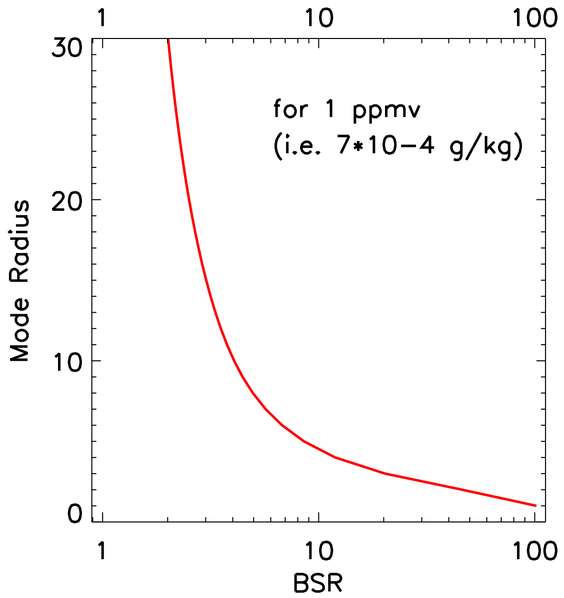

Figure 4.1: *Simulated BSR for 1 ppm ice water dependent on different mode radii for a wavelength of 870 nm.*

Similar calculations for cloud 'B' (See Figure 4.2)yields a lower and upper limit of $\sim$3x10^{-3} and $\sim$1.5x10^{-3}, respectively. Assuming a mode radius between 10 and 30 μm allows to estimate IWC with an uncertainty of factor 2.

4.2.2 Cryogenic Frostpoint Hygrometer (CFH)

The CFH was developed by Dr. Holger Vömel (DWD, Germany) and defines the state-of-the-art measurement technology for atmospheric water vapour. Its design is based on the former NOAA/CMDL frost point hygrometer, with improved accuracy. Frostpoint Hygrometers operate by cooling a mirror which is controlled with an opto-electronic feedback to maintain a constant layer of condensed or frozen coverage. The mirror temperature corresponds to the dew or frost point temperature (TF) of the gas passing over the mirror depending on the phase of the condensate (Wiederhold, 1997).

We calculate relative humidity with respect to ice according to its definition:

$$RHi_{CFH} = \frac{e_{TF}}{e_T} \tag{4.1}$$

where e_{TF} is the water vapour partial pressure derived from the frost point temperature, which is divided by the saturation vapour pressure at the measured ambient temperature (e_T). Vapour pressure is determined from the Murphy and Koop (2005) saturation vapour pressure formula. The uncertainty of the frostpoint measurement is approximately 0.5°C, a conservative estimate that covers our altitude range and has been described by Vömel et al. (2007a). With the uncertainty of 0.2°C in air temperature measurement the relative humidity uncertainty is determined by Vömel et al. (2007a) "as the % fraction of the RH; that is, a 4% uncertainty at saturation is equal to an uncertainty of 4% RH, whereas at an RH value of 10% this same 4% uncertainty of the RH percentage value is only 0.4% RH."

4.2.3 Trajectory calculations

Trajectories are calculated with the three dimensional LAGRangian ANalysis TOol (LAGRANTO) which allows the identification of air mass source regions and is explained in detail by Wernli and Davies (1997).

LAGRANTO needs input data such as "European Centre for Medium-Range Weather Forecasts" (ECMWF) or "COnsortium for Small-scale MOdelling -7" (COSMO-7) operational analysis wind field data. The spatial resolution of the operational analysis data of ECMWF is 1° x 1° (corresponding to ~78 x ~100 km at midlatitudes) horizontally with 91 layers up to 0.01 hPa (approximately 80 km altitude). The time resolution of ECMWF data is 6 hours with analysis data available at 00, 06, 12 and 18 UTC.

COSMO-7 uses a spatial resolution of 6.6 x 6.6 km. The model has 60 levels which reach an altitude of approximately 23 km and provides hourly data.

4.2.4 Microphysical column model

The microphysical column model simulates exchange of water between gas and condensed phase based on the diffusion equation allowing for a much more detailed physical treatment as compared to the schemes used in ECMWF or COSMO-7. Multiple box models, each driven by temperature and pressure data from a LAGRANTO trajectory, represent the particle distribution in a Lagrangian framework: for each prescribed initial distribution, the size evolution resulting from diffusion limited condensation (or evaporation) is followed in time together with the corresponding changes of water vapour in the gas phase. This approach avoids redistributions of particle number density on a fixed Eulerian grid after each internal time step together with the associated "numeric diffusion". The initial particle distribution is chosen as lognormal with a mode radius of r=0.06 μm, a lognormal width of σ=1.8 and a total number density of 200 cm^{-3} (personal communication with Dr. B. Luo) based on typical observations at suitable trajectory points with no indications of condensed water vapour from the underlying NWP model. Following Koop et al. (2000) nucleation rates are evaluated from saturation and temperature in order to create ice particles within a homogeneous nucleation scheme. Once formed, ice particles compete in uptake of water vapour from the gas phase at the expense of the liquid particles existing so far called the Bergeron-Findeisen effect (Seinfeld and Pandis, 1998) eventually depleting ice supersaturation. Together with the nucleation scheme the diffusion limited treatment yields a realistic ice particle size distribution and number density depending on the cooling rates as prescribed by the trajectories, e.g. Hoyle et al. (2005). To address vertical particle redistribution within the cloud these box models are stacked upon one another following trajectories at 500 m altitude difference between 8 km and 11 km with particles removed according to their size dependent sedimentation speed and reinjected to the box below.

To this end certain constraints on homogeneous homogeneity of the layers versus vertical wind shear are required which was given in this case study. Particle coagulation is not yet treated in the model and lead to larger particles and therefore larger terminal velocities. Due to larger particles it leads to smaller BSR signals. Further specifications of the model are given in Luo et al. (2003) and Hoyle et al. (2005).

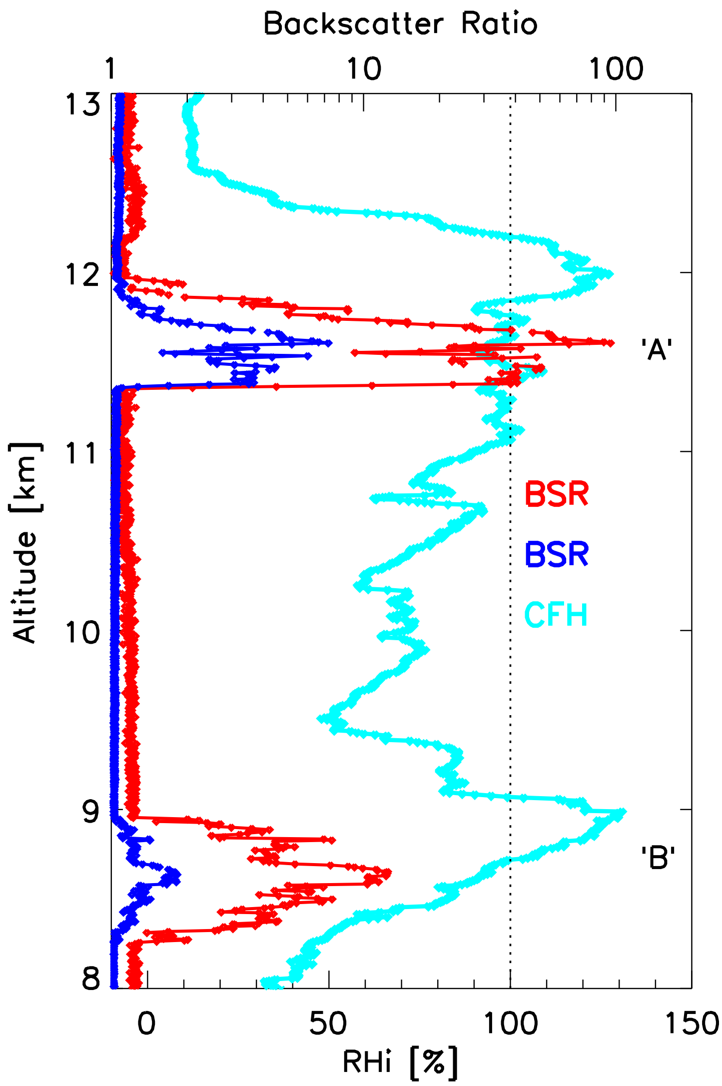

Figure 4.2: *A segment of a balloon sounding profile on 6 November 2008 above Lindenberg, Germany. COBALD's* BSR_{455} *and* BSR_{870} *are represented in blue and red, respectively.* RH*i obtained by CFH is plotted in cyan. The upper cloud is termed 'A' and the lower 'B'. The data is binned to 5 seconds time intervals corresponding to a vertical resolution of 25 m at an ascent rate of 5 m/s.*

4.3 Observations

COBALD and CFH were launched on the same payload in Lindenberg on 5 November 2008 at 11pm UTC, measuring particle backscatter ratios and RHi (Figure 4.2) showing two layers of cirrus clouds. The upper cirrus 'A' is approximately 400 m thick, with a clearly defined lower edge at 11400 m and a less distinct upper edge. In and below the cloud the gas phase is saturated with respect to ice (CFH measurements in cyan), while a layer extending roughly 300 m above the cloud reveals a supersaturation of up to ~25 %. The second cirrus layer 'B' has its lower limit at 8300 m and exhibits approximately the same vertical thickness as the upper cloud. Cloud 'B' was measured at 0.36 UTC and

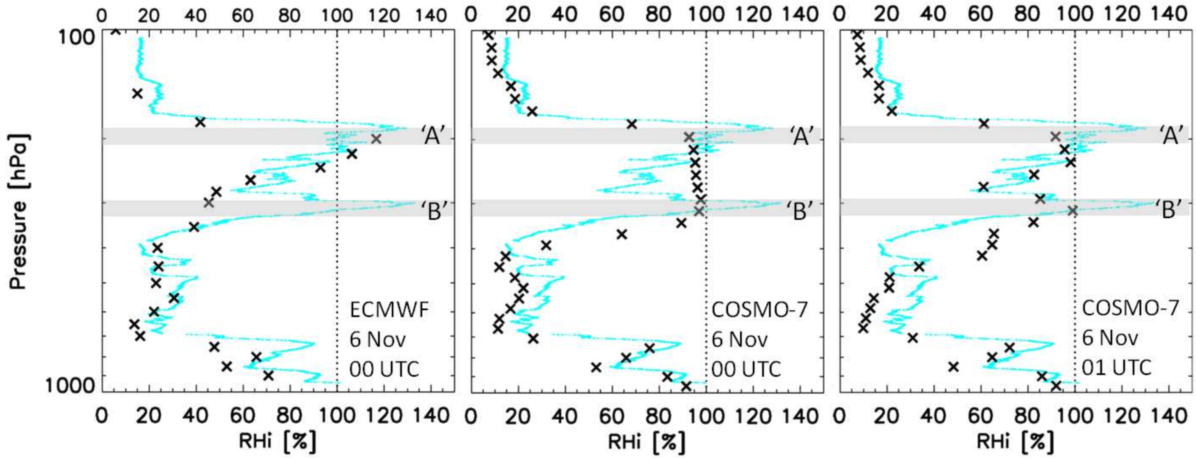

Figure 4.3: *Pressure vs. RHi profiles of ECMWF (00 UTC) and COSMO-7 (00 and 01 UTC) analyses data (black crosses) above Lindenberg on 6 November 2008. The cyan profiles show RHi measured by CFH. The grey horizontal bars represent the altitude of the detected cloud. ECMWF depicts a supersaturation within the upper cloud 'A' but does not resolve cloud 'B' (RHi < 45%). COSMO-7 depicts only one big layer (320-190 hPa) near saturation at 00 UTC. One hour later at 01 UTC two saturated layers are shown in the measured cloud altitude ranges.*

cloud 'A' at 0.44 UTC on 6 November 2008. The weather situation is characterized by very little horizontal wind shear, making it ideal for detailed testing of cirrus modelling using the approach described in Section 4.5.1.

In the absence of COBALDs BSR, it would not be possible to determine the borders of the two cirrus clouds and e.g. to reveal for cloud 'B' half of the supersaturated part is within the cloud and the other half above. This demonstrates that adding COBALD to the balloon payload is essential for localising, and therefore analysing cirrus properly.

4.4 Comparison of Measurements and synoptic/mesoscale models

Black crosses in Figure 4.3 indicate the RHi profiles of ECMWF (00 UTC) and COSMO-7 (00 UTC and 01 UTC) operational analysis data above Lindenberg, Germany on 6 November 2008. The horizontal bars show the location of the cloud deduced from the backscatter measurements and the cyan lines represent RHi of CFH. ECMWF data (left panel) show a supersaturation of 17 % within the cloud compared to a measured RHi mean of 101 % within the cloud. COSMO-7 at 00 UTC (middle panel) shows one layer near saturation spreading from approximately 300 to 200 hPa covering both clouds regions. At 01 UTC two RHi layers are visible which are close to saturation and match with the average $\bar{x}$ value of cloud 'A' ($\bar{x}$=92%) and 'B' ($\bar{x}$=101%) with a deviation of less than 10%.

IWC was analysed to investigate if the model analysis data agrees within the IWC range estimated from the cirrus cloud backscatter signal (Section 4.2.1). Figure 4.4 shows ECMWF and COSMO-7 (00 and 01 UTC) IWC values as black crosses. The horizontal grey bars indicate the altitude of the clouds and coloured horizontal lines represent es-

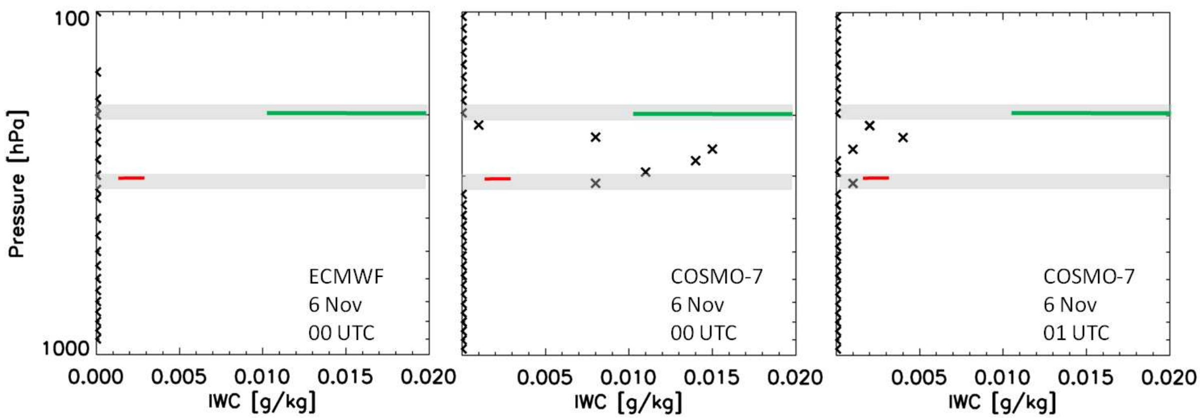

Figure 4.4: *IWC profiles of ECMWF (00 UTC) and COSMO-7 (00 and 01 UTC) are illustrated with black crosses. ECMWF (left panel) exhibits no IWC. COSMO-7 data at 00 UTC (middle panel) shows one ice cloud located below the lower edge of cloud 'A', between 'A' and 'B' and within cirrus 'B'. COSMO-7 (01 UTC) represents cloud 'A' at lower altitude whereas cloud 'B' is located at the same altitude as in the measurements. The green and red lines represent the estimated IWC by COBALD described in Section 4.2.1.*

timates of IWC based on BSR_{870} data (see Section 4.2.1 for description). As seen from the left panel no ice exists in the ECMWF data. COSMO-7 at 00 UTC (middle panel) represents one cloud reaching from approximately 300 to 200 hPa. The IWC values of the model compare with the backscatter estimate, for the upper cloud 'A' but disagree for cloud 'B'. At 01 UTC two cloud layers are present but both appear to underestimate the IWC.

In conclusion, COSMO-7 (01 UTC) analysis data reveals two RHi layers close to the average values of the measured cloud and represent CFHs RHi more adequate than ECMWF and COSMO-7 (00 UTC). It is a common feature that ECMWF underestimates humidity (Tompkins et al., 2007). COSMO-7 (01 UTC) shows as the only model data set two ice layers but underestimates IWC compared to the values estimated from BSR_{red}. COSMO-7 (01 UTC) is also closest to the observation time.

4.5 Trajectory based discussions of model processes

This section discusses LAGRANTO trajectory calculations based on ECMWF (00 UTC) and COSMO-7 (01 UTC) operational analysis data.

LAGRANTO back trajectories based on ECMWF operational analysis data were calculated starting above Lindenberg, Germany on 6 November 2008, 00 UTC (Figure 4.5). The selected starting time of the trajectories is closest to the measurements but exhibit a time shift of 36 minutes to cloud 'B' and 44 minutes to cloud 'A'. Greenish colours represent back trajectories for cloud 'A' and redish for cloud 'B', and the connecting line between two triangles represent one day. The left panel shows that 5 days before the observation the majority of the measured air is on the western side of the Atlantic Ocean carried towards Great Britain. Before reaching Great Britain, the air flows in a southerly direction due to a low pressure system over France. The air parcels then passed over the north western part of the African continent towards the Mediterranean Sea. Before

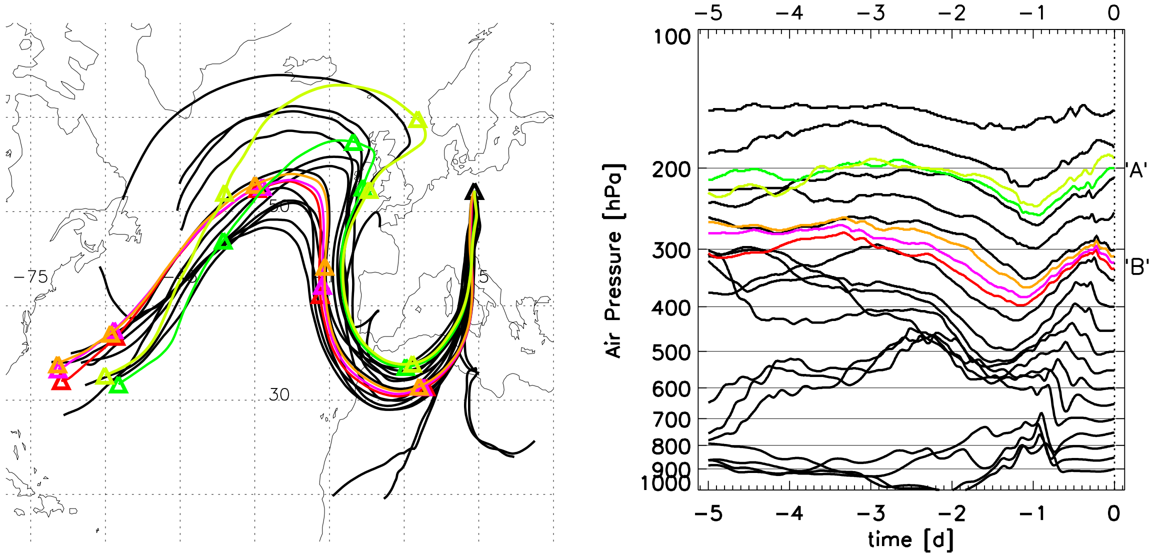

Figure 4.5: *Back trajectories computed by LAGRANTO based on ECMWF operational analysis data. In the left panel a geographical overview is given with the coloured trajectories indicating the cirrus clouds detected by COBALD above Lindenberg at time = 0. Greenish coloured trajectories represent cloud 'A' and redish ones cloud 'B'. All coloured trajectories bear triangles marking one day time intervals. Trajectories outside the cloud are shown in black to complete the picture. The x-axis on the right panel shows the calculated days starting above Lindenberg (t = 0) going back 5 days.*

reaching Lindenberg, the air parcels traversed the Alps. The lowest four trajectories are an exception having their origin on the African continent and is a sign for being inside the boundary layer. The right panel in Figure 4.5 represents an altitude profile starting from above Lindenberg where the sounding was performed (time = 0) reaching 5 days back in time. As can be inferred from the distortion in the alpine regions air parcels in the centre of the profile are fastest, the further away from the centre air parcels are becoming slower (not shown here). The slower trajectories near the ground are lifted at approximately -2 days while passing over the Alps, and influence the upper air parcels.

In Figure 4.6 only coloured (in-cloud) trajectories of Figure 4.5 are displayed. Cloud measurements are indicated as arrows and IWC estimations based on assumptions (see Section 4.1 for details) are depicted with vertical two-headed arrows. RHi of the air parcels increased while passing over the Atlantic Ocean in the time period from -5 to -3 days, visible in the left upper panel. This is attributed to decreasing temperature during that time period (upper right panel). Ice crystals formed in cloud 'A' (lower left panel) during that time section, however they disappear in the next data point. From -3 days until approximately -1 day, the air parcels descended into higher pressure levels where the increasing temperature reduced RHi.

During the last day RHi increased due to cooling by adiabatic expansion associated with the lift of the air mass by the Alps. This might have initialised an inertial gravity wave which likely triggers cirrus clouds as descibed in Spichtinger et al. (2005b). Opposite to the situation in cloud 'A' where the simulations match the observations, RHi in cloud 'B' decreased during the last part of the last day caused by the air mass descent and therefore leading to an underestimation of more than 45 % RHi. The back trajectory of water vapour mixing ratio (Figure 4.5 lower left panel) shows a lower variability for cloud

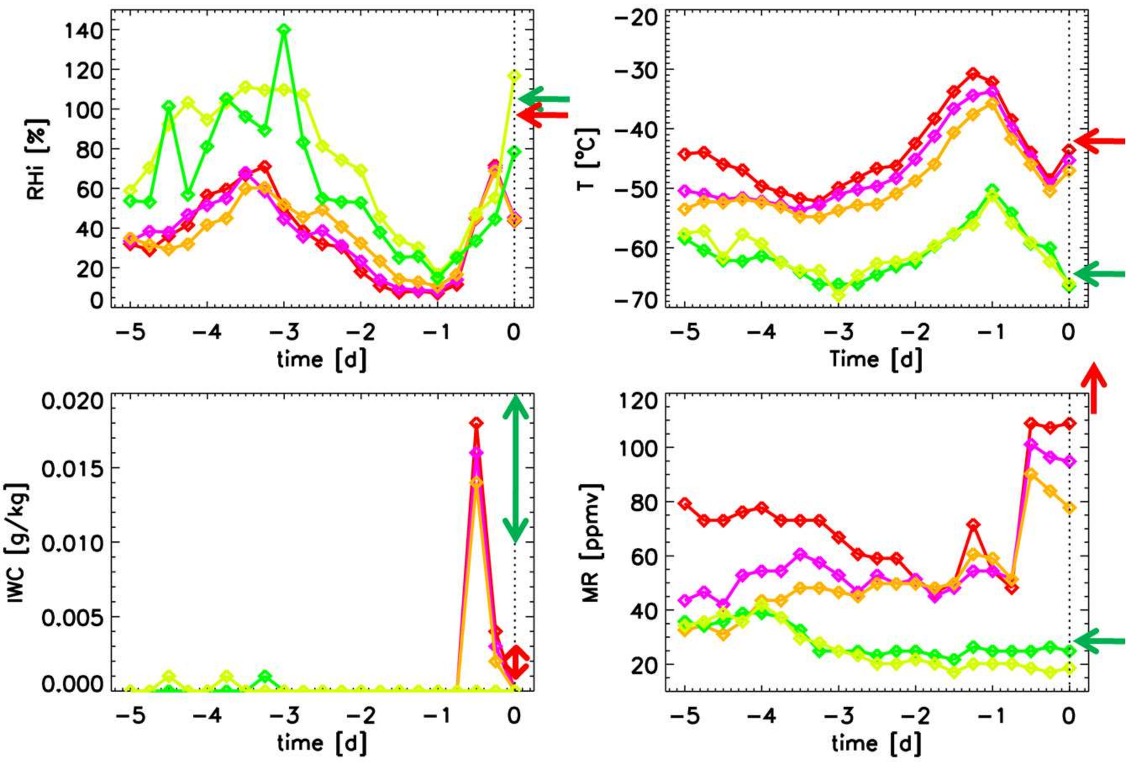

Figure 4.6: *The here presented ECMWF 5 days back trajectories refer to the colour code in Figure 4.5. Only in-cloud trajectories of the upper cloud 'A' (greenish colours) and lower cloud 'B' (redish colours) are presented. The x-axes show backward time, starting from t=0 above Lindenberg. The arrows on the right edge of the panels are the mean measured values within the cloud. The red arrow in the lower right panel showing upward illustrates that the measured mixing ratio value (293 ppmv) is larger than the scale. The vertical double-arrows for IWC are deduced from the BSR signal of COBALD (see Section 4.2.1 for description).*

'A' compared to cloud 'B'. In cloud 'B' the mixing ratio increased by almost 60 ppmv during the last day caused by an increased water vapour supply to the air mass while passing over the Mediterranean Sea. This statement is supported by the "Cloud-Aerosol Lidar and Infrared Pathfinder Satellite Observations" (CALIPSO) data. The data shows a cloud cover starting in the south at the Mediterranean Sea, where a V-shaped storm was active due to EUMETSAT satellite analysis. The measurements reveal a mixing ration of ∼290ppmv which is not shown in the figure and a very well agreement of cloud 'A'.

According to ECMWF icy particles were formed at t = -0.5 days evident by the increased cloud ice water content (IWC) in Figure 4.6. The subsequent steep decrease of 80% within 6 hours is fast in light of the elevated RHi values in that period of time. The ECMWF model does not indicate any clouds above Lindenberg at t = 0 in contrast to the observations (Figure 4.2). IWC estimates made based on COBALD BSR (vertical bars) show a large discrepancy to ECMWF.

Regarding the geographical aspect, COSMO-7 trajectories show, within its standard boundaries set by MeteoSwiss (boundary in the south: 37°N), a very similar picture to the ECMWF trajectories displayed in Figure 4.5 and is therefore not shown here. Figure 4.7 show ECMWF and COSMO-7 trajectories in pressure vs. latitude plots. The two vertical solid lines in both panels represent the extension of the Alps. COSMO-7 trajectories are

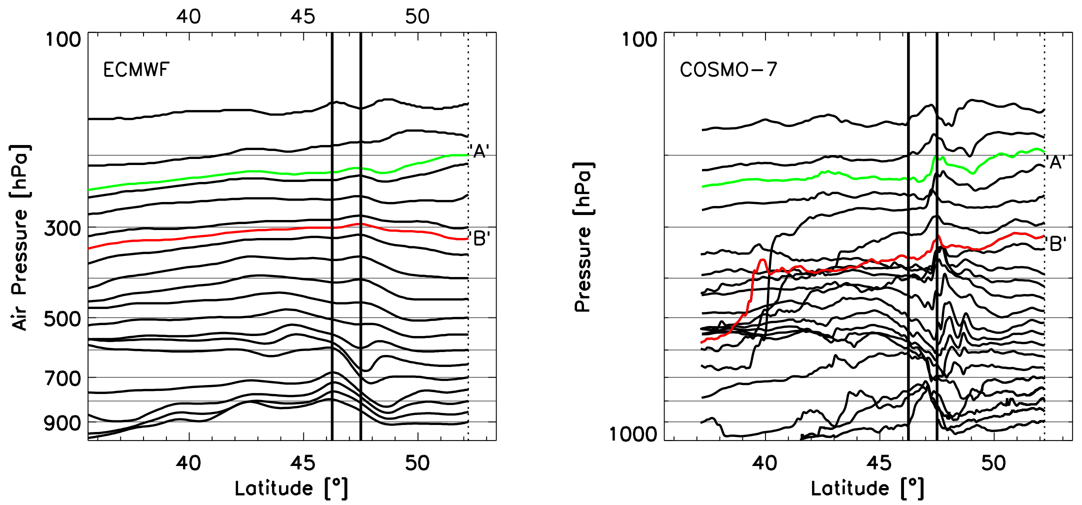

Figure 4.7: *LAGRANTO calculated trajectories displayed as pressure vs. latitude based on ECMWF (left panel) and COSMO-7 (right panel) operational data. Cloud 'A' and 'B' are in green and red, respectively. The vertical solid lines represent the extension of the Alps.*

much more detailed and show small scale fluctuations. Furthermore, COSMO-7 reflects the disturbance triggered by the Alps more detailed.

Figure 4.8 shows 4 panels with COSMO-7 trajectory results (solid lines) compared to measured values at time = 0 displayed as arrows. IWC estimations (lower left panel) are displayed with a double-head arrow for the upper cloud 'A' and an arrow pointing to the estimated value band (0.0015 - 0.003 g/kg). ECMWF trajectories are shown as dotted lines. The characteristics of RHi, temperature and IWC of the two models agree with the upper cloud (green) but diverge for the lower cloud (red). The above described V-shaped storm seems to influence the mixing ratio of COSMO-7 more profoundly.

In conclusion, COSMO-7 for time 01 UTC is the only operational analysis product that shows two layers with respect to RHi and IWC. Ice particles are located too low for the upper cloud 'A' but with the observed lower cloud. IWC values are underestimated for both clouds. COSMO-7 based trajectories are much more detailed than ECMWF. Furthermore, the characteristics of the devolution for LAGRANTO results based on 01 UTC COSMO-7 analysis data and ECMWF trajectories are for cloud 'A' similar but vary for cloud 'B' disregarding the different time resolutions. Due to mentioned reasons above COSMO-7 trajectories at time 01 UTC are used as input data for the microphysical column model in the upcoming section.

4.5.1 Analysis with the microphysical column model

Figure 4.9 shows the results for COSMO-7 (black) and the microphysical column model (colours) for one box in an altitude of 8500 m. On the one hand it shows the mixing ratio (total and gas phase), temperature, RHi and IWC devolution from COSMO-7. On the other hand the figure shows the simulated results by the column model for aerosol BSR, mixing ratio (total and gas phase), ice number density, RHi and IWC.

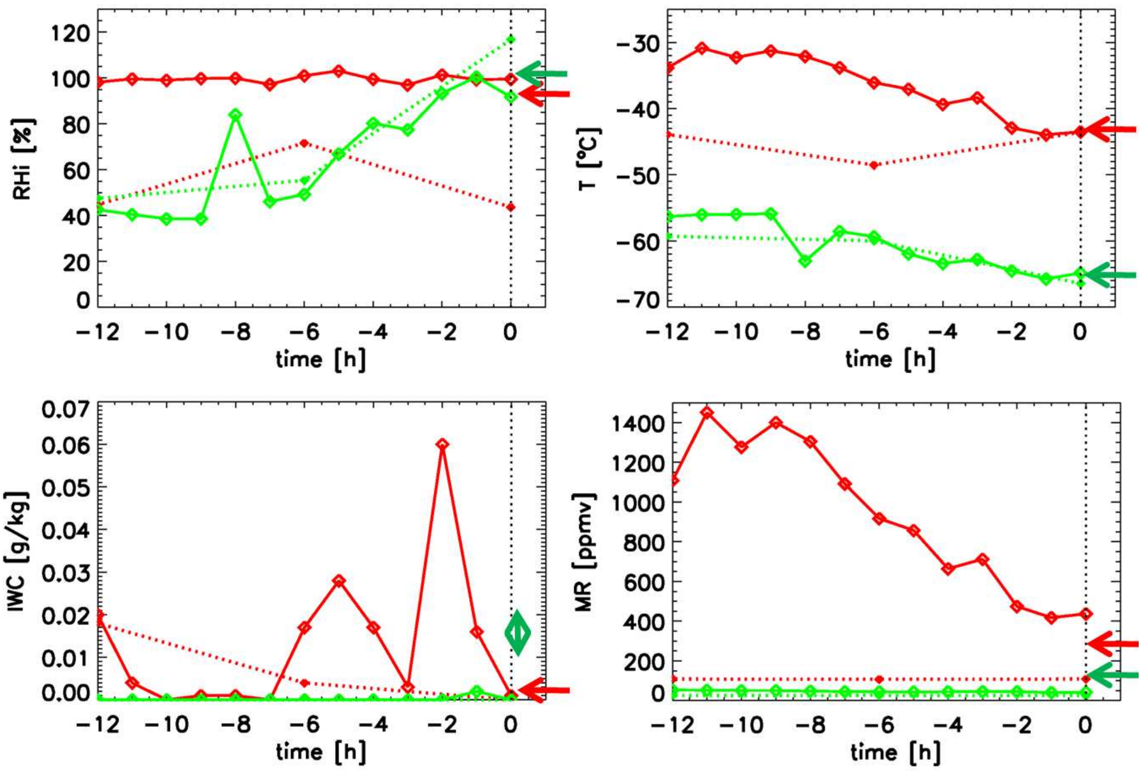

Figure 4.8: *COSMO-7 12 hours back trajectories (solid lines) refer to the colour code in Figure 4.5. Only in-cloud trajectories of the upper cloud 'A' (green) and the lower cloud 'B' (red) are presented. The x-axis show the calculated hours starting from t=0 which is above Lindenberg. Measurements at time=0 are indicated with arrows and IWC estimations (see Section 4.2.1) the lower cloud 'A' is shown with a vertical green double-head arrow and for cloud 'B' a horizontal red arrow points to the estimated value band(0.0015 - 0.003 g/kg). ECMWF trajectories are shown with dotted lines.*

COSMO-7 trajectories of water and temperature indicate that seven hours before the observation, ice water content was negligible and that the relevant nucleation occurred only later. Consequently the column model was initialized with the gas water content at that time (black horizontal bar in panel a). Subsequently, the column model simulations follows the temperature devolution of the COSMO-7 temperature trajectory. If RHi of the model reaches ∼150% homogeneous nucleation is initiated visible at -5.25 h. The consequences of the homogeneous nucleation is visible in all the panels. Once ice particles are formed (blue line in panel b) aerosol BSR increases (panel a) and the gas phase RHi decreases (panel c) and relaxes to RHi = 100 %. As soon as ice particles are fomed they start to sediment. Panel (d) shows IWC and indicates the amount of ice present. In Figure 4.9 starting from -6.5 h going forward in time mixing ratio (panel a), ice number densities (panel b) and IWC (panel d) reveal an increase due to ice particles sedimenting from the upper box. Furthermore, the decrease of the ice number density (panel b) starting from -5.25 h going forward in time indicates sedimentation into a lower box of the column. COSMO-7 and the box model show severe differences for gas phase RHi and occurrence of IWC in the provided example.

Results from the microphysical column model are summarised in Figure 4.10 compared to the measurements. The simulated upper cloud 'A' of the column model is at lower altitudes than observed by COBALD. This might be explained by insufficient time res-

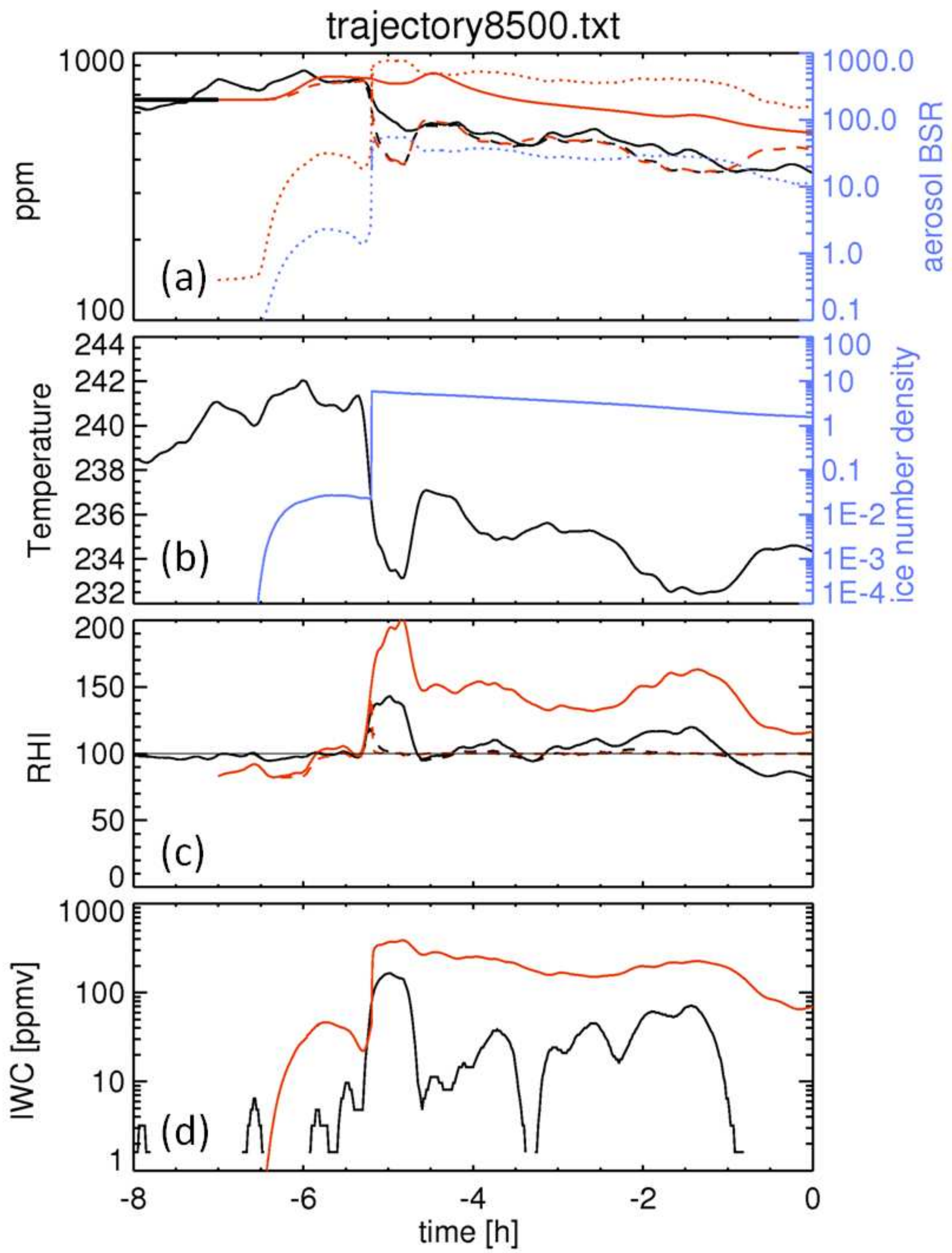

Figure 4.9: *Microphysical column model results based on COSMO-7 (01 UTC) hourly analysis fields and COSMO-7 trajectory results for an altitude of 8500m. All black lines are LAGRANTO results based on COSMO-7 data and all coloured lines are results by the microphysical column model simulation. The initial amount of water for the box model calculations is taken from COSMO-7 at -7 h visualised in panel (a) with a black bar. This panel shows the COSMO-7 (black) total water (solid line) and gas phase (dashed line) water mixing ratio. The two dotted lines represent BSR_{455} and BSR_{870}. Panel (b) shows the temperature (black) devolution by COSMO-7 and in blue the simulated ice number densities. In panel (c) RHi of the gas phase without a nucleation event (solid) and the gas phase with a nucleation event (dashed) is shown. Finally, in panel (d) IWC of COSMO-7 trajectories and the microphysical model are illustrated.*

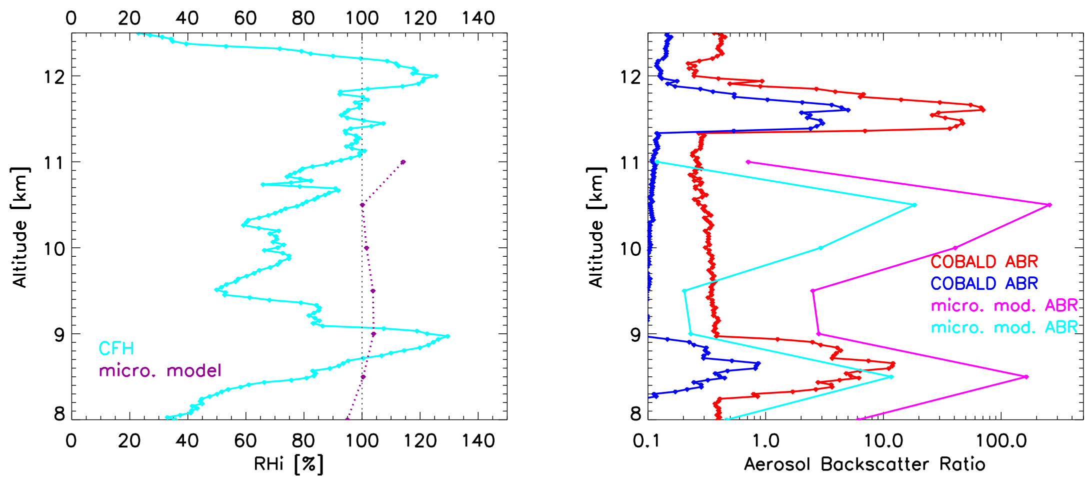

Figure 4.10: *In the left panel RHi of CFH (cyan) and the microphysical model (purple) is shown. The right panel shows the blue and red aerosol BSR of the measurements (blue and red) and the microphysical column model (cyan and magenta).*

olution of the underlying COSMO temperature and pressure data. The altitude of the simulated cloud 'B' fits with the observation.

4.6 Summary and Conclusion

This work has analysed one profile with two cirrus clouds measured by balloon-borne sondes above Lindenberg, Germany on 6 November 2008. A newly developed backscatter sonde termed COBALD and a state-of-the-art frostpoint hygrometer named CFH were used as part of the "Lindenberg Upper-Air Methods Intercomparison" (LUAMI) campaign. The COBALD-CFH tandem is shown to be an excellent combination to determine the partitioning of atmospheric water between the gas phase and the condensed ice phase in and around cirrus clouds, and thus to detect in-cloud and out-of-cloud supersaturation with respect to ice. In-cloud measurements showed that RHi from 47 % to 130 % occured. Without COBALD there would be no clear evidence for the boundaries of the clouds. Therefore, COBALD prooves to be a valuable instrument to fill this gap and to improve the quality of water vapour measurements inside and outside of cirrus clouds.

Operational analyses of ECMWF (1°x1° spatial resolution, 6-hourly stored fields) fail to represent cloud properties properly, such as ice water contents or relative humidities, whereas COSMO-7 fields (6.6 x 6.6 km, hourly) show better agreement with the observations, though the profile of the ice water content is not captured accurately. The main difference between the ECMWF and the COSMO data are the resolution of small-scale vertical winds, which allows the mesoscale model to better represent cirrus nucleation and growth processes, and better mesoscale representation of mixing processes resulting in a more accurate representation of relative humidity. Comprehensive microphysical cloud model calculations along LAGRANTO trajectories based on COSMO-7 wind and temperature fields allow humidity, ice particle size, number density and backscatter ratios to be determined, which are in good agreement with the measured cirrus clouds. The higher backscatter values obtained by the microphysical model compared to the measurements

	ECMWF	COSMO-7	Microphysical model
T	✔	✔	✔
RHi	—	✔	✔
IWC	—	(✔)	✔
Vertical location	—	(✔)	(✔)

Table 4.1: *Summary of model ability to reproduce the observations. A tick mark indicates "good reproduction", a tick mark in brackets "reproduction with limitations" and a horizontal line "no reproduction".*

for both clouds are thought to be due to the chosen sedimentation rates which imposed by too large ice particles.

The summary of the results are illustrated in Table 4.1. A tick mark in brackets indicates "with limitations".

Acknowledgments

M. Brabec is funded by the Swiss National Science Foundation with the project number 200021-1179879. Thanks to the organisers of the "Lindenberg Upper-Air Methods Intercomparison" campaign (LUAMI) especially Franz Immler, Holger Vömel and the whole crew in Lindenberg, who made the campaign work. We also acknowledge ETH, Zurich.

Chapter 5

Balloon-sonde measurements of in-cloud and clear sky humidities at cirrus levels from polar to tropical latitudes

This chapter is a paper draft.

M. Brabec*, F. G. Wienhold*, B. Luo*, F. Immler+, H. Vömel+, E. Hall[o], H. Rieder*, T. Peter*

* Institute for Atmospheric and Climate Science (IAC), ETH Zurich, Switzerland
+ Meteorological Observatory, Lindenberg, Germany
[o] National Oceanic and Atmospheric Administration (NOAA), USA

The layout of the article as well as the section and figure numbering have been adapted to match with the thesis structure.

Abstract

Previous studies of in-cloud and clear sky measurements in the upper troposphere reveal high supersaturations occasionally exceeding water saturation. This raised the question whether there is a lack of understanding of ice cloud formation processes.

This study investigates balloon-borne measurements of S_{ice} comprising all sky, in-cloud and clear sky conditions. 43 cirrus clouds detected on 27 balloon soundings in high-latitude, mid-latitude, tropics, monsoon region and southern hemisphere in the temperature range 187 - 250 K. Frequent super- and subsaturations are observed inside cirrus clouds but no measurements reveal supersaturations above water saturation.

In-cloud and clear sky observations are statistically analysed and compared to other cirrus cloud studies (such as Ovarlez et al. (2002), Jensen et al. (2005), Gierens et al. (1999), Spichtinger et al. (2002) and Krämer et al. (2009)) and cirrus model results. The study shows that cirrus clouds reveal significant differences among the geographical regions concerning S_{ice}. The increase of the median S_{ice} from high-latitudes to low latitudes could be caused by different formation processes in the corresponding geographical regions and indicating the need for further studies. It raises the question if future cirrus studies need to be analysed differentiating geographical regions.

Moreover, it is shown that clear sky observations follow an exponential distribution regarding S_{ice} which means that the probability of measuring a certain amount of ice supersaturation in the analysed troposphere decreases exponentially with increased ice supersaturation. This is in agreement with observations done by Gierens et al. (1999), Spichtinger et al. (2002) and Ovarlez et al. (2002).

5.1 Introduction

Lifting an air parcel increases its relative humidity by its associated temperature decrease. If an air parcel is moist enough, humidity exceeds its equilibrium value over ice, leading to a supersaturated and therefore metastable phase. At sufficiently high supersaturation ice crystals form and the gas phase relaxes to equilibrium (Peter et al., 2006). These cirrus cloud ice crystals deplete gas phase water in the upper troposphere as a function of their number and size (Korolev and Mazin, 2003). The diffusional growth eventually leads to sedimentation of ice crystals and therefore a redistribution of water in the upper troposphere **??**.

Many air borne and remote sensing measurements have been performed to study the distribution of saturation with respect to ice (S_{ice}) in the upper troposphere. These studies reveal high supersaturations i.e. of 60 % (aircraft measurement, <205 K environment, Gao et al. (2004)) and up to 130 % in aircraft measurement at 187 K (Jensen et al., 2005). Some measurements even exceed the liquid water saturation level (Ovarlez et al., 2002) which challenges our current microphysical understanding. A summary table on these supersaturation observations is provided in Krämer et al. (2009).

Here, we present the result of 26 balloon soundings from eight different locations. The data show 43 in-cloud measurements within 7 different campaigns covering a temperature range of 187 - 250 K. The locations are grouped in high latitudes (Sodankylä [Findland], Ny-Alesund [Norway]), mid latitudes (Zürich [Switzerland], Payerne [Switzerland], Lindenberg [Germany]), the tropics (Biak [Indonesia]), monsoon region (Lhasa [China]) and the southern hemisphere (Lauder [New Zealand]). Based on this data set, we examine in-cloud and clear sky supersaturation and compare it with previous studies (such as Ovarlez et al. (2002), Jensen et al. (2005), Gierens et al. (1999), Spichtinger et al. (2002) and Krämer et al. (2009)). One of the main aims of this work is to analyse if S_{ice} is significantly different among the individual geographical regions. The measurements are further compared to microphysical-model results to investigate whether microphysical cloud models use an appropriate accommodation coefficient.

5.2 Instrumentation and Method

The measurements use a balloon-borne backscatter sonde and a high quality hygrometer on the same payload. Section 5.2.1 describes the approach to determine or define cirrus clouds with these instruments. The second type of sondes are frostpoint hygrometers to measure water vapour. In this study 3 different hygrometers were used: SnowWhite (SW), the NOAA Frostpoint Hygrometer (NOAA-FPH) and the Cryogenic Frostpoint Hygrometer (CFH). All sondes are briefly introduced below.

The Lagrangian microphysical model which was applied to be compared to observations is described in Section 5.2.3. The model was used to investigate one special data set in a case study for Lindenberg 5/6 November 2008.

The data are binned in 20 m intervals equivalent to about 4 values at a rise rate of 5 m/s and a 1 sec resolution. Therefore small features in the data may be considered.

5.2.1 COBALD

COBALD is a balloon-borne backscatter sonde developed at ETH Zurich to be flown on operational weather balloons using the telemetry of a pTU sonde. COBALD uses similar principles as the Wyoming Backscatter sonde by Rosen and Kjome (1991) which has been used extensively in field studies (such as Larson et al. (1994), Larson et al. (1995), Rosen et al. (1997), Beyerle et al. (2001)). The backscatter sonde COBALD is driven by two high power (250 mW) LEDs at wavelengths centered at 455 nm (blue) and 870 nm (infrared) illuminating the direct environment. The backscattered light caused by air molecules, aerosols or cloud droplets/ice particles is collected by a single silicon detector.

The backscatter data is treated with the procedure developed by Rosen and Kjome (1991): The raw backscatter signal provided by COBALD is normalized to the environmental molecular scattering derived from molecular number density using the payload temperature and pressure data. This product, termed backscatter ratio (BSR), is derived for both wavelengths (BSR_{455} and BSR_{870}) invoking a calibration procedure explained in chapter 3. The BSR has two contributions, the molecular Rayleigh part equaling unity by definition and the additional aerosol/particle backscatter (ABSR = BSR - 1). The way the BSR is used to determine in-cloud and clear sky observations is described in the following Section.

Cloud detection

To classify an air mass as in-cloud its BSR_{870} has to exceed a value of 3. This threshold is set to exclude (swollen) background aerosols which can reach a BSR_{870} of 1.5 as shown in chapter 6. This value provides a margin to safely exclude aerosol signals without substantially reducing the amount of cloud observations.

Depending on temperature the following cases are discriminated: (1) If the BSR_{870} signal is situated in a region below 235 K we classify it as a cirrus cloud. 235 K depicts the homogeneous freezing threshold as described in Koop et al. (2000), below which, according to common microphysical understanding, no liquid particles exist. (2) If part of the region of $BSR_{870} > 3$ is warmer than 235 K but colder than 273K the lower edge of the cloud is analyzed to distinguish between a cirrus and a mixed-phase cloud. In case BSR_{870} of the cloud's lower edge rises from a value of 3 to 30 in an altitude range less than 100 m and characterized by subsaturated conditions with respect to ice a cirrus cloud is assumed. This observation is attributed to large, sedimenting ice particles since liquid particles in subsaturation would evaporate within a few seconds in such conditions (Hienola et al., 2001) and reveal a "sharp lower edge". (3) For the sake of completeness, if T > 273K, a liquid cloud is measured and is not taken into account in this study.

5.2.2 Hygrometers

For measuring water vapor, frostpoint hygrometers were used. In a frostpoint hygrometer the temperature of a small mirror is measured, which is electronically controlled to maintain a thin and constant layer of frost coverage. Under these conditions the mirror temperature equals the frost-point temperature of the ambient air (Vömel et al., 1995). A brief specification of the three hygrometers used is given as follows. Depending on the campaign one of these hygrometers was used.

(1) The SnowWhite uses a single-stage thermoelectric Peltier device to cool the mirror. SnowWhite has been described by Fujiwara et al. (2003) and was designed and is produced by Meteolabor AG, Switzerland. As experienced during the AquaVIT campaign (Möhler et al., 2009) conducted inside the AIDA (Aerosols, Interactions and Dynamics in the Atmosphere) chamber in Karlsruhe, 8-26 October 2007, SnowWhite is only capable to measure water vapour mixing ratios larger than 10 ppm. This is taken into account in the selection of the profiles in section 5.2.1.

(2) NOAA-FPH and CFH are based on the former NOAA/CMDL frost point hygrometer with improved accuracy. They use cryogenic cooling. The measurement uncertainty of the frost point temperature is approximately 0.5°C which corresponds to $RH\mathrm{i} < 10\%$ in the upper troposphere (Vömel et al., 2007b). Further details are found in Vömel et al. (1995) and Vömel et al. (2007a), respectively.

5.2.3 Microphysical cloud model calculations

A microphysical cloud model has been used to simulate mid latitude cirrus clouds with input data from COSMO (COSMO, 2010) trajectory analysis data. The microphysical cloud model contains boxes on top of each other and simulates homogeneous nucleation along the measured trajectory. The nucleation properties embedded correspond to the theory of Koop et al. (2000). Once ice crystals have been formed supersaturation is depleted and ice crystal start to sediment depending on their size (see Section 2.1.4). Sedimentation of ice particles are not implemented in numerical weather prediction (NWP) models which makes the microphysical cloud model valuable. A description of the model is given in chapter 3 and can be found in Luo et al. (2003) or Hoyle et al. (2005).

5.3 Observations and discussion

The dataset examined covers a wide range of conditions at different latitudes (67° N to 45° S), altitudes (5 km to the tropopause) and temperatures (187-250 K). The observations include different kind of cirrus such as synoptically and orographically formed cirrus at high and mid-latitudes, while in the tropics measurements were conducted during the rainy season and therefore the cirrus are thought to be driven by convective outflows.

5.3.1 All sky versus in-cloud observations

Figure 5.1 shows all sky S_{ice} observations. The left panel depicts 246 sounding measurements using a CFH or NOAA/CMDL frost point hygrometer but without COBALD and in the right panel our 28 soundings with S_{ice} observations and COBALD on board. Our measurements include data from 5 km to the tropopause. In general, S_{ice} is distributed between subsaturated and supersaturated values close to the homogeneous freezing threshold as seen in Figure 5.1. 32.1% of all data exeeds S_{ice}. The symbols in Figure 5.1 right panel represent the three different hygrometers used which is CFH (+), FPH (□) and SW (△). All sky measurements in the tropics (left panel) reveal S_{ice} values above the homogeneous freezing threshold (black diagonal lines) of 50 nm and 5 μm and even above the liquid water saturation line (cyan line). In contrast, we observe no data above the liquid water saturation line (Figure 5.1 right panel). That supports thermodynamic basic understanding, above the liquid water line particles should immediately form directly from the gas phase. Previous measurements, no matter if in or out of clouds, did not reproduce this thermodynamic basic understanding (Jensen et al., 2005). Aerosols are present anywhere containing particles that grow with increasing RH until the water activity level for homogeneous freezing is reached - then they form ice. Very few of our measurements show the homogeneous freezing level. Some measurements exceed the 5 μm homogeneous freezing threshold (Koop et al., 2000) which is the lower diagonal line.

The data are not only sorted by regions but also classified as in-cloud or clear sky observations. Being able to distinguish humidity data from balloon soundings between in-cloud and clear sky is a novelty and not possible for previous measurements.

For all in-cloud measurements the median for S_{ice} is 1.02. The 25% and 75% quantile resides at $S_{ice} = 0.87$ and 1.11, respectively. The absolute minimum and maximum values are at $S_{ice} = 0.3$ and 1.49. Although an S_{ice} value of 0.3 is rather low and can be explained by particles falling into dry air below clouds. Our measurements do not support in-cloud observations done by Ovarlez et al. (2002) as mentioned above. Ovarlez et al. (2002) speculated that their high supersaturation measurements may suffer from artefacts due to ice crystal accumulating and evaporating in the instrument inlet which is supported by our observations. Equilibrium S_{ice} values are expected to be 1.0 in a dense cirrus cloud in the absence of strong wave activity or radiative heating and cooling

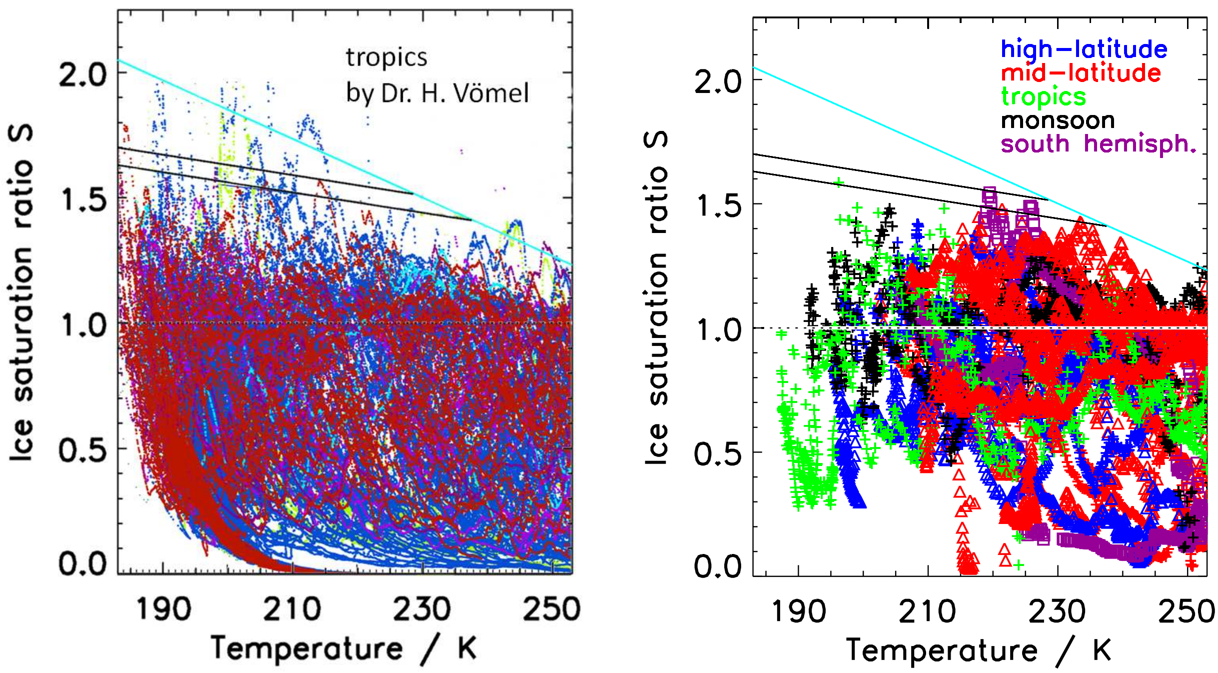

Figure 5.1: *All sky observations of S_{ice} vs. temperature. The cyan line depicts the water saturation curve whereas the diagonal black lines indicate the homogeneous freezing threshold for 50 nm (upper) and 5 μm. The dotted line shows S_{ice} = 1.0. Left panel shows 246 profile measurements in the tropics using CFH and NOAA/CMDL. The measurements were collected in Biak/ Indonesia (red), Kototabang/ Indonesia (magenta), Tarawa/ Kiribati (purple), Bandung/ Indonesia (cyan), Watukosek/ Indonesia (brown), Heredia/ Costa Rica (blue), Central Equatorial Pacific Experiment/ CEPEX (green) and Galapagos/ Ecuador (amber). The right panel shows 28 soundings in different geographical areas (as described in the introduction) from an altitude of 5 km to the tropopause. The different symbols represent the used hygrometer: (+) CFH, (□) FPH, (△) SW and the colours refer to the geographical region. The horizontal continuous line the median (S_{ice} = 0.86 for the entire dataset).*

(Khvorostyanov and Sassen, 1998).

Our measurements agree with the model hypothesis, and the data sampling appears to be representative. We observe diffusion limited growth and evaporation of particles that allows - in conjunction with modelling based on realistic temperature fluctuation - to test key assumptions of our microphysical understanding.

Comparison of S_{ice} between geographical regions

Figure 5.2 shows all in-cloud measurements subdivided into the geographical regions of high-latitude, mid-latitude, monsoon region, tropics and southern hemisphere. Additionally, a microphysical Lagrangian box model (see section 5.2.3), which simulates the evolution of cirrus clouds for a case study in Lindenberg (see Chapter 4), is shown in the lower right panel. The median appears to show a trend with the lowest values for high-

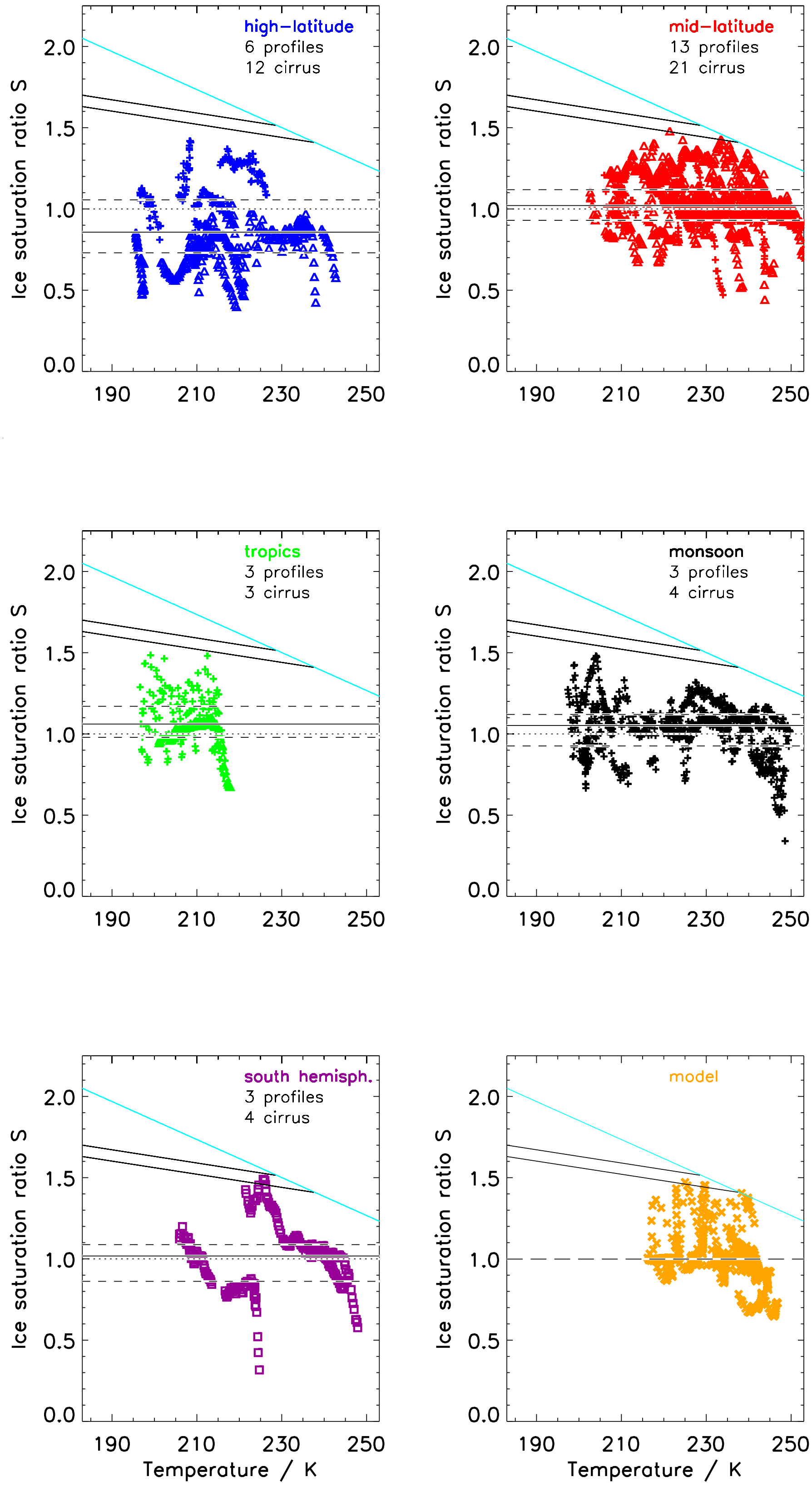

Figure 5.2: *In-cloud observations of S_{ice} vs. temperature. See description in caption to Figure 5.1 for lines and symbol explanations. Additionally, dashed lines depict 25% and 75% quantile, respectively. Moreover, in-cloud box model results are shown in the lower right panel.*

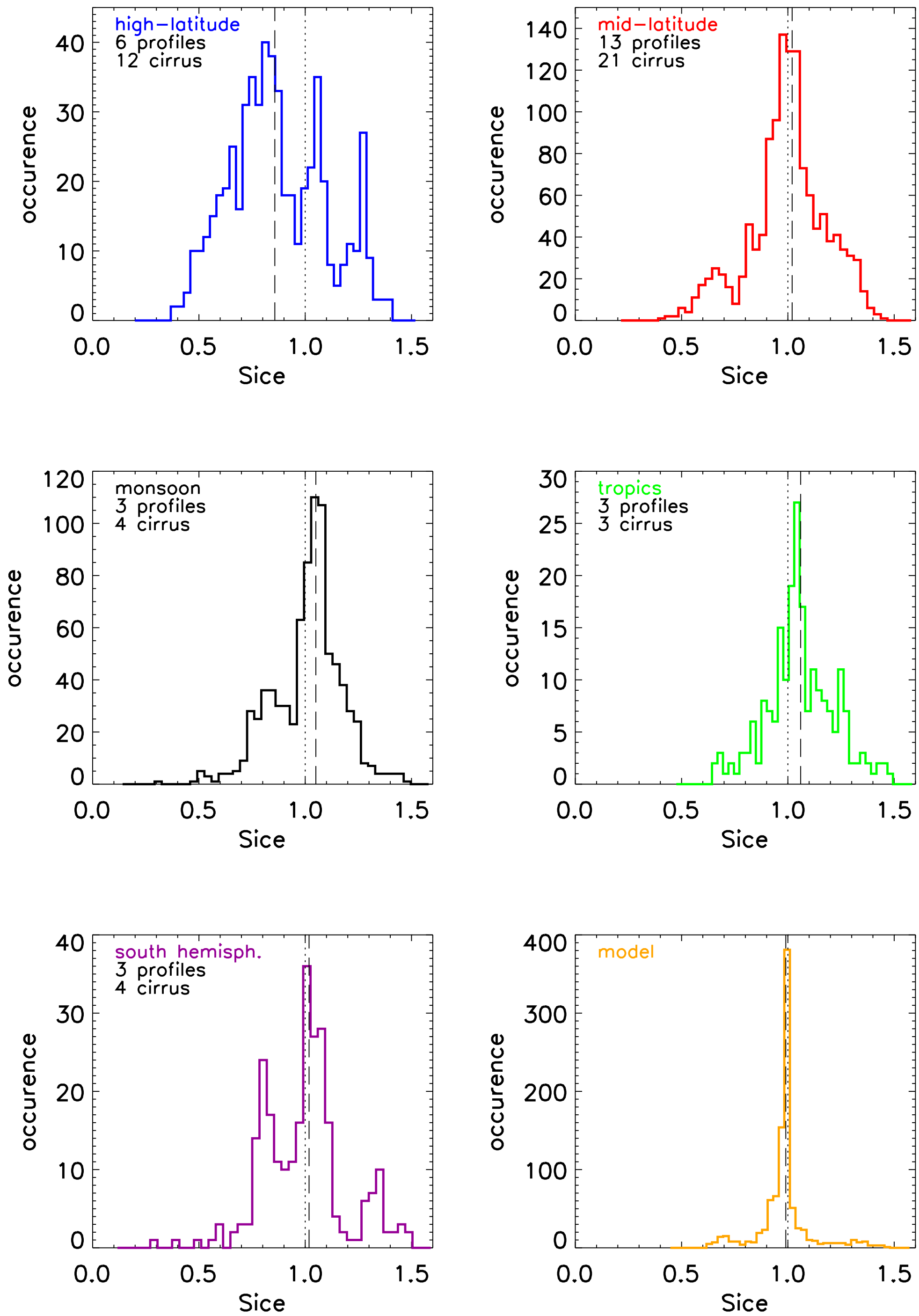

Figure 5.3: *In-cloud cirrus S_{ice} measurements displayed as occurrence. Dotted line shows S_{ice} = 1 and dashed line the median.*

latitudes (median = 0.86) and increasing towards the tropics where the highest (median = 1.06) values are found.

The distribution of in-cloud measurements is shown in Figure 5.3 and illustrates that the distribution of S_{ice} varies with geographical regions. It is important to keep in mind that the measurements contain clouds in different stages including evaporating cirrus clouds (low S_{ice} values) and a just formed clouds (high S_{ice} values) which broadens the

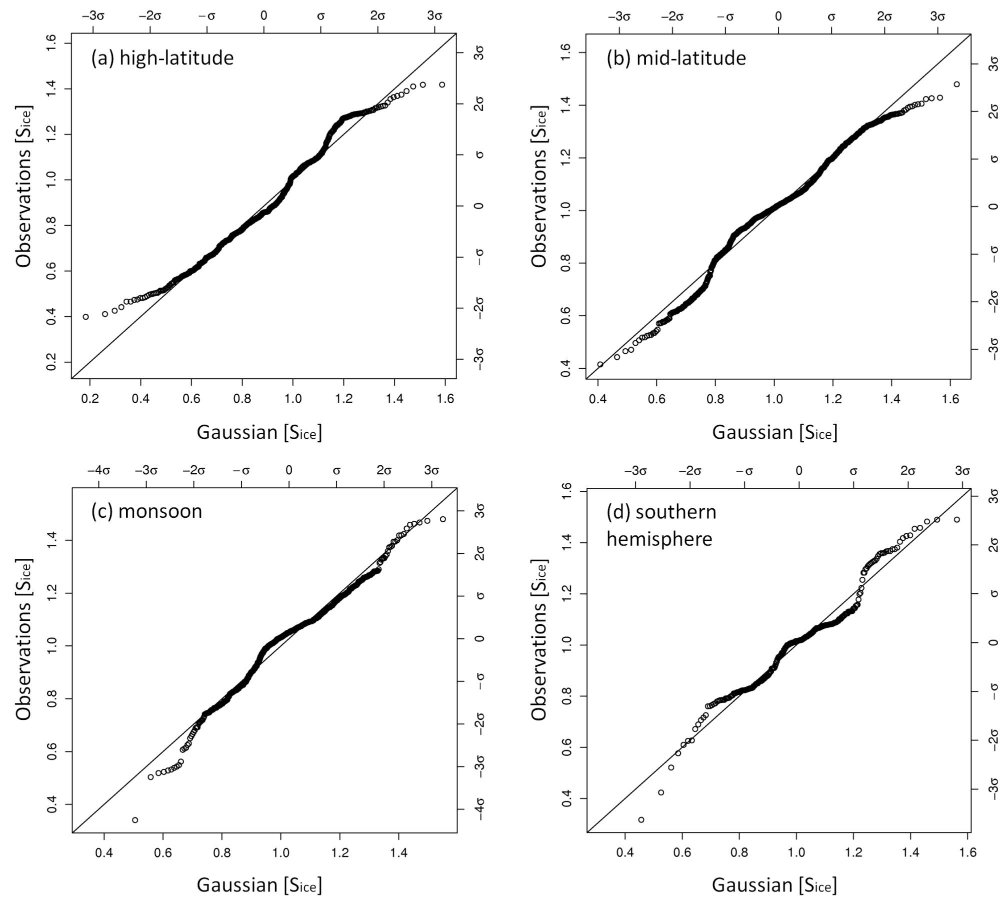

Figure 5.4: *Quantile-Quantile plots comparing (a) high-latitude observations, (b) mid-latitude observations, (c) monsoon and (d) south hemisphere with a Gaussian distribution (least-mean-square fitted to observations). The plots reveal a non-Gaussian distribution since a Gaussian distribution would lie closer to the diagonal line, but all observations show strong positive skewness.*

distribution. Other potential causes for broad distributions are (1) longer water vapour relaxation times as assumed or (2) strong perturbations (high cooling/heating rates).

In order to investigate if S_{ice} is significantly different for individual geographic regions a Student T-test is used under the assumption of a normally distributed S_{ice}. For data which significantly deviate from a Gaussian distribution, a Wilcoxon-Mann-Whitney rank sum test (commonly referred to as U-test) is applicable (Monahan, 2001). To test for Gaussianity a standard Shapiro-Wilk test is applied. The analysis shows that the test values (p-value, a statistical measure of evidence against the null hypothesis, following Royston (1982) and 1982b) for (a) high-latitude (2x10^{-7}), (b) mid-latitude (6x10^{-13}), (c) monsoon region (1.5x10^{-10}) and (d) southern hemisphere (1.3x10^{-5}), indicate strong deviations from a Gaussian distribution (Figure 5.4). However, for the fifth category (the tropics), the data can be adequately described by a Gaussian distribution with a p-value of 0.085 (”a p-value is a measure of how much evidence we have against the null hypothesis” (Essenwanger, 1976)) as seen in Figure 5.5.

Thus, for high-latitudes, mid-latitudes, monsoon regions and southern hemisphere deviating from the Gaussian distribution the U-test is applied in the further analysis. In all cases highly significant p-values (of the entire data sets as well as randomly sample

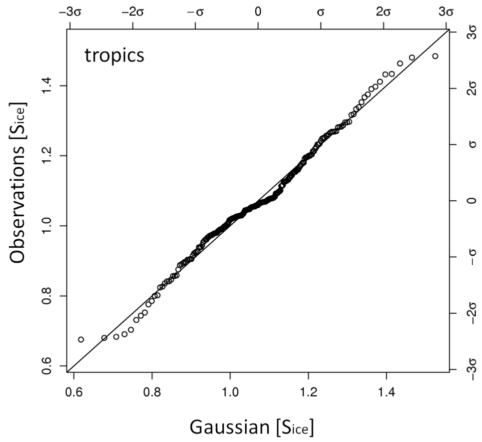

Figure 5.5: *Quantile-Quantile plot comparing the tropics with a Gaussian distribution (least-mean-square fitted to observations). The observations reveal a Gaussian distribution (p-value = 0.085).*

subsets (to address auto-correlation)) show that the individual observations are different and therefore the null hypothesis of equality of mean values needs to be rejected.

5.3.2 In-cloud intercomparison between measurements and the model result

Referring to the histograms in Figure 5.3 the model result shows by far the most narrow distribution compared to all our measurements. Statistical comparison for the observational data and the box model output shows, based on the Wilcoxon-Mann-Whitney test, a clear difference in the mean (p-value of $4 \mathrm{x} 10^{-5}$). Following this significant difference we have to be sure that temperature fluctuations are adequately represented in the box model runs. Up to now we used COSMO-7 analyses data. Once the temperature is approved it can be concluded that there is either a bias in the observations or an overestimation of the accommodation coefficient α, which is accountable for the depletion of the water vapour, in the microphysical cloud model. By decreasing α, the relaxation time is larger and therefore the spread would be broader and closer to the distribution of the observations.

However, such analysis is beyond the scope of the presented study and recommended for further in-depth analysis such as (1) Addressing experimental uncertainties by convolution of the model data histogram with a Gaussian of appropriate width (error estimate). (2) Overlay high frequency temperature fluctuations with the resulting total (COSMO-7 plus addition) PSD matching the reference spectrum. (3) Analyse if and what amount of accommodation coefficient tuning is needed.

Intercomparison with the in-cloud study of Krämer et al. (2009)

In this section in-cloud studies by Krämer et al. (2009) are briefly compared with our measurements. In Figure 5.6, the frequency distributions of RH_{ice} of our measurements are contrasted to the observations by Krämer et al. (2009). The measurements are binned into two temperature ranges above and below 205 K. In general, the two different measurements exhibit a good agreement. The peaks of the distributions for of T > 205K are

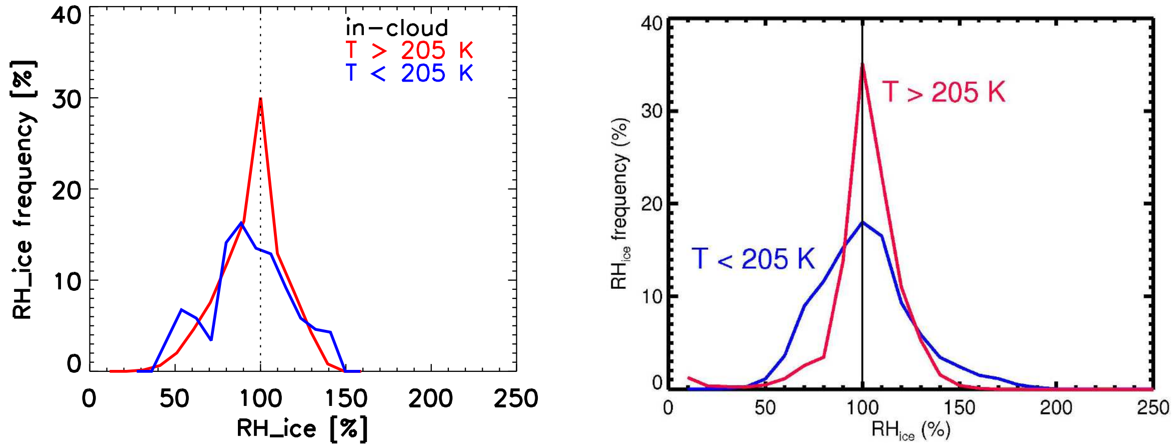

Figure 5.6: *In-cloud frequency of RH_{ice} for two temperature ranges: T < 205 K (blue) and T > 205 K (red). Comparison of our measurements (left panel) to Krämer et al. (2009) observations (right panel).*

at RH_{ice} = 100% for both data sets which also agrees with the observations during the mid-latitude experiment INCA (Ovarlez et al., 2002). Our measurements however show a significantly broader distribution, which could be caused by a measurement error or observations of longer water vapour relaxation times in the regions studied.

In the temperature range of T < 205K our measurements reveal a peak slightly below 100% RH_{ice}. Both data sets show a wider distribution in the colder regime. A part of this broader distribution can be caused by the precision of the water vapour measurement due to the low mixing ratios in those temperature ranges which can be of the order of 10ppm (Krämer et al., 2009). Another reason could be due to the fact that 80% of the measurements in the cold regime was performed by CFH which provides accurate water vapour measurements in cold regimes (Möhler et al., 2009), therefore we assume that this difference is caused by the longer water vapour relaxation times in cold cirrus.

5.3.3 Clear sky

The clear sky data set (Figure 5.7) shows measurements between 5 km and the tropopause excluding all in-cloud data. S_{ice} is randomly distributed between almost zero up to very few data points at the homogeneous threshold of 50 nm particles (Koop et al., 2000) with less data above saturation. 86.4 % of the clear sky measurements are below and 13.6 % above S_{ice}=1. Figure 5.8 illustrates with the means of density plots binned into intervals of S_{ice} = 0.05 for subsaturated (a) and supersaturated (b) regions. The supersaturated part is termed ice-supersaturated regions (ISSR) (Spichtinger, 2004). It shows that the ISSR data set can be adequately well described by an exponential distribution (maximum likelihood estimate rate parameter λ=0.085, standard error SE=0.003). The exponential distribution means that the probability of measuring a certain amount of ice supersaturation in the analysed troposphere decreases exponentially with the degree of ice supersaturation. This exponential dependency is also described by Gierens et al. (1999), Spichtinger et al. (2002) and Ovarlez et al. (2002).

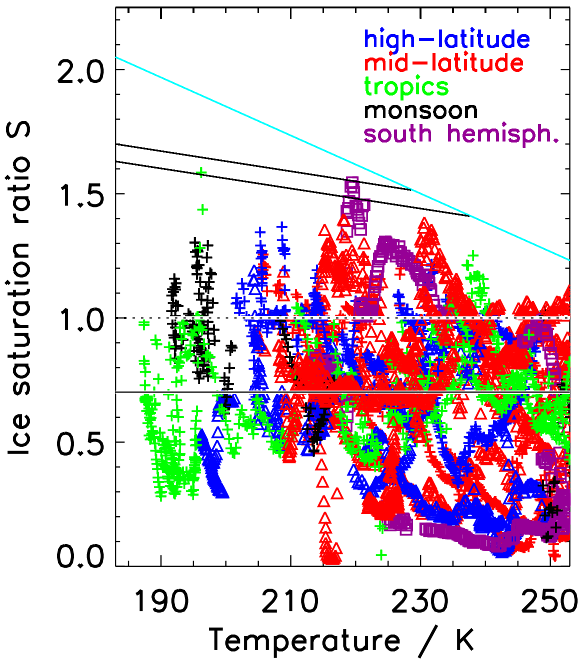

Figure 5.7: *Clear sky observations of S_{ice} vs. temperature. Data from an altitude of 5 km to the tropopause without clouds are illustrated. For line and symbols explanations see caption for Figure 5.1.*

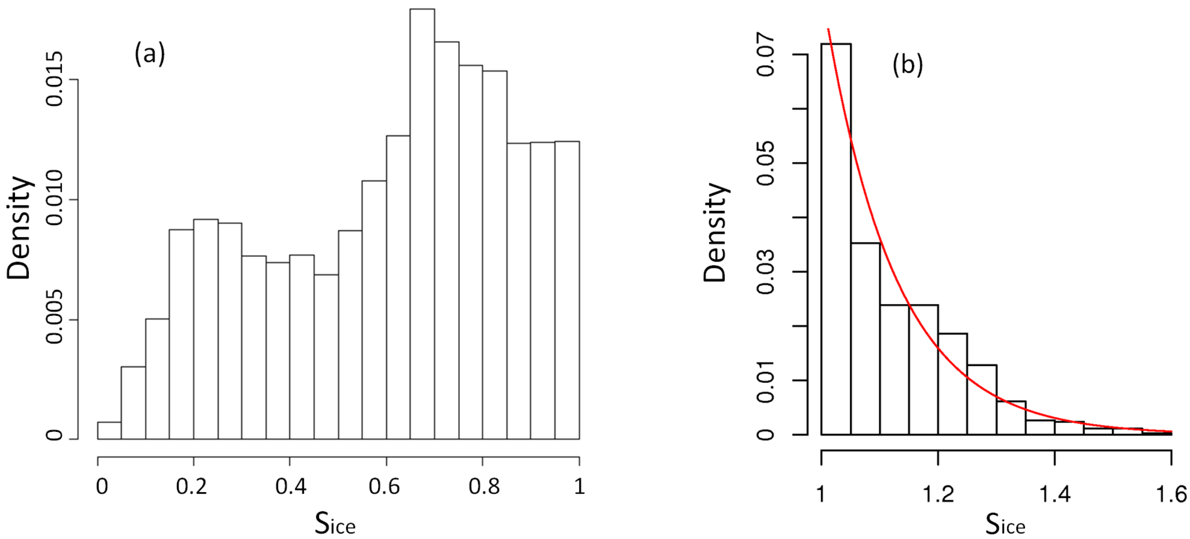

Figure 5.8: *Clear sky observations shown as a function of density. Panel (a) depicts measurements below and (b) above S_{ice}=1. The ISSR's follow an exponential distribution.*

5.4 Conclusion

In this study, we presented an in situ data set measured by balloon borne sondes, both in-cloud and clear sky observations of relative humidity as well as backscatter ratio to distinguish between in-cloud and clear sky. We demonstrated that the backscatter sonde COBALD successfully detects clouds and is therefore an indispensable instrument in future balloon borne observations of cirrus studies. Furthermore, we propose a way of distinguishing between cirrus clouds and mixed-phase clouds.

Our data does not reveal any measurements above the water saturation curve which questions measurements done by Jensen et al. (2005) (up to 230 %, aircraft measurement at 187 K).

The study shows that cirrus cloud distributions reveal significant differences between different geographical regions. Moreover, the increase of the median from high-latitudes to low latitudes could be caused by different formation processes in the corresponding geographical regions and needs further studies. It raises the question whether future cirrus studies should distinguish between regions.

It could be shown that the clear sky observations of supersaturation follow an exponential distribution which means that the probability of measuring a certain amount of ice supersaturation decreases exponentially with the degree of ice supersaturation. This is in agreement with observations done by Gierens et al. (1999), Spichtinger et al. (2002) and Ovarlez et al. (2002).

Acknowledgments

M. Brabec is funded by the Swiss National Science Foundation with the project number 200021-1179879. K. Rigel, H. Chisholm, A. Cirisan, I. Engel and MeteoSwiss are kindly acknowledged for launching balloons and the support. We also acknowledge ETH, Zurich.

Chapter 6

Australian dust aerosol measurements and simulation

This chapter is a paper draft.

M. Brabec, F. G. Wienhold, B. Luo, T. Peter

* Institute for Atmospheric and Climate Science (IAC), ETH Zurich, Switzerland

The layout of the article as well as the section and figure numbering have been adapted to match with the thesis structure.

Abstract

COBALD, a newly developed backscatter sonde was launched at Lauder, New Zealand to measure dust, transported from Australia across the Tasman Sea. With the support of the Lagrangian trajectory calculation tool LAGRANTO based on ECMWF wind fields, it is shown that the dust measured in Lauder originated from a dust storm in the Lake Eyre Basin. The dust plume was also observed by the MODIS instrument on Terra at the Australian south east coast. Microphysical model calculations based on water vapour data obtained on the same flight identify an additional BSR peak at around 350 hPa as swollen aerosols which indicates that COBALD is sufficiently sensitive to detect small signals arising from growth of aerosols caused by changes in relative humidity.

The dust was characterised in terms of particle size and number density based on Mie calculations. It revealed to have three possible estimated particle sizes which are 0.5 μm, 1.3 μm or 2.9 μm. Their corresponding number densities are 1 cm^{-3}, 0.2 cm^{-3} and 0.06 cm^{-3}.

Previous observations of dust which travelled from Asia to the San Nicolas Island, California, reported particle sizes of 1-2 μm (Tratt et al., 2001). Husar et al. (2001) describe Asian dust that reached other parts of western North America during April 1998 and had particle sizes of 2-3 μm. These results agree with our calculations.

6.1 Introduction

Dust aerosols play an important role in the climate system through direct interactions by affecting the radiation budget and indirect interactions by influencing cloud properties, biogeochemical cycles and also atmospheric chemistry (Tegen and Lacis (1996), Gildor and Follows (2002) and Ziemann (2010)). Additionally, dust aerosols affect air quality and human health (Griffin et al., 2001).

The residence time of the accumulation mode particles (See chapter 2 for description) are typically 3 to 10 days and therefore, have a significant effect on visibility, cloud formation and atmospheric chemistry. In the presence of large concentrations of dust, the coarse particle mode can also be optically active and hence be climatically important (Giannakaki et al., 2009).

On 22 September 2009, a severe dust storm originating from the Lake Eyre Basin, was sweeping through half of Australia's continent and brought dust particles to the Australian Capital Territory, the states of New South Wales and Queensland. The Lake Eyre Basin covers approximately 1.2 million square kilometers and is classified as an arid and semi-arid region (Pechey et al., 2007). Dust storms in Australia are not uncommon due to dry soil conditions, but are usually restricted to inland regions. However, during a widespread drought, dust storms occasionally reach coastal areas. When drought conditions reduce vegetation cover, the soil surface becomes more vulnerable to wind erosion. The 2009 dust storm carried away valuable soil from farmlands. The Australian ABC news (ABC, 2009) reported that at times up to 75,000 tonnes of dust per hour were blown across Sydney and dumped into the Pacific Ocean. Furthermore, they estimated that 5 million tonnes of valuable farmland topsoil was carried away.

Naturally occurring mineral dust is known to be the most abundant aerosol in the atmosphere with regard to its mass (Satheesh and Moorthy, 2004). Focusing on the Southern Hemisphere, Australia is considered to be the most dominant source (Tanaka and Chiba, 2006) with the Lake Eyre Basin as the largest contributor (Radhi et al., 2010), causing a range of environmental impacts including iron fertilization of surrounding oceans and possible climate feedbacks as described in Cassar et al. (2007).

Remnants of the mentioned dust storm were detected in New Zealand by the COBALD backscatter sonde. The dry air coming from the Lake Eyre Basin area was also identified by the water vapour measurements. The aim of this article is to illustrate the ability of the COBALD sensor and to simulate the dust transport by LAGRANTO, which allows for a comparison with the COBALD measurements.

6.2 Instrumentation and model tools

The following chapter describes all involved instruments and how the data is treated.

6.2.1 COBALD

The newly developed backscatter sonde COBALD is designed to be flown on operational weather balloons. It uses similar principles as the Wyoming backscatter sonde (Rosen and Kjome, 1991). COBALD operates with two high power (250 mW) LEDs at wavelengths centered at 455 nm (blue) and 870 nm (infrared). Due to air molecules, aerosols or cloud droplets/ice particles the light is backscattered and gets detected by a silicon detector. With certain assumptions on particle size distribution and morphology of the measured particles, information on particle sizes and number density are retrieved (Rosen and Kjome, 1991).

The backscatter data is treated according to the Rosen and Kjome (1991) procedure:

The backscatter signal needs to be normalised to the environmental molecular scattering derived from molecular number density using the payload temperature and pressure data. This outcome is named backscatter ratio (BSR). The BSR has two contributions, the molecular Rayleigh part, equaling unity by definition, and the additional aerosol/particle backscatter (ABSR = BSR - 1). COBALD provides BSR_{455} and BSR_{870} for the two different wavelengths. Its derivation invokes a calibration procedure explained in Section 3.2.3.

The colour index (CI) by convention has been defined as the ABSR in the infrared (870 nm) channel divided by the ABSR in the blue (455 nm) channel:

$$CI = \frac{ABSR_{870nm}}{ABSR_{455nm}} \tag{6.1}$$

CI is an indicator of particle size, given certain assumptions on the particle size distribution and on the refraction index. By definition very small particles with respect to the wavelength approach a colour index of 1 while large particles have an index of ∼14 (Rosen and Kjome, 1991). The latter value corresponds to the fourth power of the wavelength ratio. As explained by Rosen and Kjome (1991) it is possible for the CI to

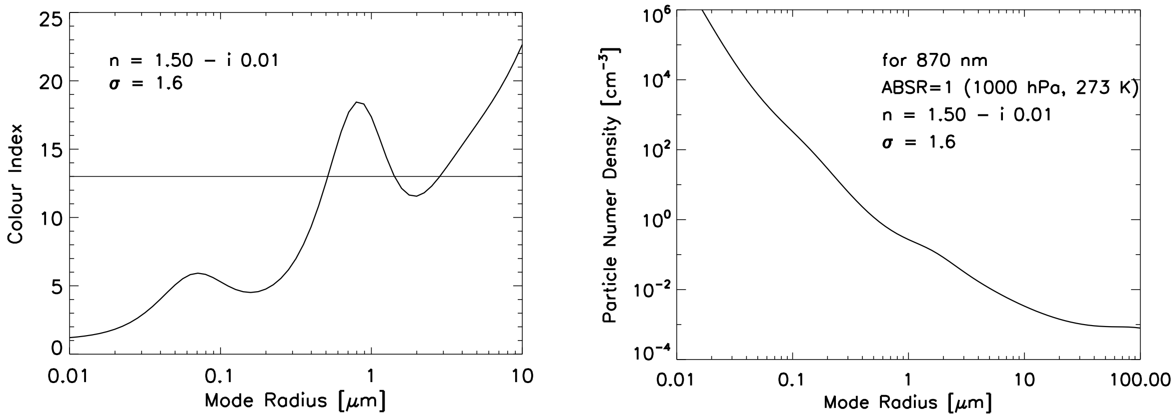

Figure 6.1: *Mie calculus modelled with a refractive index n = 1.50 - i 0.01 and a lognormal width of σ = 1.6. The left panel shows the colour index dependent on the mode radius. The horizontal solid line represents a CI of 13 and reflects the maximum value measured inside peak 'A'. The right panel shows particle densities versus mode radius for ABSR = 1.*

significantly exceed 14 before reaching the large particle geometric value, due to scattering functions oscillating around the asymptotic limit.

Figure 6.1 shows Mie calculations for a refractive index n = 1.50 - i 0.01 and a lognormal width of $\sigma = 1.6$. The left panel shows CI dependent on the mode radius. The solid horizontal line is for illustrations in Section 6.3.1. The right panel shows particle densities versus mode radius for the case ABSR = 1.

6.2.2 NOAA Frostpoint Hygrometer (NOAA/FPH)

NOAA/FPH is a chilled-mirror hygrometer using cryogenic cooling. The temperature of a small mirror, which is electronically controlled to maintain a small and constant layer of frost coverage, equals the frost-point temperature of the ambient air. Further details are given by Vömel et al. (1995). The measurement uncertainty is approximately 0.5°C which is a conservative estimate that covers most conditions and has been described by Vömel et al. (2007b).

Relative humidity with respect to ice is calculated according to its definition:

$$RHi_{FPH} = \frac{e(T_{FP})}{e(T)} \times 100 \tag{6.2}$$

where $e(T_{FP})$ is the water vapour partial pressure derived from the frost point temperature and e(T) the saturation vapour pressure at the ambient temperature T. The vapour pressure is calculated using the Murphy and Koop (2005) saturation vapour pressure formula.

6.2.3 LAGRANTO

The LAGRangian ANalysis TOol (LAGRANTO) allows the identification of air mass source regions and is described in detail by Wernli and Davies (1997). To drive the trajectory calculations, analysis input wind fields of the European Centre for Medium-Range Weather Forecast (ECMWF) are used for this study.

6.2.4 Microphysical box model

The microphysical box model, developed by Dr. B. Luo, simulates exchange of water between gas and condensed phase based on the diffusion equation (Hoyle et al., 2005). The model input consists of a number density for background aerosols, given by the equation:

$$n = n_0 \left(\frac{p}{p_0}\right) \left(\frac{T_0}{T}\right), \tag{6.3}$$

where n_0, p_0, and T_0 are the number density (330 H_2SO_4 cm^{-3}), pressure and temperature at a pressure level of 950 hPa, respectively. A log-normal size distribution is assumed with a value of $\sigma = 1.8$ were used. Furthermore, we assume that the aerosol particles are in equilibrium with the ambient relative humidity. The mode radius of the lognormal distribution at a pressure level of 950 hPa is assumed to be of 0.07 μm. Using the measured profiles of temperature and relative humidity, the composition of the aerosols, and therefore the size is calculated using the thermodynamic model given in Luo et al. (2003).

6.3 Observations and discussion

On 22 September 2009 a severe dust storm occurred in the south eastern part of Australia. On 25 September 2009 at 22.17 LT a payload comprising NOAA/FPH and COBALD was launched to explore remnants of dust in the atmosphere above Lauder (45°S, 169.7°E), New Zealand. Figure 6.2 shows the resulting profiles of RHi and BSR_{455} and BSR_{870} in conjunction with the colour index and the ambient temperature. Two distinct peaks in the BSR signal are visible at 700 hPa ('A', 3 km) discussed in the following part of this section and at 350 hPa ('B', 8 km) discussed subsequently.

6.3.1 Dust aerosol analysis

Peak 'A' measured at ~10.30 UTC has a BSR of 3 with very low RHi down to 57% (RHi = RH at 0°C) which indicates an arid air mass origin. Observation of a cloud can be excluded due to the low humidity values. The dry layer also indicates that biomass burning aerosols are unlikely since RH would be higher due to release of humidity by biomass burning.

The synoptic overview of Figure 6.3 shows that at the time of the dust storm event (map 1) a low pressure system was approaching the Lake Eyre Basin. The red arrow shows the location of Lauder, New Zealand and the black area depicts the Lake Eyre

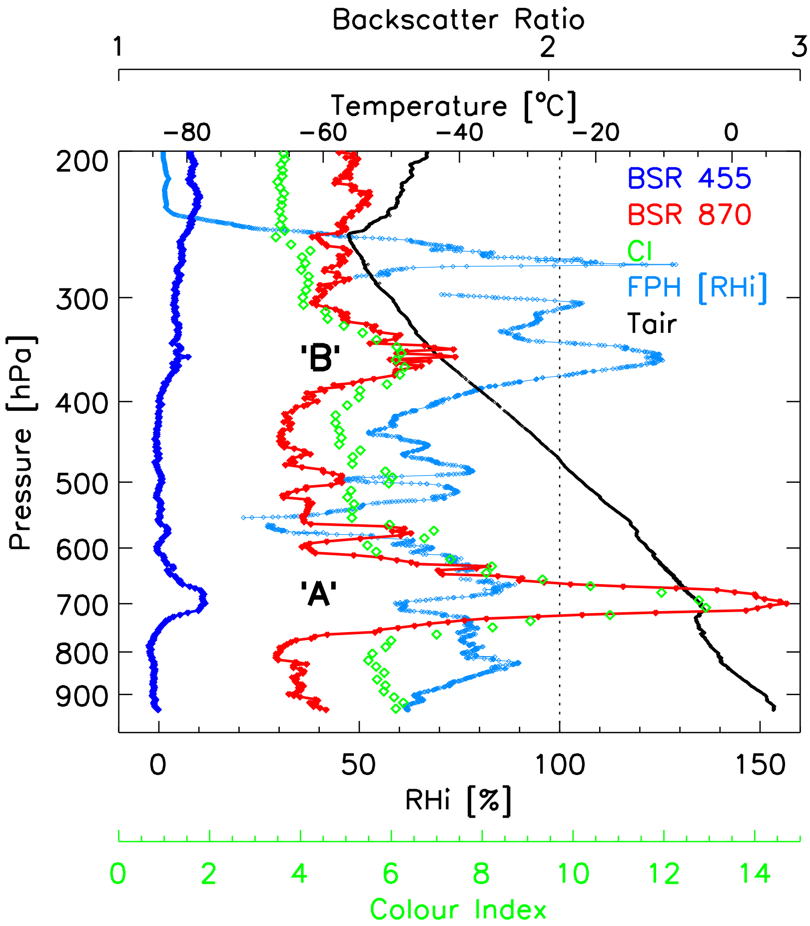

Figure 6.2: *Profiles of RHi, BSR and CI measured by NOAA/FPH and COBALD, together with radiosonde temperature. Two distinct peaks in the BSR signal are visible at 700 hPa (peak 'A') and 350 hPa (peak 'B').*

Basin. High wind velocities in the Lake Eyre Basin area in excess of 70 km/h were reported in the western part of New South Wales (Lays et al., 2009). These strong winds are associated with the cold front illustrated in Figure 6.3 moving from west to east and the low pressure trough passing the Lake Eyre Basin in the south. This low pressure system moved towards New Zealand and was responsible for transporting the dust of this event across the Tasman Sea.

Figure 6.4 shows a Moderate-Resolution Imaging Spectroradiometer (MODIS) image taken on 23 September 2009 at 13 UTC. MODIS is a scientific instrument on board of the satellite NASA Terra (NASA, 2011). The MODIS image shows the dust plume moving away from the mainland off the coast of New South Wales. The dust plume apparently tangles around the low pressure system and represents the location of the cold front marked in Figure 6.3 panel (4).

Figure 6.5 shows the classification of CALIPSO (Cloud-Aerosol Lidar and Infrared Pathfinder Satellite Observations) data for 25 September 2009 with the left end of the image recorded at 15.08 UTC and right at 15.22 UTC. The measurement satellite path is illustrated in Figure 6.6 by the diagonal black line. The classification (Vaughan et al., 2004) indicates aerosols (orange) dominantly in the left part of the image when the satellite passed over the air plume from between 28°S and 35°S. The altitude of the aerosol rises from the ground to around 3 km ($\sim$ 700 hPa) on the very left side of the picture (north) up to more than 5 km ($\sim$ 540 hPa) further south. Two days before the balloon observation, which is approximately at the time of the MODIS and CALIPSO images, the air parcels in Figure 6.6 were found at an altitude of 800 to 700 hPa, corresponding to the plume level.

To characterise dust aerosols measured in Lauder, New Zealand, COBALD data are analysed using Mie calculations (Laurent et al., 2010) which are performed using a refractive index of 1.50 - i 0.010 (Moulin et al., 1997) and a lognormal width of $\sigma = 1.6$. Figure 6.1 shows the result and allows to estimate the mode radius of the dust particles. Peak 'A' provides a CI value of 13 which is illustrated with a horizontal line in the left panel of Figure 6.1. The result is ambiguous and reveals possible mode radii of 0.5μm, 1.3μm and 2.9μm.

The right panel in Figure 6.1 shows the relation between particle number density and the mode radii for unity ABSR_{870}, for the same parameter set. Peak 'A' reveals a ABSR_{870} of 2, therefore the particle densities need to be multiplied by 2. The corresponding particle number densities for the mode radii as mentioned above are approximated to $\sim$1 cm^{-3} (for 0.5μm particles), 0.2 cm^{-3} (for 1.3μm mode radius particles) and 0.06 cm^{-3} (for 2.9μm mode radius particles).

6.3.2 Swollen aerosol analysis

Peak 'B' (referring to Figure 6.2) shows a BSR_{red} of $\sim$1.7 and RHi up to 125% as seen in Figure 6.2. The concentrations of H_2SO_4 particles as described in Section 6.2.4 is adjusted to the RHi profile. The result is shown in Figure 6.7. The dotted profile represents BSR_{870} measured by COBALD and the solid line depicts the simulation. In an altitude of 350 hPa where peak 'B' is located measurements agree strongly with the simulation. Therefore, peak 'B' is assumed to be swollen aerosols. Due to the low signal intensity it is not interpreted as a cirrus cloud.

The bad agreement in an altitude of between 900 and 800 hPa is assumed to be due to different air masses and therefore different properties of background aerosols.

6.4 Summary and conclusion

In this study, we presented measurements by COBALD, a newly developed backscatter sonde, and NOAA/FPH launched at Lauder, New Zealand to measure dust, transported from Australia across the Tasman Sea. The Lagrangian trajectory calculation tool LAGRANTO based on ECMWF wind fields confirm that the dust measured in Lauder originated from the Australian south east coast due to a dust storm also observed by the MODIS satellite. The dust was characterised in terms of particle size and number density based on Mie calculus. It revealed to have three possible estimated particle sizes which are 0.5 μm, 1.3 μm and 2.9 μm. Their corresponding number densities are 1 cm^{-3}, 0.2 cm^{-3} and 0.06 cm^{-3}. Previous measurements analysing dust carried long distances from Asia to the San Nicolas Island, California reported particle sizes of 1-2 μm (Tratt et al., 2001). Husar et al. (2001) describe Asian dust that reached other parts of western North America during April 1998 and had particle sizes of 2-3 μm. These results agree with our calculations.

Finally, microphysical model calculations based on water vapour data obtained by NOAA/FPH identify an additional BSR peak at around 350 hPa as swollen aerosols. This proves that COBALD is sufficiently sensitive to detect small signals arising from aerosol growth caused by changes in relative humidity.

In conclusion, COBALD successfully localised a dust plume. With support of Mie calculations and an accurate hygrometer it is possible to estimate dust particle sizes and particle number densities. Analyses revealed to have three possible estimated dust particle sizes which are 0.5 μm, 1.3 μm and 2.9 μm. Their corresponding number densities are 1 cm^{-3}, 0.2 cm^{-3} and 0.06 cm^{-3}. The estimated particle sizes (1.3 μm and 2.9 μm) agree with previous studies regarding long distance transport of dust particles.

In this work COBALD also successfully localised swollen aerosols with the help of a microphysical box model.

Acknowledgments

M. Brabec is funded by the Swiss National Science Foundation with the project number 200021-1179879. H. Chisholm and E. Hall are kindly acknowledged for helping to launch the balloon and the NOAA/FPH data supply, respectively. We also acknowledge ETH, Zurich.

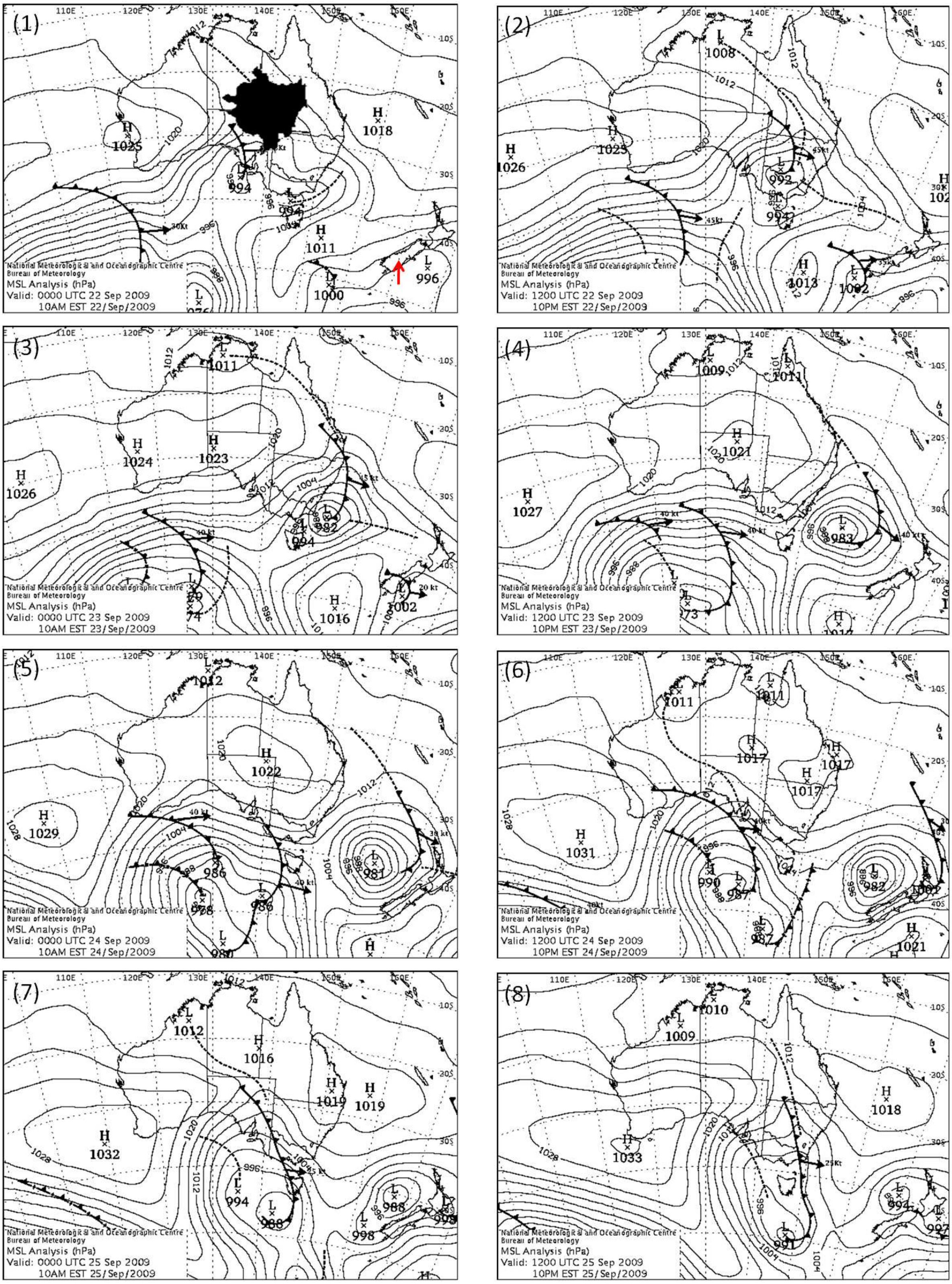

Figure 6.3: *Synoptic overview. Map 1 shows the synoptic situation at the dust storm event with the black area showing the Lake Eyre Basin and the red arrow the location of Lauder, New Zealand (adapted from original Australian Government (2009)). The time steps between maps is 12 hours and panel 8 shows the synoptic situation at approximately observation time. Figure courtesy of Australian Government (2009).*

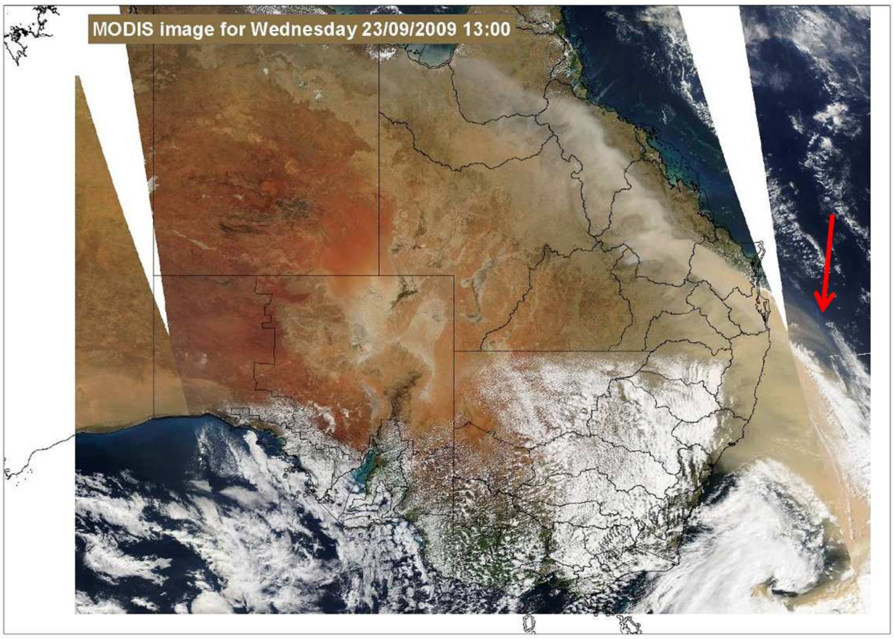

Figure 6.4: *MODIS image showing the dust plume off the New South Wales coast indicated by the red arrow. The image was taken on 23 September 2009. (Figure source: Lays et al. (2009))*

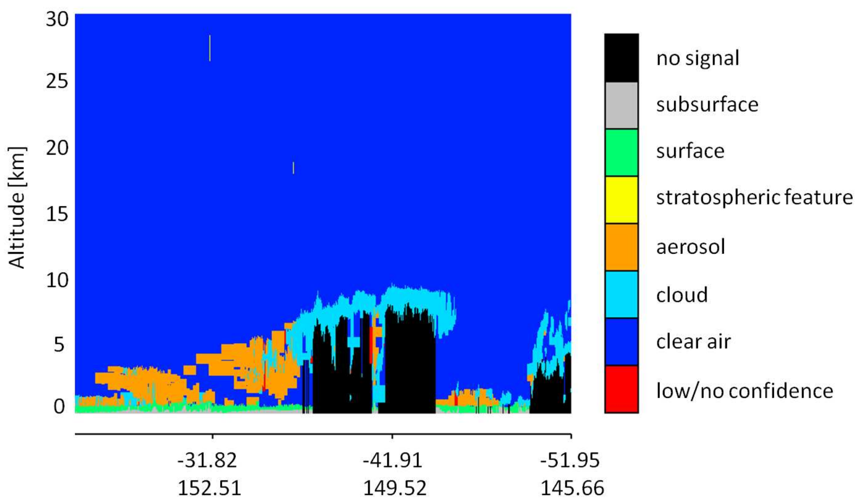

Figure 6.5: *Image of CALIPSO classification for 25 September 2009 at around 15.08 UTC (left side) to 15.22 UTC (right side). The x-axis shows latitude and longitude and the y-axis altitude. Adopted from CALIPSO (2010).*

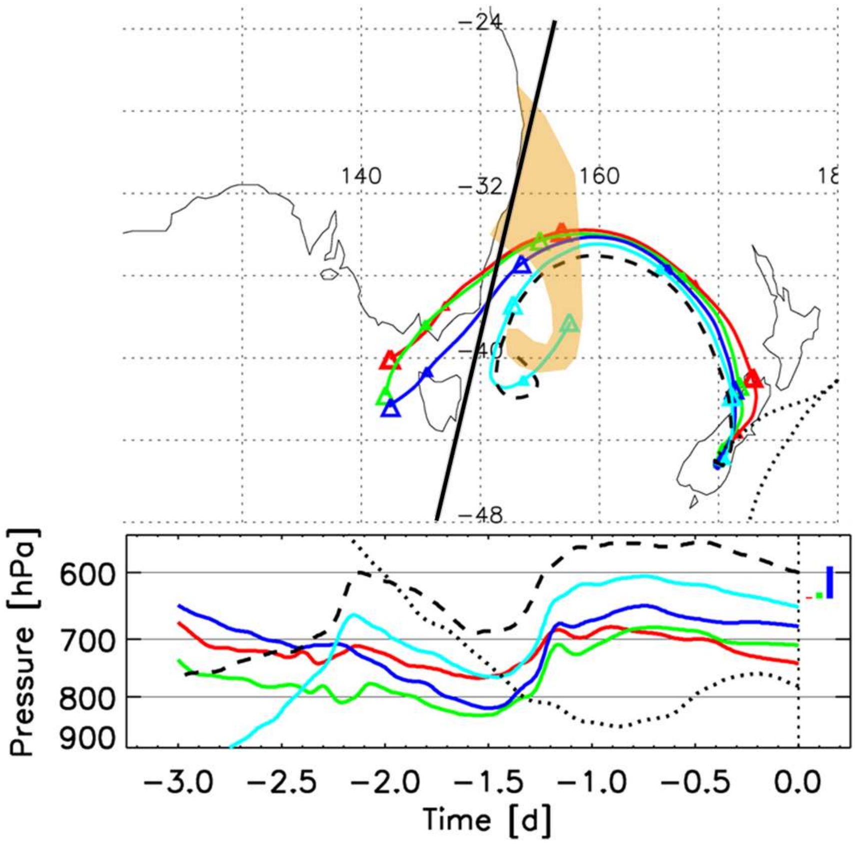

Figure 6.6: *LAGRANTO backward trajectories starting from Lauder, New Zealand. The coloured trajectories represent air parcels within peak 'A'. The connection from one large triangle to the other large triangle represents one day, the small triangles in between show the 12 hours in between. The light red area shows the dust plume taken from the MODIS satellite picture in figure 6.4. The black diagonal line represents the path of CALIPSO essential for Figure 6.5.*

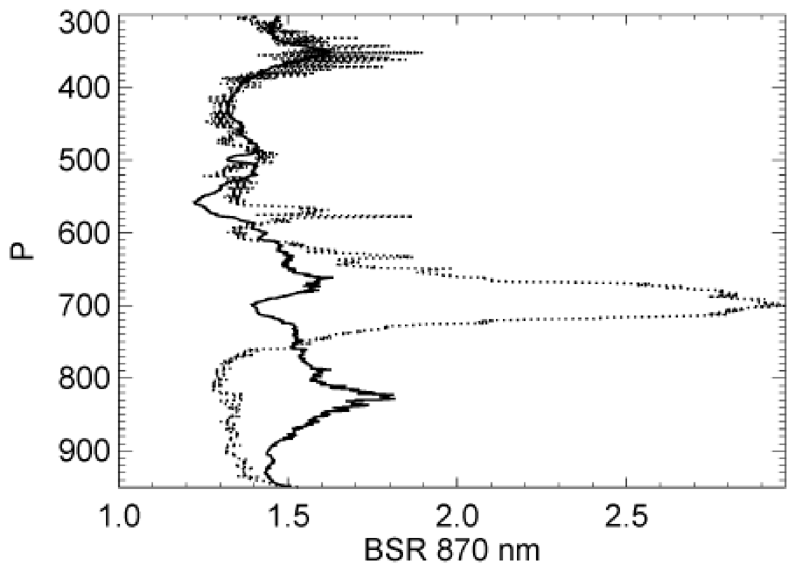

Figure 6.7: *Measured BSR_{870} by COBALD illustrated with the dotted line. Simulated BSR_{870} by the box model based on the relative humidity profile is illustrated with the solid line. Figure courtesy of Dr. B. Luo.*

Chapter 7

Final remarks

7.1 Review of the thesis

The balloon-borne backscatter sonde COBALD (Compact Optical Backscatter and AerosoL Detector) was successfully launched 111 times during a number of campaigns, together with various high quality hygrometers sondes. COBALD proved to be an essential tool for atmospheric applications.

This thesis shows that COBALD is able to quantitatively define boundaries of cirrus clouds, and accurately measure the particle backscatter ratio at two wavelengths (455 nm and 870 nm), from which the ice water content and to some approximation also the ice particle number density and a lower bound of the ice particle radius could be derived. It has been shown that COBALD adds to the RHi measurements and consequently to cirrus cloud studies. To correctly apply COBALDs measurements a calibration procedure was established and verified in parts.

A cirrus cloud case study at Lindenberg, Germany (52.21°N, 14.12°E) in November 2008 shows that the COBALD-CFH tandem is an excellent payload to determine the partitioning of atmospheric water between the gas phase and the condensed ice phase in and around cirrus clouds, and thus to detect in-cloud and out-of-cloud supersaturations with respect to ice. The case study investigates operational analysis data of ECMWF (1° x 1° spatial resolution, 6-hourly stored fields) and COSMO-7 fields (6.6 x 6.6 km, hourly). ECMWF fail to represent important cloud properties in this study, such as ice water contents or relative humidities, whereas COSMO-7 provides a much better agreement with the humidity measurements, although ice water content is not represented accurately. Microphysical cloud model calculations using LAGRANTO trajectories based on COSMO-7 wind and temperature fields allow a determination of humidity, ice particle size, number density and backscatter ratio, which are all in good agreement with the observed cirrus clouds.

A detailed analysis of all sky, in-cloud and clear sky conditions from 43 cirrus clouds observed in 27 balloon soundings in northern high latitudes, mid-latitude, the tropics, monsoon region and in the southern hemisphere mid latitudes is presented. Observations show frequent super- and subsaturations inside cirrus clouds but no measurements above water saturation, which contrasts with previous studies but agrees with common thermodynamic theories. An observed increase of the median S_{ice} from high-latitudes to low latitudes could be caused by different formation processes encountered in the corresponding geographical regions, e.g. in situ cloud formation versus outflow. It has been shown that clear sky observations follow an exponential frequency distribution regarding S_{ice}

that has also been shown by other cirrus studies. The exponential frequency distribution means that the probability of measuring a certain amount of ice supersaturation decreases exponentially with increasing ice supersaturation.

Finally, COBALD was applied to measure dust above Lauder, New Zealand transported from Australia across the Tasman Sea. With support of Mie calculus dust particles were characterised due to their mode radius and particle number density. The result showed particle sizes of 0.5 μm, 1.3 μm and 2.9 μm with their corresponding particle number densities of 1 cm^{-3}, 0.2 cm^{-3} and 0.06 cm^{-3}, respectively. Other studies of long distant transport of dust particles agree with the obtained values which supports assumptions made by Mie calculations based on COBALD's measurements.

7.2 Outlook

Based on the results presented in the previous three chapters, new questions arise. Some aspects are discussed in the following subsections.

7.2.1 For Chapter 4: A case study of particle backscatter and relative humidity measured across cirrus clouds and comparison with state-of-the-art cirrus modelling

The microphysical column model could not fully reproduce the observations. Therefore, experimental runs with higher time-resolved output fields (every 5 minutes) from COSMO-7 should be conducted. These could lead to improved vertical trajectory movements and cooling rates, and hence to further improve the modelled cloud properties.

In terms of improving the results of the microphysical column model it is planned to overlay high frequency temperature fluctuations over COSMO-7 data, which potentially lead to smaller ice crystals. As illustrated in Figure 7.1 by the means of the green arrow (1), smaller ice crystals sediment slower and might therefore agree better with the measured location of the upper cloud. However smaller ice crystals lead to a larger BSR signal. Applying heterogeneous nucleation instead of homogeneous nucleation would lead to fewer but larger ice crystals, which could decrease the BSR signals (green arrow 2) and therefore could lead to better agreement with the measurements.

7.2.2 For Chapter 5: Balloon-sonde measurements of in-cloud and clear sky humidities at cirrus levels from polar to tropical latitudes

RS92 data with a newly developed correction method, which were flown on the same payload as COBALD, are planned to increase the amount of measurements for an improved statistics. This will be done in coorperation with Dr. F. Immler.

The BSR$_{red}$ threshold to determine cirrus clouds in Section 5.2.1 was set to 3 which needs to be tested in a sensitivity study. It needs to be shown that changing the BSR threshold by for example 1 does not alter the over all results of the study.

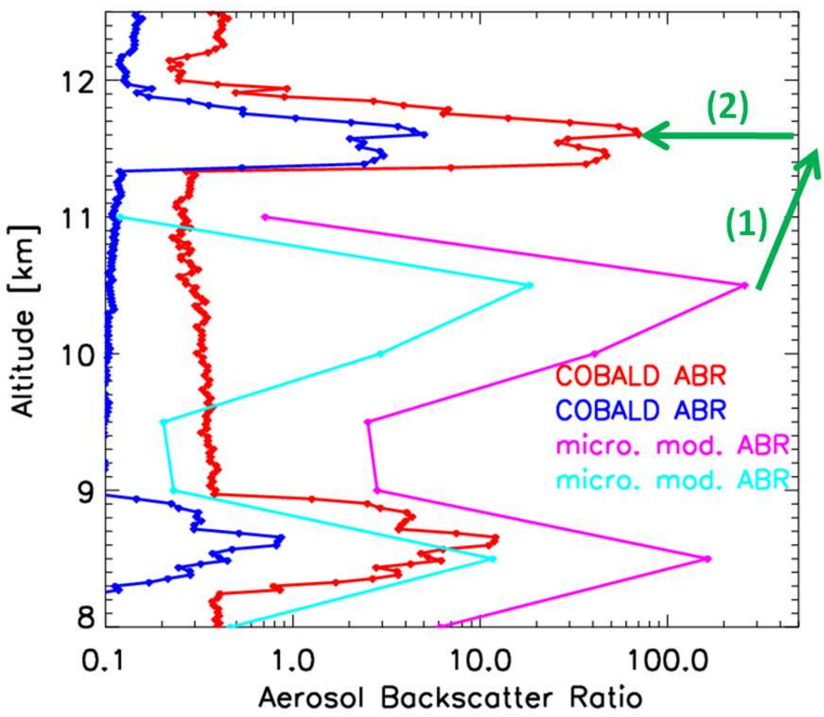

Figure 7.1: *Figure taken from Chapter 4. The figure illustrates BSRs of COBALD vs. microphysical column model results. Additionally, two green arrows illustrate improvements explained in the text.*

Statistical values such as median and quantiles are planned to be compared with measurements by Krämer et al. (2009) as soon as data by Martina Krämer are available.

Regarding the significant difference of model and measurements, further in-depth analysis is needed such as

(1) Addressing experimental uncertainties by convolution of the model data histogram with a Gaussian of appropriate width (error estimate).
(2) Overlay high frequency temperature fluctuations over COSMO-7 temperatures.
(3) Analyse if and what amount of accommodation coefficient tuning.

7.2.3 For Chapter 6: Australian dust aerosol measurements and simulation

Contrary to Laurent et al. (2010) who suggest to use Mie calculus for small dust particles, T-Matrix could be applied to compare results.

Furthermore, calculations with FLEXPART could be used. FLEXPART is a Lagrangian particle dispersion model that simulates the long-range and mesoscale transport, diffusion, dry and wet deposition and radioactive decay of tracers released from point, line, area or volume sources. It uses ECMWF numerical weather analysis fields (Stohl et al., 2005). With information on soils and the surface of the source region it would be possible to obtain quantitative Australian dust emissions.

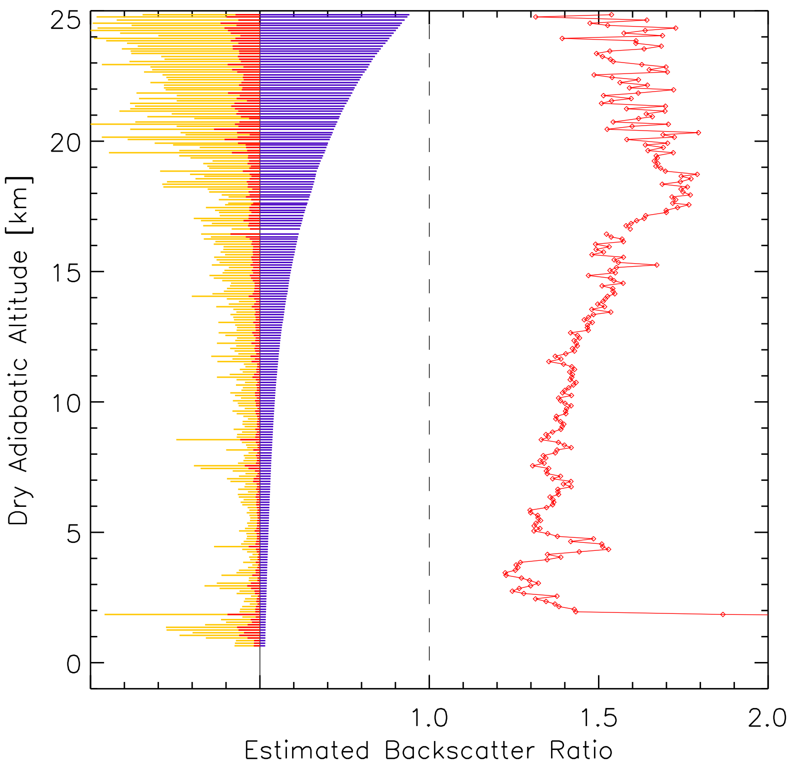

Figure 7.2: *Left panel shows in blue the noise expected for 1s data from lab measurements. This is compared to the standard deviation of the bin (yellow) and to its standard error (red). In the right panel the red BSR Signal of a sounding is shown. Figure credits by Dr. Frank Wienhold.*

7.2.4 Uncertainty calculations/bars

Currently, uncertainty estimates have not been applied to BSR data collected by COBALD. This needs to be done in future studies. Following is a way how this could be applied.

Firstly, it needs to be distinguished between precision and accuracy which describe uncertainty. These two terms are explained below referring to COBALD and followed by an example.

Precision of COBALD

The precision describes the degree to which several measurements are arranged to each other. It is an indicator of random error in the data and states that the smaller scatter, the higher the precision. The precision of COBALD is largely determined by electronical noise. The noise is assumed to be roughly 20 counts referring to the silicon photodiode counting photons.

Figure 7.2 shows the vertical profile for BSR_{red}. The raw data is binned into altitude intervals of 100 m representing approximately 20 values with an ascent rate of 5m/s. In the left panel the harp-shaped plot shows in blue the noise expected for the 1s data from lab measurements which means the 20 counts due to noise divided by the Rayleigh signal. This is compared the standard deviation of the bin (yellow) and to its standard error (red). Considering that the flight data contain the atmospheric variation this gives a conservative noise estimate of around 10% with respect to the Rayleigh level at 15 km altitude. In an altitude of 25 km the estimated noise is 50%. Consequently, COBALDs precision is altitude dependend.

Applying this to the measurements, 20 counts should be divided by the measured raw signal (counts) to estimate the precision.

Accuracy of COBALD

Accuracy describes how near measurements are to the true value. The accuracy in our case was determined with arctic COBALD measurements. Referring to section 3.2.3 the BSR_{blue} is initially set to a value of 1.05. Thereafter, the red BSR is set in ways to gain an upper and lower limit where we reveal a mode radius of approximately 0.1 μm and a particle density of 20 cm^{-3} as illustrated. The outcome is that the red BSR can be shifted 5% and the blue 3% referring to the measured signal.

An example for a COBALD relative error calculation

Assuming a raw signal in the infrared channel of 10'146 counts and a BSR_{red} of 17 in an altitude of 17 km precision and accuracy are calculated as followed. To obtain COBALDs relative precision, the electronical noise is divided by the measured raw signal: 20 counts/10'146 counts $\approx$ 0.2%. 0.2% of the BSR_{red} is 0.034. The relative accuracy is obtained by calculating 5 % of the BSR_{red} which is 0.85.

To obtain the relative error σ_{rel} following equation is applied:

$$\sigma_{rel} = \sqrt{p^2 + a^2}. \tag{7.1}$$

The result of the above example reveals a relative error of 0.85%.

List of Symbols and Abbreviations

ABSR	Aerosol Backscatter Ratio
BSR	Backscatter Ratio
CCN	Cloud condensation nuclei
CFH	Cryogenic Frostpoint Hygrometer
CI	Colour Index
COBALD	Compact Optical Backscatter AerosoL Detector
COSMO	COnsortium for Small-scale MOdelling
DWD	Deutscher Wetterdienst
e	Vapor pressure
ECMWF	European Centre for Medium Range Weather Forecasts
ETH	Eidgenössische Technische Hochschule; Swiss Federal Institute of Technology
FPH	FrostPoint Hygrometer
IAC	Institute for Atmospheric and Climate Science
IFS	Integrated Forecast System
IN	ice nuclei
ISSR	Ice Supersaturated Regions
LAGRANTO	Lagrangian Analysis Tool
LT	Local time
n	Refraction index
NWP	Numerical Weather Prediction
r	radius
RH	Relative humidity
RHi	Relative humidity with respect to ice
S_{ice}	Saturation with respect to ice
t	time
T	Temperature
TF	Frostpoint Temperature
UNFCCC	United Nations Framework Convention on Climat Change
v	terminal sedimentation velocity
λ	Wavelength
σ	Standard deviation
σ_{cs}	cross section

List of Figures

List of Tables

Bibliography

Abbatt, J., S. Benz, D. Cziczo, Z. Kanji, U. Lohmann, and O. Möhler, 2006: Solid ammonium sulfate aerosols as ice nuclei: A pathway for cirrus cloud formation. *Science*, **313**, 1770–1773.

ABC, 2009: Abc news, website available under http://www.abc.net.au, last accessed on 26 September 2009.

Albertz, J., 2001: *Einfuehrung in die Fernerkundung*. Wissenschaftliche Buchgesellschaft, 249 pp.

Australian Government, B. o. M., 2009: Weather maps, website available under http://www.bom.gov.au, last accessed on 30 September 2009.

Barahona, D. and A. Nenes, 2011: Dynamical states of low temperature cirrus. *Atmos. Chem. Phys*, **11**, 3757–3771.

Beyerle, G., M. Gross, D. Haner, N. Kjome, I. McDermid, T. McGee, J. Rosen, H.-J. Schäfer, and O. Schrems, 2001: A lidar and backscatter sonde measurement campaign at table mountain during february-march 1997: Observations of cirrus clouds. *Amer. Meteor. Soc.*, **15**.

Bohren, C. and D. Huffman, 2004: *Absorption and Scattering of Light by Small Particles*. Wiley-VCH Verlag GmbH and Co.

Borrmann, S., S. Solomon, J. Dye, and B. Luo, 1996: The potential of cirrus clouds for heterogeneous chlorine activation. *Geophys. Res. Lett.*, **23**, 2133–2136.

Brabec, M., F. Wienhold, and T. Peter, 2011: Particle backscatter and relative humidity in and around cirrus clouds measured with a lightweight balloon sonde, swiss National Science Foundation: Final Report.

Braham, R. and P. Spyers-Duran, 1967: Survival of cirrus crystals in clear air. *J. Appl. Meteo.*, **6**, 1053–1061.

CALIPSO, 2010: Calipso images available under http://www-calipso.larc.nasa.gov, last accessed on 10 May 2010.

Cantrell, W. and A. Heymsfield, 2005: Production of ice in tropospheric clouds, a review. *Amer. Meteor. Soc.*, 795–807.

Cassar, N., M. Bender, B. Barnett, S. Fan, W. Moxim, H. Levy, and B. Tilbrook, 2007: The southern ocean biological response to aeolian iron deposition. *Science*, **317**, 1067–1070.

Charlson, R., W. Porch, A. Waggoner, and N. Ahlquist, 1974: Background aerosols light scattering characteristics: nephelometric observations at mauna loa observatory compared with results at other remote locations. *Tellus 26*, **3**, 345–360.

Chen, T., W. Rossow, and Y. Zhang, 2000: Radiative effects of cloud-type variations. *J. Climate*, **13**, 264–286.

Christensen, J., B. Hewitson, A. Busuioc, A. Chen, X. Gao, I. Held, R. Jones, R. Kolli, W.-T. Kwon, R. Laprise, V. Magana Rueda, L. Mearns, C. Menendez, J. Raisanen, A. Rinke, A. Sarr, and P. Whetton, 2007: *Climate Change 2007: The Physical Science Basis. Contribution of Working Group I to the Fourth Assessment Report of the Intergovernmental Panel on Climate Change*, chap. Regional Climate Projections. Cambridge University Press,Cambridge, United Kingdom and New York, NY, USA.

COSMO, 2010: Consortium for small-scale modelling, website available under http://www.cosmo-model.org, last accessed on 26 December 2010.

Cziczo, D., D. Murphy, P. Hudson, and D. Thomson, 2004: Single particle measurements of the chemical composition of cirrus ice residue during crystal-face. *J. Geophys. Res.*, **109 (D04201)**, doi:10.1029/2003JD004032.

DeMott, P., 2002: *Laboratory Studies of Cirrus Cloud Processes*. Oxford University Press, pp. 102-135 pp., in Lynch,D.K., Sassen,K., Starr,D.O. and Stephens,G. (Eds.): Cirrus.

Dessler, A., K. Minschwaner, E. Weinstock, E. Hintsa, J. Anderson, and J. Russel, 1996: The effects of tropical cirrus clouds on the abundance of lower stratospheric ozone. *J. Atmos. Chem.*, **23**, 209–220.

Essenwanger, O., 1976: *Applied Statistics in Atmospheric Science*. Elsevier Scientific Publishing Company.

Finlayson-Pitts, B. and J. Pitts, 2000a: *Chemistry of the Upper and and Lower Atmosphere*. Academic Press, 969 pp.

———, 2000b: *Chemistry of the Upper and Lower Atmosphere. Theory, Experiments and Applications*. Academic Press: San Diego, 969 pp.

Fu, Q., P. Yang, and W. Sun, 1998: An accurate parameterization of the infrared radiative properties of cirrus clouds for climate models. *Amer. Meteor. Soc.*, **11**, 2223–2237.

Fujiwara, M., M. Shiotani, F. Hasebe, H. Vömel, S. Oltmans, P. Ruppert, T. Horinouchi, and T. Tsuda, 2003: Performance of the meteolabor ”snow white” chilled-mirror hygrometer in the tropical troposphere: Comparisons with the vaisala rs80 a/h-humicap sensors. *J. Atmos. Oceanic Technol.*, **15**.

Fusina, F., P. Spichtinger, and U. Lohmann, 2007: The impact of ice supersaturated regions and thin cirrus on radiation in the mid latitudes. *J. Geophys. Res.*, **112**.

Gao, R., P. Popp, D. Fahey, T. Marcy, R. Herman, E. Weinstock, D. Baumgardner, T. Garrett, K. Rosenlof, T. Thompson, P. Bui, B. Ridley, S. Wofsy, O. Toon, M. Tolbert, T. Kärcher, B. Peter, P. Hudson, A. Weinheimer, and A. Heymsfield, 2004: Evidence that nitric acid increases relative humidity in low-temperature cirrus clouds. *Science*, **303**, 516–520.

Giannakaki, E., D. Balis, V. Amiridis, and C. Zerefos, 2009: Optical properties of different aerosol types: seven years of combined ramanelastic backscatter lidar measurements in thessaloniki, greece. *Atmos. Meas. Tech.*

Gierens, K., U. Schumann, M. Helten, H. Smit, and A. Marenco, 1999: A distribution law for relative humidity in the upper troposphere and lower stratosphere derived from three years of mozaic measurements. *Annales Geophysicae*, **17**, 1218–1226.

Gildor, H. and M. Follows, 2002: Two-way interactions between ocean biota and climate mediated by biochemical cycles. *Israel Journal of Chemistry*, **42**, 15–27.

Griffin, D., V. Garrison, J. Herman, and E. Shinn, 2001: African desert dust in the caribbean atmosphere: Microbiology and public health. *Aerobiologia*, **17**, 203–213.

Heymsfield, A., L. Miloshevich, C. Schmitt, A. Bansemer, C. Twohy, M. Poellot, A. Fridlind, and H. Gerber, 2005: Homogeneous ice nucleation in subtropical and tropical convection and its influence on cirrus anvil microphysics. *Amer. Meteor. Soc.*, **62**.

Hienola, J., M. Kulmala, and A. Laaksonen, 2001: Condensation and evaporation of water vapor in mixed aerosols of liquid droplets and ice: numerical comparison of growth rate expressions. *J. of Aerosol Science*, **32**, 351–374.

Hobbs, P., 1993: *Aerosol-Cloud-Climate Interactions*. Academic Press, Inc., 237 pp.

Hoyle, C., B. Luo, and T. Peter, 2005: The origin of high ice crystal number densities in cirrus clouds. *J. Atmos. Sci.*, **62**, 2586–2579.

Husar, R., D. Tratt, B. Schichtel, S. Falke, F. Li, D. Jaffe, S. Gasso, T. Gill, S. Laulainen, F. Lu, M. Reheis, Z. Chun, D. Westphal, B. Holben, R. Frouin, J. Merrill, D. DuBois, F. Vignola, T. Murazama, S. Nickovic, W. Wilson, K. Sassen, N. Sugimoto, and W. Malm, 2001: Asian dust events of april 1998. *J. Geophys. Res.*, **106**, 18 317–18 330.

IPCC, 2007: Intergovernmental Panel on Climate Change: The Physical Science Basis, Cambridge Univ. Press, New York, 2007.

Jacob, D., 1999: *Introduction to atmospheric chemistry*. Princeton University Press, 266 pp.

Jaenicke, R., 1993: *Tropospheric Aerosols*. Academic Press, Inc., pp. 1-42 pp., in Hobbs,P. (Eds.): Aerosol-Cloud-Climate Interactions.

Jensen, E., P. Lawson, B. Baker, B. Pilson, Q. Mo, A. Heymsfield, A. Bansemer, T. Bui, M. McGill, D. Hlavka, G. Heymsfield, S. Platnick, G. Arnold, and S. Tanelli, 2009: On the importance of small ice crystals in tropical anvil cirrus. *Atmos. Chem. Phys.*, **9**, 5321–5370.

Jensen, E., J. Smith, L. Pfister, J. Pittman, E. Weinstock, D. Sayres, R. Herman, R. Troy, K. Rosenlof, T. Thompson, A. Fridlind, P. Hudson, D. Cziczo, A. Heymsfield, C. Schmitt, and J. Wilson, 2005: Ice supersaturations exceeding 100for cirrus formation and dehydration. *Atmos. Chem. Phys.*, **5**, 851–862.

Jensen, O., E.J. Toon, L. Pfister, and H. Selkirk, 1996: Dehydration of the upper troposphere and lower stratosphere by subvisible cirrus clouds near the tropical tropopause. *Geophys. Res. Letters*, **23**, 825–828.

Joos, H., P. Spichtinger, U. Lohmann, J.-F. Gayet, and A. Minikin, 2008: Orographic cirrus in the global climate model ECHAM5. *J. Geophys. Res.*, **113 (D18205)**, doi: 10.1029/2007JD009605.

Khvorostyanov, V. and K. Sassen, 1998: Cirrus cloud simulation using explicit microphysics and radiation. part ii: Microphysics, vapor and ice mass budget, and optical and radiative properties. *J. of the Atmospheric Science*, **55**, 1822–1845.

Koop, T., B. Luo, A. Tsias, and T. Peter, 2000: Water activity as the determinant for homogeneous ice nucleation in aqueous solutions. *Nature*, **406**, 611–614.

Korolev, A. and I. Mazin, 2003: Supersaturation of water vapor in clouds. *Amer. Meteor. Soc.*, **60**, 2957–2974.

Kärcher, B., 2002: Properties of subvisible cirrus clouds formed by homogeneous freezing. *Atmos. Chem. Phys.*, **2**, 161–170.

Kärcher, B. and U. Lohmann, 2003: A parameterization of cirrus cloud formation: Heterogeneous freezing. *J. Geophys. Res.*, **108**.

Krämer, M., M. de Reus, V. Ebert, V. Mitev, O. Möhler, H. Saathoff, R. Bauer, N. Spelten, C. Schiller, and N. Sitnikov, 2007: Supersaturations in cirrus: field and laboratory measurements. *International Workshop on Upper Tropospheric Humidity.*

Krämer, M., C. Schiller, A. Afchine, I. Bauer, R. Gensch, A. Mangold, S. Schlicht, N. Spelten, N. Sitnikov, S. Borrmann, M. de Reus, and P. Spichtinger, 2009: Ice supersaturations and cirrus cloud crystal numbers. *Atmos. Chem. Phys.*, **9**, 3505–3522.

Larson, N., B. Knudsen, T. Jorgensen, A. di Sarra, D. Fua, P. Di Girolamo, G. Fiocco, M. Cacciani, J. Rosen, and N. Kjome, 1994: Backscatter measurements of stratospheric aerosols at thule during january-february 1992. *Geophys. Res. Letters*, **21**, 1303–1306.

Larson, N., J. Rosen, N. Kjome, and B. Knudsen, 1995: Deliquescence and freezing of stratospheric aerosol observed by balloonborne backscattersonde. *Geophys. Res. Letters*, **10**, 1233–1236.

Laurent, B., I. Tegen, B. Heinhold, B. Schepanski, B. Weinzierl, and M. Esselborn, 2010: A model study of saharan dust emissions and distributions during the samum-1 campaign. *J. Geophys. Res.*, **115 (D21210)**, doi:10.1029/2009JD012995.

Lays, J., S. Heidenreich, and M. Case, 2009: Dustwatch report for week ending 28 september 2009, last accessed 5 June 2011: http://www.environment.nsw.gov.au.

Libbrecht, K., 2005: The physics of snow crystals. *Reports on progress in physics*, **68**, 855–895, doi:10.1088/0034-4885/68/4/R03.

Luo, B., C. Voigt, S. Fueglistaler, and T. Peter, 2003: Extreme nat supersaturations in mountain wave ice pscs: A clue to nat formation. *J. Geophys. Res.*, **108**, doi:10.1029/2002JD003104.

McCartney, E., 1976: *Optics of the Atmosphere: Scattering by Molecules and Particles.* John Wiley and Sons, 408 pp.

Möhler, O., D. Fahey, and R. Gao, 2009: Summary of the aquavit water vapor intercomparison: Static experiments, website available under https://aquavit.icg.kfa-juelich.de/whitepaper, last accessed on 16 March 2011.

Möhler, O., C. Linke, H. Saathoff, M. Schnaiter, R. Wagner, A. Mangold, M. Krämer, and U. Schurath, 2005: Ice nucleation on flame soot aerosol of different organic carbon content. *Meteorol. Z.*, **14**, 477–484.

Miloshevich, L., H. Vömel, D. Whiteman, B. Lesht, F. Schmidlin, and F. Russo, 2006: Absolute accuracy of water vapor measurements from six operational radiosonde types launched during awex-g and implications for airs validation. *J. Geophys. R.*, **111**, D09S10.

Mishchenko, M., L. Travis, and D. Mackowski, 1996: T-matrix computations of light scattering by nonspherical particles: a review. *J. Quant. Spectrosc. Radiat. Transfer*, **55**, 535–575.

Monahan, J., 2001: *Numerical Methods of Statistics*. Cambridge University Press, 425 pp.

Moulin, C., F. Guillard, F. Dulac, and C. Lambert, 1997: Long-term daily monitoring of saharan dust load over ocean using meteosat isccp-b2 data 1. methodology and preliminary results for 1983-1994 in the mediterranean. *J. Geophys. Res.*, **102**, 16 947–16 958.

Murphy, D. and T. Koop, 2005: Review of the vapor pressures of ice and supercooled water for atmospheric applications. *R. Meteorol. Soc.*, **131**, 1539–1565.

Murray, B., 2008: Inhibition of ice crystallisation in highly viscous aqueous organic acid droplets. *Atmos. Chem. Phys.*, **8**, 5423–5433.

Murray, B., D. Knopf, and A. Bertram, 2005: The formation of cubic ice under conditions relevant to earth's atmosphere. *Nature*, **434**, 202–205.

Ovarlez, J., Gayet.J., K. Gierens, J. Ström, H. Ovarlez, F. Auriol, R. Busen, and U. Schumann, 2002: Water vapour measurements inside cirrus clouds in northern and southern hemispheres during inca. *Geophysical Research Letters*, **29**.

Overlaz, J. and P. van Velthoven, 1997: Comparison of water vapor measurements with data retrieved from ecmwf analyses during the polinat experiment. *J. Appl. Meteorol.*, **36**, 1329–1335.

Overlaz, J., P. van Velthoven, G. Sachse, S. Vay, H. Schlager, and H. Ovarlez, 2000: Comparison of water vapor measurements from polinat 2 with ecmwf analyses in high humidity conditions. *J. Geophys. Res.*, **105**, 3737–3744.

Pechey, L., M. Andrew, and G. Gentle, 2007: Review of the lake eyre basin intergovernmental agreement. *Report*.

Peter, T., C. Marcolli, P. Spichtinger, T. Corti, M. Baker, and T. Koop, 2006: When dry air is too humid. *Science*, **314**, 1399–1402.

Peter, T. and F. Wienhold, 2006: Particle backscatter and relative humidity in and around cirrus clouds measured with a lightweight sonde suitable for operational monitoring, proposal.

Pruppacher, H. and J. Klett, 1997: *Microphysics of clouds and precipitation*. Kluwer Academic Publisher, 954 pp.

Qin, Y. and R. Mitchell, 2008: Characterisation of episodic aerosol types over the australian continent. *Atmos. Chem. Phys.*, **8**, 18 803–18 842.

Radhi, M., M. Box, R. Mitchell, D. Cohen, E. Stelcer, and M. Keywood, 2010: Size-resolved mass and chemical properties of dust aerosols from australia's lake eyre basin. *Atmospheric Environment*, **44**, 3519–3528.

Rosen, J. and N. Kjome, 1991: Backscattersonde: a new instrument for atmospheric aerosol research. *Appl. Opt.s*, **30**, 1552–1561.

Rosen, J., N. Kjome, and B. Liley, 1997: Tropospheric aerosol backscatter at a midlatitude site in the northern and southern hemispheres. *J. Geophys. Res.*, 21 329–21 339.

Rotstayn, L., M. Keywood, B. Forgan, A. Gabric, I. Galbally, J. Gras, A. Luhar, G. McTainsh, R. Mitchell, and S. Young, 2009: Possible impacts of anthropogenic and natural aerosols on australian climate: a review. *Intern. J. Climat.*, **21**, 461–479.

Royston, J., 1982: Algorithm as 181: The w test for normality. *Appl. Statist.*, **31**, 176–180.

Sassen, K., 2002: *Cirrus Clouds*. Oxford University Press, pp. 11-40 pp., in Lynch,D.K., Sassen,K., Starr,D.O. and Stephens,G. (Eds.): Cirrus.

Satheesh, S. and K. Moorthy, 2004: Radiative effects of natural aerosols: A review. *Atmospheric Environment*, **39**, 2089–2110.

Schumann, U., 2002: *Cotrail Cirrus*. Oxford University Press, pp. 231-255 pp., in Lynch,D.K., Sassen,K., Starr,D.O. and Stephens,G. (Eds.): Cirrus.

Seinfeld, J. and S. Pandis, 1998: *Atmospheric Chemistry and Physics: From Air Pollution to Climate Change*. Wiley-Interscience,New York, 1326 pp.

Shilling, J., M. Tolbert, O. Toon, E. Jensen, B. Murray, and A. Bertram, 2006: Measurements of the vapor pressure of cubic ice and their implications for atmospheric ice clouds. *Geophys. Res. Lett.*, **33**, L17 801.

Spichtinger, P., 2004: *Eisübersättigte Regionen*. Deutsches Zentrum für Luft- und Raumfahrt, 208 pp.

Spichtinger, P., K. Gierens, and A. Dörnbrack, 2005a: Formation of ice supersaturation by mesoscale gravity waves. *Atmos. Chem. Phys.*, **5**, 1243–1255.

Spichtinger, P., K. Gierens, U. Leiterer, and H. Dier, 2003: Ice supersaturation in the tropopause region over Lindenberg, Germany. *Meteorol. Z.*, **12**, 143–156.

Spichtinger, P., K. Gierens, and W. Read, 2002: The statistical distribution law of relative humidity in the global tropopause region. *Meteorol. Z.*, **11**, 83–88.

Spichtinger, P., K. Gierens, and H. Wernli, 2005b: A case study on the formation and evolution of ice supersaturation in the vicinity of a warm conveyor belt's outflow region. *Atmos. Chem. Phys.*, **5**, 1243–1255.

Steppeler, J., G. Doms, U. Schättler, H. Bitzer, A. Gassmann, U. Damrath, and G. Gregoric, 2003: Meso-gamma scale forecasts using the nonhydrostatic model lm. *Meteorol. Atmos. Phys.*, **82**, 75–96.

Stohl, A., C. Forster, A. Frank, P. Seibert, and G. Wotawa, 2005: Technical note: The lagrangian particle dispersion model flexpart version 6.2. *Atmos. Chem. Phys*, **5**, 2461–2474.

Strawbridge, K. and B. Snyder, 2004: Planetary boundary layer height determination during pacific 2001 using the advantage of a scanning lidar instrument. *Atmospheric Environment*, **38**, 5861–5871.

Tanaka, T. and M. Chiba, 2006: A numerical study of the contributions of dust source regions to the global dust budget. *Global and Planetary Change*, **52**, 88–104.

Tegen, I. and A. Lacis, 1996: Modeling of particle size distribution and its influence on the radiative properties of mineral dust aerosol. *J. Geophys. Res.*, **101**, 19 237–19 244.

Tompkins, A., K. Gierens, and G. Rädel, 2007: Ice supersaturation in the ecmwf integrated forecast system. *Q. J. R. Meteorol. Soc.*, **133**, 53–63.

Tratt, D., R. Frouin, and L. Douglas, 2001: April 1998 asian dust event¿ a southern california perspective. *J. Geophys. Res.*, **106**, 18 371–18 379.

Vaughan, M., S. Young, D. Winker, K. Powell, A. Omar, Z. Liu, Y. Hu, and C. Hostetler, 2004: Fully automated analyses of space-based lidar data: an overview of the calipso retrieval algorithms and data products. *Laser Radar Techniques for Atmospheric Sensing*, **5575**, 16–30.

Vömel, H., D. David, and K. Smith, 2007a: Accuracy of tropospheric and stratospheric water vapor measurements by cryogenic frost point hygrometer: Instrumental details and observations. *J. Geophys. Res.*, **112**, D08 305.

Vömel, H., M. Fujiwara, M. Shiotani, F. Hasebe, S. Oltmans, and J. Barnes, 2003: The behavior of the snow white chilled-mirror hygrometer in extremely dry conditions. *J. Atmos. Oceanic Technol.*, **20**, 1560–1567.

Vömel, H., S. Oltmans, D. Hofmann, T. Deshler, and J. Rosen, 1995: The evolution of the dehydration in the antarctic stratosphere vortex. *J. Geophys. Res.*, **100**, 13 919–13 926.

Vömel, H., V. Yushkov, S. Khaykin, L. Korshunov, E. Kyrö, and R. Kivi, 2007b: Intercomparisons of stratospheric water vapor sensors: Flash-b and noaa/cmdl frost-point hygrometer. *J. Atmos. Oceanic Technol.*, **24**, 941–952.

Weisenstein, D., G. Yue, M. Ko, N.-D. Sze, J. Rodriguez, and C. Scott, 1997: A two-dimensional model of sulfur species and aerosols. *J. Geophys. Res.*, **102**, 13 019–13 035.

Wendisch, M., P. Yang, and P. Pilewskie, 2007: Effects of ice crystal habit on thermal infrared radiative properties and forcing of cirrus. *J. Geophys. Res.*, **112 (D08201)**, doi:10.1029/2006JD007899.

Wernli, H. and H. Davies, 1997: A lagrangian-based analysis of extratropical cyclones. i: The method and some applications. *Q.J.R. Meteorol. Soc.*, **123**, 467–489.

Wiacek, A. and T. Peter, 2009: On the availability of uncoated mineral dust ice nuclei in cold cloud regions. *Geophys. Res. Lett.*, **36**, L17 801.

Wiederhold, P., 1997: *Water vapor measurement: methods and instrumentation.* Marcel Dekker, Inc., 353 pp.

Wienhold, F., 2008: Cobald data sheet: datasheet available under http://www.iac.ethz.ch/groups/peter/research/, last accessed on 17 May 2011.

WMO, 1956: *International cloud atlas.* Geneva.

Wylie, D., 2002: *Cirrus and Weather: A Satellite Perspective.* Oxford University Press, pp. 136-146 pp., in Lynch,D.K., Sassen,K., Starr,D.O. and Stephens,G. (Eds.): Cirrus.

Wylie, D. and W. Menzel, 1999: Eight years of high cloud statistics using HIRS. *J. Clim.*, **12**, 170–184.

Zhang, M., W. Lin, S. Klein, J. Bacmeister, S. Bony, R. Cederwall, A. DelGenio, J. Hack, N. Loeb, U. Lohmann, P. Minnis, I. Musat, R. Pincus, P. Stier, M. Suarez, M. Webb, J. Wu, S. Xie, M. Yao, and J. Zhang, 2005: Comparing clouds and their seasonal variations in 10 atmospheric general circulation models with satellite measurements. *J. Geophys. Res.*, **110 (D15S02)**, doi:10.1029/2004JD005021.

Ziemann, P., 2010: Atmospheric chemistry: Phase matters for aerosols. *Nature*, **467**, 797–798.

Zobrist, B., C. Marcolli, D. Pedernera, and T. Koop, 2008: Do atmospheric aerosols form glasses? *Atmos. Chem. Phys.*, **8**, 5221–5244.

Acknowledgment

Over the past three years, many colleagues, friends and family members supported me in different ways and encouraged me to successfully complete this thesis. I'm very gratful to all those who believed in me.

My first cordial "thank you" goes to Prof. Thomas Peter, for offering me the opportunity to work on this thesis and for not only being a excellent scientifical support, but also a motivator and a role model of someone who works with passion. I greatly appreciated your incredible open-mindedness and flexibility when I came up with the idea to work in another country twice.

Many thanks to Frank Wienhold, my supervisor, who helped me with a great deal of scientific and technical advice. Thanks for being open-minded to have skype meetings when I was abroad. Thanks for reading my thesis very carefully and for all the corrections.

Thanks to Beiping Luo, for sharing his knowledge, his magical model run outputs and patiently answering stupid questions.

Special thanks to:

My former and present office mates Hanna, Hanna, Felix, Zamin and Amewu. Thanks Hanna Joos, for the great support and solving some of my trajectory problems.

Michelle, for being a sincere friend and for shaking me awake once in a while.

Uwe, who made me laugh heaps, who I shared quite a few beers, who was listening to all my problems and giving me advices.

Luc and Fabian, for keeping me fit during a life in front of the computer.

FLINK, for keeping me creative and alive.

Sergey Khaykin, for being a very good companion on campaigns and workshops.

Alexey Lykov, for repairing my instruments in Niamey and therefore saving my campaign.

Marc Wüest, for introducing me into the topic.

Peter Isler and Dani Lüthi for technical support and being patient.

Petra Forney and Eva Choffat, for excellent administrative work and advice.

Holger Vömel, for his calm and friendly manner and agreeing to be my co-examiner.

Prof. Dr. Harald Bugmann, for being my co-examiner.

Shubha, for sharing the suffering and gossiping once in a while.

Harald, for giving me statistical advice at the last minute.

Beni, for all feedback and the chats in the hallway.

Greg Bodeker, who was the intermediary in Lauder, New Zealand and made it possible for me to go there. Many thanks go also to the whole Lauder-team for their hospitality during my stay.

Edwin Hausammann who fabricated some of the COBALD's I was working with and being the calm pole of the institute.

My family for all the support and the healthy food from the garden. Last but not least Nat, who proofread my thesis, for being patient during stressful times, for the nice time in NZ and everything which waits for us in the future.

Curriculum Vitae

Martin Brabec
born 16 March 1978 in Luzern, Switzerland
citizen of Kriens (LU), Switzerland

Education

2007 - 2011	Ph.D. at ETH, Institute of Atmospheric and Climate Science
2002 - 2007	Master Of Science
1995	Exchange year in Australia, Brisbane
1993 - 1999	Teacher College in Lucerne

Professional Experience

0?/2003–0?/2005	German lessons at vocational school (Berufsschule Luzern).
09/1999–07/2003	Teaching in several primary and secondary schools in Luzern and Zürich. Focus on mathematics, geography and music.

Conferences and Workshops

LAPBIAT Workshop, Helsinki (2010)

International Conference on Clouds and Precipitation (ICCP), (reward to the best instrumental poster) Cancun, Mexico (2008)

COST Workshop (Action ES0604), Atmospheric Water Vapour in the Climate System (WaVaCS), Lindenberg, Germany (2008)
AquaVIT Workshop, The AquaVIT formal intercomparison of atmospheric water measurement methods, Karlsruhe, Germany (2008)

Campaigns

Lapland atmosphere-biosphere facility (LAPBIAT), Sodankylä, Finland (2009)

Lindenberg Upper-Air Methods Intercomparison (LUAMI), Lindenberg, Germany (2008)

SCOUT-O3, Niamey, Niger (2008)

AquaVIT formal intercomparison of atmospheric water measurement methods, Karlsruhe, Germany (2008)